THÈSE

En vue de l'obtention du

DOCTORAT DE L'UNIVERSITÉ DE TOULOUSE

Délivré par : ***l'Université Toulouse III-Paul Sabatier***
Discipline ou spécialité : ***Génie Civil***

Présentée et soutenue par ***Muazzam Ghous SOHAIL***
Le ***14/05/2013***

Corrosion of Steel in Concrete: Development of an Accelerated Test by Carbonation and Galvanic Coupling

---

JURY

Dr. HDR Valérie L'HOSTIS	***Rapporteur***	***CEA Saclay***
Prof. Karim AIT-MOKHTAR	***Rapporteur***	***Université de la Rochelle***
Prof. Abdelhafid KHELIDJ	***Examinateur***	***Université de Nantes***
Prof. Jean-Paul BALAYSSAC	***Examinateur***	***Université de Toulouse***
Dr. Stéphane LAURENS	***Examinateur***	***Université de Toulouse***
Dr. Fabrice DEBY	***Examinateur***	***Université de Toulouse***

Ecole doctorale : Mécanique, Energétique, Génie civil et Procédés (MEGeP)
Unité de recherche : Laboratoire Matériaux et Durabilité des Constructions (LMDC)
Directeur de Thèse**: *Jean-Paul BALAYSSAC***
Co-directeur**: *Stéphane LAURENS***
Co-directeur**: *Fabrice DEBY***

Acknowledgement

If I am writing an acknowledgement of my Ph.D. thesis, it is only by the grace of mother and my father, who have worked so hard to make me what I am today. I dedicate this thesis to my parents and all those parents who introduce their children to the wisdom of knowledge. Then I thank to my sisters Farah and Uzma and my brother Ali for their love and care, you all are my proud.

I am very thankful to my supervisors, Prof. Dr. Jean-Paul Balayssac, Dr. Stéphane Laurens and Dr. Fabrice Deby for their utmost support during these three years of my Ph.D. work. During all those lengthy scientific discussions, I have learnt a lot, not just about my subject but also about the attitude towards research. I feel honored to be working with a team full of knowledge and passion to advance in research.

I am also thankful to director of Laboratoire Matériaux et Durabilité des Constructions (LMDC) Mr. Gilles Escadeillas for receiving me in the institute and providing me all the facilities and equipment required to carry out this research work. I would like to thank all the technical staff of LMDC who has helped during my work, specially Mr. Attard, Sylvain and Carole. I pray for the prosperity of this prestigious laboratory.

I am thankful to Higher Education Commission of Pakistan (HEC) for awarding me a scholarship and providing me this opportunity to study in France. I would also like to thank SFERE for taking care of all the administrative matters during my stay in France.

I am also thankful to all my friends in Toulouse, specially Dr. Rashid, Dr. Rizwan, Dr. Majid, Dr. Toufeer, Dr. Ilyas and Dr. Shahid. Then I would like to thank, Abid, Ayesha, Inam and Tameez, their presence made my stay more pleasant. I am thankful to all my collegues of office, Angel, Minh, Rackel, Hugo, Marie, Rémy and Raphaëlle, and a very special thanks to Antoine, who helped me a lot during my Ph.D.

Above all I thank to God, the most Merciful and Generous, who gave me the strength and knowledge to achieve this milestone of my life.

Abstract

This work presents the results of an experimental and numerical study of an accelerated corrosion test, performed in laboratory. The acceleration of corrosion in reinforced concrete is due to the elimination of initiation phase by an artificial environment technique. The initiation phase takes years to undergo, if it is accelerated, the studies can be focused on the kinetics of steel corrosion in concrete. For acceleration of initiation phase the concrete samples were kept in a carbonation chamber set at 50% CO_2 and 65% RH. The geometry used in this test is comprised of two concrete cylinders. The inner concrete cylinder is carbonated and has a steel bar in the center, the bar is depassivated and acts as anode (A). The outer cylinder comprised of non-carbonated concrete, casted around the inner carbonated cylinder. Four steel bars are embedded around centered bar at given distance in non-carbonated concrete; these bars are in passive state and act as cathodes (C). The presence of these passive bars will allow changing the cathode surface and hence C/A ratio, by connecting different number of bars to active bar.

The geometry for the test is defined by numerical simulations using COMSOL Multiphysics® software, and its sensitivity in particular the effect of C/A ratio, is defined by numerical experiments. In order to provide reliable inputs for the model the corrosion parameters are measured. Once the geometry of the samples is defined an extensive experimental program involving 15 samples is carried out. Despite the higher resistivity of carbonated concrete layer, the measurements of macrocell current revealed high levels of galvanic corrosion rate even in case of low C/A ratio. With the increase in C/A ratio the higher macrocell current levels are achieved in propagation phase. The importance of galvanic coupling in carbonation-induced corrosion is therefore also experimentally demonstrated.

The accordance between numerical and experimental results is demonstrated regarding both potential field and C/A influence on macrocell current. This coherence highlights the relevance of the numerical modeling.

Key words: Concrete corrosion, carbonation, accelerated corrosion test, macrocell corrosion system, numerical modeling.

Résumé

L’objectif principal de ce travail est de développer un essai accéléré de corrosion dans le béton armé capable de bien représenter les conditions de développement de la corrosion en environnement réel. Le test reproduit les phases d’initiation et de propagation. La phase d’initiation correspond à la période durant laquelle les agents agressifs (le CO_2 ou les ions chlorure) pénètrent à travers le béton d’enrobage jusqu’à atteindre l’armature. La phase de propagation se produit une fois que le béton entourant les armatures est totalement pollué par les agents agressifs et les conditions nécessaires étant réunies, la corrosion de l’acier démarre. Dans cette étude la phase d’initiation est accélérée en exposant le béton dans une enceinte avec un taux de CO_2 de 50% et une humidité relative de 65%. Dans la phase de propagation la corrosion de type galvanique est accélérée en augmentant le rapport de surface entre cathode et anode.

Les échantillons utilisés sont composés de deux cylindres de béton imbriqués. Le cylindre interne contient une seule armature et le béton d’enrobage est entièrement carbonaté. Autour de cette éprouvette un cylindre externe de béton est alors coulé avec quatre armatures régulièrement réparties sur sa périphérie. Le béton du cylindre externe est préservé de la carbonatation. Les barres externes sont donc dans un état passif et la barre interne dans un état actif. La distance entre chaque barre du cylindre externe et la barre du cylindre interne est identique. La connexion entre une ou plusieurs barres passives et la barre active génère un courant galvanique qui va entraîner la corrosion de la barre active. En jouant sur le nombre de barres passives connectées on peut donc faire varier l’intensité du courant galvanique et donc accéléré ou ralentir la corrosion.

Pour éviter de réaliser un trop grand nombre d’essais en laboratoire, la conception de l’essai et la définition de sa sensibilité sont effectuées par le biais de simulations numériques à l’aide du logiciel commercial COMSOL Multiphysics® qui utilise les éléments finis. La vitesse de corrosion de l'acier dans le béton est déduite de la densité de courant à la surface de l'acier, qui est elle-même reliée au potentiel. La modélisation numérique de la corrosion dans le béton implique la résolution de deux équations simultanément, l'équation du transfert de charge et la loi d'Ohm, avec des conditions aux limites appropriées. Le comportement du système électrochimique est décrit par l'équation de Butler-Volmer pour les aciers actifs et passifs. Les paramètres nécessaires à l’implémentation des équations de Butler-Volmer (constantes de

Tafel, potentiel et courant de corrosion) sont mesurés par le biais d’une campagne expérimentale sur un nombre significatif d’échantillons carbonatés ou non carbonatés. Il est ainsi possible de disposer de données réellement représentatives des conditions de l’essai accéléré. L’essai est ensuite réalisé en conditions de laboratoire et les résultats sont analysés et comparés aux calculs du modèle numérique.

Le premier chapitre de la thèse est dédié à une revue bibliographique sur les phénomènes liés à la corrosion dans le béton armé. L'électrochimie qui exprime le phénomène de corrosion et la cinétique de Butler-Volmer de corrosion de l'acier (métal) sont présentées. Ensuite, les méthodes de caractérisation de la corrosion de l'acier dans le béton sont discutées. Les modèles numériques disponibles dans la littérature jusqu'à présent sont détaillés, en focalisant sur ceux qui prédisent la densité de courant de corrosion d'une barre d’acier en utilisant la cinétique de Butler-Volmer. A la fin, les tests accélérés utilisés par les différents chercheurs sont présentés et analysés.

Le deuxième chapitre est consacré à la mesure des paramètres nécessaires pour modéliser la corrosion dans le béton armé. Les paramètres tels que le potentiel de corrosion, la densité de courant de corrosion, les coefficients de Tafel anodique et cathodique sont obtenus à partir des courbes de polarisation. Pour obtenir ces courbes de polarisation des expériences de Tafel sont effectuées sur des échantillons cylindriques de béton carbonaté et non carbonaté. L’influence de la vitesse de balayage a été en particulier étudiée. Dans certaines conditions, les résultats obtenus montrent une variabilité relativement importante des paramètres de Tafel.

Dans le troisième chapitre, la conception du test de corrosion accélérée proposé est présentée. La géométrie numérique et expérimentale de l'échantillon utilisée pour ces tests est élaborée. Dans les expériences numériques, la variation de la surface polarisée sur l’acier actif en fonction du nombre d’aciers passifs connectés est particulièrement bien démontrée. A l'aide des simulations numériques, une étude paramétrique a été réalisée et l’incidence des différents paramètres de corrosion sur le courant galvanique est observée. L’influence de la résistivité du béton sur l’intensité du courant galvanique d’une part et sur la polarisation de barres d'acier actif et passif d’autre part est également soulignée.

Le quatrième chapitre présente les résultats expérimentaux obtenus durant la phase de différents essais mettant en œuvre 15 éprouvettes. L'accélération de corrosion à la propagation a été réalisée en augmentant le nombre de barres passives connectées suivant deux

configurations. Un dispositif expérimental original a permis de suivre l’évolution du courant galvanique au cours de la durée de l’essai. Les résultats confirment bien les prévisions du modèle, en particulier l’influence du nombre de barres passives connectées sur la polarisation de la barre active. Les courants galvaniques obtenus sont ensuite comparés aux résultats du modèle et les tendances sont également confirmées. Des autopsies pratiquées sur certaines éprouvettes ont permis de comparer la masse de produits de corrosion formés à la masse calculée à partir de la loi de Faraday en faisant intervenir le courant galvanique et le temps d’exposition.

TABLE OF CONTENTS

3 DESIGN OF ACCELERATION CORROSION TEST ……………………………………………………………70

LIST OF FIGURES

LIST OF TABLES

INTRODUCTION

Corrosion of reinforced concrete (RC) is a major cause of structural degradation. Maintenance and rehabilitation of RC structures has become as important and costly as new construction. The economic loss and damage caused by the corrosion of steel in concrete makes it the largest infrastructure problem faced by industrialized countries in recent times. The cost of repair to damage caused by corrosion could be around 3.5% GDP in developed countries. Corrosion in concrete is due to the ingress of chloride ions till the steel surface or carbonation of concrete cover. The pH of concrete pores solution is normally above 12, in such alkaline environment an oxide film is formed at steel surface, which protects steel from corroding. The carbonation reduces the pH of concrete below 9, which causes the breakdown of oxide passive layer, and steel becomes depassivated and corrosion process starts.

The concrete volume provides excellent protection for steel reinforcement thanks to the high alkalinity of concrete pore solutions. The quality of concrete cover also provides good physical protection to steel from aggressive environment, and it takes years for aggressive agents like CO_2 and chloride ions Cl^- to reach steel surface. This makes the study of corrosion behavior, in different environments of concrete, a time taking project even in the laboratory experiments. That is why accelerated tests are designed. They help to study the corrosion behavior and to predict the remaining structure life for engineering purposes. According to Tuutti’s corrosion model, corrosion process can be divided in two phases, initiation phase, where aggressive agents penetrate through the concrete cover and reach the steel surface, and propagation phase, where corrosion process of steel reinforcement starts and develops.

The main objective of this work was to develop an accelerated corrosion test (ACT), which could simulate the naturally occurring corrosion in concrete structures, in laboratory environment. The accelerated corrosion test presented in this work consists of two stages; the first is to accelerate the corrosion process in initiation phase, which was achieved by accelerated carbonation. While in propagation phase corrosion process was accelerated by increasing Cathode/Anode surface ratio. The increase in cathode surface was achieved by increasing the number of passive bars embedded in concrete.

In addition, to avoid time consuming laboratory experiments, the design of the accelerated corrosion test was at first carried out by means of numerical simulations. The simulations were performed by using commercially available software COMSOL Multiphysics® which is based on FEM. The corrosion rate of steel in concrete could be deduced from current density at steel surface, which is related with potential at the steel surface. Numerical modeling of corrosion in concrete involves the solution of two equations simultaneously; the equation of charge transfer and the second is Ohm’s law, for appropriate boundary conditions. The polarization behavior of electrochemical systems is described by the Butler–Volmer equation for both active and passive steel bars. Parameters involved in equations were calculated from polarization curves obtained from Tafel experiments on carbonated and non-carbonated concrete samples.

The first chapter presents the state of the art in the field of corrosion in reinforced concrete. The electrochemistry involved in corrosion phenomenon is explained. The Butler-Volmer kinetics of steel corrosion is presented afterwards. Then, the methods of assessing the corrosion state of steel and the methods of measurements of corrosion currents in concrete are discussed. The numerical models available in the literature up to now are elaborated; the models which predict the corrosion current density of a corroding bar by using Butler-Volmer kinetics are also discussed. At the end, the accelerated tests used by researcher till present are discussed and their techniques are described.

The second chapter is dedicated to the parameters required to model the corrosion phenomenon in reinforced concrete. The parameters like corrosion potential, corrosion current density, anodic Tafel slope coefficient and cathodic Tafel slope coefficients were calculated from polarization curves. These polarization curves were obtained from Tafel experiments performed on the cylindrical carbonated and non-carbonated concrete samples.

In third chapter, the design of proposed accelerated corrosion test (ACT) is presented. The numerical and experimental geometry of the sample used for these tests is elaborated. The basic theory of microcell and macrocell corrosion phenomenon is explained with the help of polarization curves of the active and passive systems. By numerical experiments, the face-to-face polarization effects and the effect of increase in Cathode/Anode ratio on polarization behviour of both active and passive bars were observed. With help of these numerical simulations a parametric study was performed on a galvanic corrosion system, hence the effects of change in all corrosion parameters were observed. The effects of concrete resistivity on macrocell current and on the polarization behviour of active and passive steel bars were also observed.

The chapter four presents the results of accelerated corrosion test. The acceleration in propagation was achieved by increasing the number of passive bars in a macrocell corrosion system. At first the effects of Cathode/Anode ratio on macrocell corrosion current found by numerical simulations are presented. Then the results of laboratory experiments which study the effect of Cathode/Anode ratio are discussed. A comparison between numerical and experimental results is done to validate the corrosion model. The conclusions and perspectives are discussed at the end.

CHAPTER # 1

1 State of the art

1.1 Electrochemistry involved in corrosion

1.1.1 Thermodynamics

The iron is found in the form of oxides in natural environment. When thermal or mechanical treatments are applied to convert iron into pure steel, it becomes thermodynamically unstable, and always tends to revert back to its original form which is at a lower level of energy, i.e. in the form of oxides. Hence, the steel always tends to corrode to form oxides in an environment where humidity and oxygen are present. To understand the corrosion mechanism in concrete it is important to discuss the thermodynamics and kinetics of an electrochemical reaction.

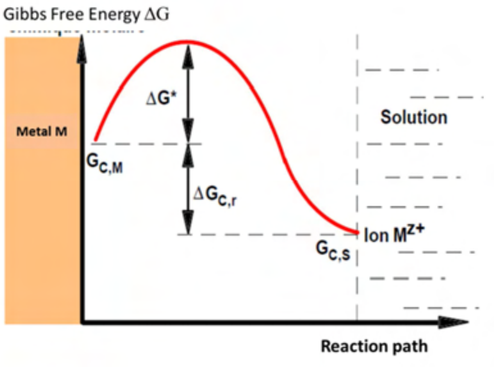

Figure 1-1 Activation Complex, showing transfer of ions into solution (Cefracor, n.d.)

Thermodynamic explains the occurrence of any chemical reaction. The tendency of a chemical reaction to go forward is determined by the change in Gibbs free energy ΔG of a system. When a metal M dipped into a solution which contains the ions of same metal, the metal ions M^+ start following into the solution. Each metallic atom can be considered as an ion occupying a certain energy level that can be represented by its chemical Gibbs free energy $G_{C,M}$ (Figure 1-1). It may exist for these ions a different energy level in the solvent represented by chemical Gibbs free energy $G_{C,S}$ as shown in the (Cefracor, n.d.; Revie and Uhlig, 2008).

Due to thermal agitation, metal ions tend to jump into solution by crossing the energy barrier that is the breakage of their electronic bonds. In Figure 1-1, the difference between highest energy level and G $_{C,M}$ represents the energy of activation $\Delta G^{\,*}$ (E_a), which is required for the transition of metal into the solution (Perez, 2004; Revie and Uhlig, 2008).

The Eq.1.1 and Eq.1.2 are examples of iron dissolution and conversion of ferric ions into ferrous ions. As more negative value of Gibbs free energy indicates more rapid forward reaction, so in Eq.1.2 the reaction will go forward, but in first reaction it would not proceed forward naturally.

$$Fe^{2+} + 2e^{-} \rightarrow Fe \qquad E° = -.440V,\ \Delta G° = +.880\,F \qquad \textit{Eq. 1.1}$$

$$Fe^{3+} + e^{-} \rightarrow Fe^{2+} \qquad E° = +.771V,\ \Delta G° = -.771\,F \qquad \textit{Eq. 1.2}$$

1.1.2 Nernst Equation

Based on thermodynamic principle, Nernst established an equation to calculate the cell potential or potential of an electrochemical reaction, which depends upon the activities of reactant and products (Perez, 2004; Revie and Uhlig, 2008). When a metal is dipped into a solution, metal ions starts moving into solution due to potential difference, however, the presence of positive ions near the metal-water interface and excess of electrons at the metal surface create a potential barrier and halts the further dissolution of metal ions. This creates a dynamic equilibrium (Perez, 2004) .

$$M \leftrightarrow M^{n+} + ne^{-} \qquad \textit{Eq. 1.3}$$

This equilibrium corresponds to a potential E, which represents potential between the metal M and the solution containing ions M^{n+}. E is called reversible electrode potential E_{rev}. When this equilibrium is formed, there is equality between the change in Gibbs free energy $\Delta G_{C,r}$ of the dissolution reaction and electrical energy W_E needs to cross the potential barrier Figure 1-1. For an electrochemical reaction electrical energy is written in absolute terms of Eq.1.4.

$$W_E = nFE \qquad \text{Eq. 1.4}$$

Where, F is the Faraday number (charge of one mole of electrons: 96,500 Coulomb/mole). The thermodynamic relation between standard Gibbs free $\Delta G°$ and Gibbs free energy ΔG at any instant is given by.

$$\Delta G = \Delta G° + RTLnK \qquad \text{Eq. 1.5}$$

Where: R gas constant, 8.314 J/ mol. k, T temperature, K is rate of reaction.

Since,

$$\Delta G° = -nFE° \qquad \text{Eq. 1.6}$$

$E°$ is standard electrode potential and n is number of electrons taking part in a reaction. The general equation can be written as,

$$\Delta G = - nFE$$

$$-nFE = -nFE° + RT \ln K$$

$$E = E° - \frac{RT}{nF} LnK \qquad \text{Eq. 1.7}$$

Eq. 1.7 is Nernst equation which gives the instantaneous potential of an electrochemical cell in terms of reaction rate K, which in turn related to the activities of products and reactants (Perez, 2004; Redaelli et al., 2006; Revie and Uhlig, 2008).

1.1.3 Pourbaix Diagram

M. Pourbaix (Pourbaix, 1974) devised a compact summary of thermodynamic data in the form of potential-pH diagram, which relates to the electrochemical and corrosion behaviour of the any metal in water. These diagrams have the advantage of showing at glance the specific conditions of potential and pH under which the metal either does not react or reacts to form specific oxides or complex ions, i.e. the Pourbaix diagrams indicate the potential and pH domains in which a metal is stable (Cefracor, n.d.; Redaelli et al., 2006; Revie and Uhlig, 2008).

Figure 1-2 is the Pourbaix diagram of iron, by convention, the Pourbaix diagram is established at $25°C$ and concentration of dissolved species is at $10^{-6}\ mol.\,l^{-1}$. Two iron oxides were considered for this particular diagram, hematite Fe_2O_3 and magnetite Fe_3O_4. All the lines represent equilibrium between different species (Fortuné, 2009; Pourbaix, 1974; Revie and Uhlig, 2008).

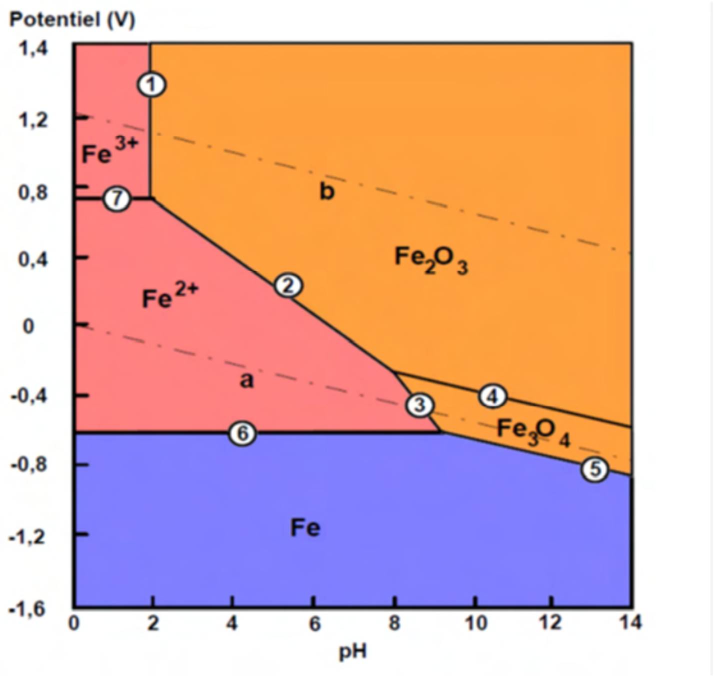

Figure 1-2 Pourbaix diagram for Iron

Horizontal lines on Pourbaix diagram show equilibrium of a reaction in which pH plays no rule, i.e. neither H^+ nor OH^- are involved in the reaction, as in the following reaction:

<u>Line 6:</u> shows the equilibrium between Fe and Fe^{2+} ,

$$Fe \leftrightarrow Fe^{2+} + 2e^- \qquad \textit{Eq. 1.8}$$

$$E = E° - 2.303\,\frac{RT}{nF}\,log\,[\frac{1}{Fe^{2+}}] = -.440 + .0296\ log\ (Fe^{2+})$$

A vertical line shows equilibrium of reaction in which no electron transfer is occurred so potential change plays no rule, and H^+ and OH^- ions are involved in reaction.

$$2Fe^{3+} + 3H_2O \leftrightarrow Fe_2O_3 + 6H^+ \qquad \textit{Eq. 1.9}$$

$$K = \frac{(H^{+})^{6}}{(Fe^{3+})^{2}} = log\,k = 6\,log\left(H^{+}\right) - 2log\left(Fe^{3+}\right) = -6pH - 2log(Fe^{3+})$$

$log(Fe^{3+}) = -.72 - 3pH$, *taking* Fe^{3+} = $10^{-6}\,mol.\,l^{-}$, we have $pH = 1.76$.

Other lines on Pourbaix diagram give the equilibrium as shown in following equations.

Line 2: $2Fe^{2+} + 3H_2O \leftrightarrow Fe_2O_3 + 6H^{+} + 2e^{-}$ *Eq. 1.10*

$E\,(V) = 0.728 - 0.1773\,pH - 0.059\,log[Fe^{2+}]$ $\quad E(V) = 1.082 - .1773\,pH$

Line 3: $3Fe^{2+} + 4H_2O \leftrightarrow Fe_3O_4 + 8H^{+} + 2e^{-}$ *Eq. 1.11*

$E\,(V) = 0.980 - 0.2364\,pH - 0.0886\,log[Fe^{2+}]$ $\quad E\,(V) = 1.512 - 0.2364\,pH$

Line 4: $2Fe_3O_4 + H_2O \leftrightarrow 3Fe_2O_3 + 2H^{+} + 2e^{-}$ *Eq. 1.12*

$E\,(V) = 0.221 - 0.059\,pH$

Line 5: $3Fe + 4H_2O \leftrightarrow Fe_3O_4 + 8H^{+} + 8e^{-}$ *Eq. 1.13*

$E\,(V) = 0.085 - 0.059\,pH$

Line 6: $F_e \leftrightarrow Fe^{2+} + 2e^{-}$ *Eq. 1.14*

$E\,(V) = -0.440 + 0.0295\log[Fe^{2+}]\;E\,(V) = -0.617$

Line 7: $Fe^{2+} \leftrightarrow Fe^{2+} + e^{-}$, $\quad E\,(V) = -0.771$ *Eq. 1.15*

Two inclined dotted lines a & b shown in Figure 1-2, these lines distinguish the three important regions,

I. All metals having ionic concentration 10^{-6} $mol.\,l^{-1}$, whose equilibrium potential is located below the line a, are attacked by water with evolution of hydrogen.

$$M + zH_2O \leftrightarrow M^{2+} + zOH + \frac{z}{2}H_2$$

II. All metals having ionic concentration 10^{-6} $mol.l^{-1}$, whose equilibrium potential is located between the lines a and b are attacked in presence of oxygen in the reaction:

$$M + \frac{z}{4}O_2 + \frac{z}{2}H_2O \leftrightarrow M^{z+} + zOH^-$$

III. All metals having ionic concentration 10^{-6} $mol.l^{-1}$, whose equilibrium potential is located above the line b, are thermodynamically stable.

The oxides formed during the attack at a metal may protect the metal from further corrosion, so metal remains in passive state, and this rust is called passive layer of oxides. In the case of an attack at a metal by water at $25\,°\,C$, Pourbaix diagrams can define theoretical areas of immunity, passivation and corrosion of the metal. The Pourbaix diagram gives no account on the rate of an electrochemical reaction, it only gives the thermodynamic considerations (Cefracor, n.d.; Perez, 2004; Revie and Uhlig, 2008).

1.2 Kinetics Involved in Corrosion Process

1.2.1 Butler-Volmer kinetics

Thermodynamics explains the concept of corrosion tendency, but it does not give any idea on rate of corrosion, which is measured by kinetics principles. In practice we are interested in the rate at which the corrosion reaction is taking place. The rate of a chemical reaction can be defined as the number of moles of atoms reacting per unit time and per unit surface of an electrode. In the case of an electrochemical reaction, which involves charge transfer, the rate of reaction (corrosion) is calculated in terms of equivalent current or charge transfer rate, which can presented by Eq. 1.16 (Cefracor, n.d.; Redaelli et al., 2006; Warkus and Raupach, 2006)

$$j\ =\ n\,F\,v \qquad \textit{Eq. 1.16}$$

Where;

j : Current density of charge-transfer ($A.m^{-2}$)

n : number of mole of electron

F : Faraday constant ($96500 Col.mol^{-1}$)

v : rate of reaction ($mol.s^{-1}.m^{-2}$)

Applying this formula to the oxidation-reduction reaction representative of the corrosion of any metal at equilibrium.

$$Red\ \leftrightarrow O_X +\ ne^+ \qquad \textit{Eq. 1.17}$$

When this equilibrium is disturbed by either anodic or cathodic polarization, the reaction rates are given by Arrhenius law.

Anodic reaction rate: $k_{red}\, C_{red}\, exp\,(-\Delta Ga^{*})/RT$ *Eq. 1.18*

Cathodic reaction rate: $k_{Ox}\, C_{Ox}\, exp\,(-\,\Delta Gc^{*})/RT$ *Eq. 1.19*

$$\Delta Ga^{*} = \Delta Ga_{ch} - \alpha nF\,\eta \quad \text{Eq. 1.20}$$

$$\Delta Gc^{*} = \Delta Gc_{ch} + (1 - \alpha)\, nF\,\eta \quad \text{Eq. 1.21}$$

Where k_{red} and k_{ox} are reduction and oxidation reaction rate constants respectively, C_{red} and C_{Ox} are concentrations of reacting species, ΔGa^{*} and ΔGc^{*} are activation energies of anodic and cathodic reactions respectively, R is the gas constant and T is the temperature in Kelvin (K). The electrochemical Gibbs energy of activation can be decomposed into the Gibbs chemical activation energy ΔG_{ch} (which does not depend on the potential) and electrical energy of charge transfer. The η represents the change in potential at the metal-electrolyte interface ($\Delta E = E - E_{rev}$), and α is the coefficient of charge transfer ($0 < \alpha < 1$), which reflects the ratio of charge transfer between the two partial reactions, anodic and cathodic. The reaction rates can be expressed by the anodic and cathodic current densities, given below,

$$j_a = zFK_{red}C_{red}\, exp\left(-\frac{\Delta Ga_{ch}}{RT}\right) exp\left(\frac{\alpha nF}{RT}\eta\right) \quad \text{Eq. 1.22}$$

$$j_c = zFK_{Ox}C_{Ox}\, exp\left(-\frac{\Delta Gc_{ch}}{RT}\right) exp\left(-\frac{(1-\alpha)nF}{RT}\eta\right) \quad \text{Eq. 1.23}$$

For a reversible electrode at equilibrium, the current density becomes the exchange current density, that is

$$j_o = zFK_{red}C_{red}\, exp\left(-\frac{\Delta Ga_{ch}}{RT}\right) = zFK_{Ox}C_{Ox}\, exp\left(-\frac{\Delta Gc_{ch}}{RT}\right) \quad \text{Eq. 1.24}$$

$$j = j_a - j_c = j_0\left[exp\left(\frac{\alpha nF}{RT}(E - E_{rev})\right) - exp\left(-\frac{(1-\alpha)nF}{RT}(E - E_{rev})\right)\right] \quad \text{Eq. 1.25}$$

The Eq. 1.25 is called Butler-Volmer equation for an electrode reaction. This relation between current density and overpotential is valid only when reaction is governed only by charge transfer, and concentration polarization has no effect *(Cefracor, n.d.; Revie and Uhlig, 2008)*.

1.2.2 Polarization Behavior

The kinetics of the electrochemical reactions at the interface between electrodes and electrolyte can be quantified by current-potential curves, also known as polarisation curves shown in Figure 1-3. These curves are expressed as Butler-Volmer relations between current density and over potential. When at equilibrium, the anodic and cathode currents are equal to each other and no net current flows through the system (electrode), i.e. the over potential is zero (Perez, 2004; Revie and Uhlig, 2008).

$$j_0 = |j_a| = |j_c| \qquad \textit{Eq. 1.26}$$

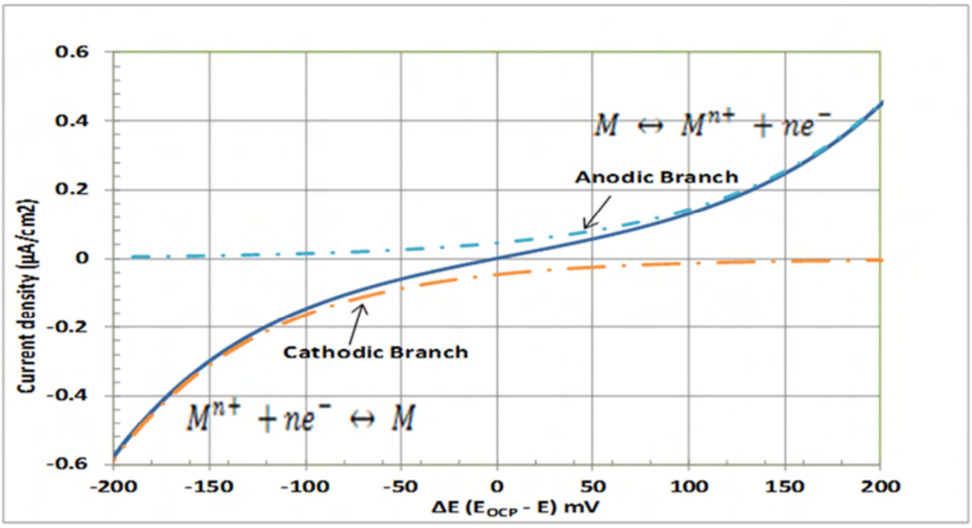

Figure 1-3 Polarization curve according to Butler-Volmer equation

1.2.3 Tafel Slope Constants

When there is sufficient overpotential, the anodic or cathode current becomes negligible depending upon whether the over potential is positive or negative respectively (Gareth Kear, 2005). When η is anodic, that is positive, the second term in the Butler-Volmer equation becomes negligible and the anodic current density (j_a) can be expressed by Eq. (1.27) and its overpotential in Eq. (1.28), with β_a obtained by plotting log $|j|$ versus η (Figure 1-4) (Kim and Kim, 2008).

$$j = j_a = j_0 exp[\frac{\alpha nF}{RT}\eta_c] \qquad \textit{Eq. 1.27}$$

$$\eta = \eta_a = \beta_a log(\frac{j_a}{j_o}) \qquad \textit{Eq. 1.28}$$

$$\beta_a = 2.303\frac{RT}{\alpha nF} \qquad \textit{Eq. 1.29}$$

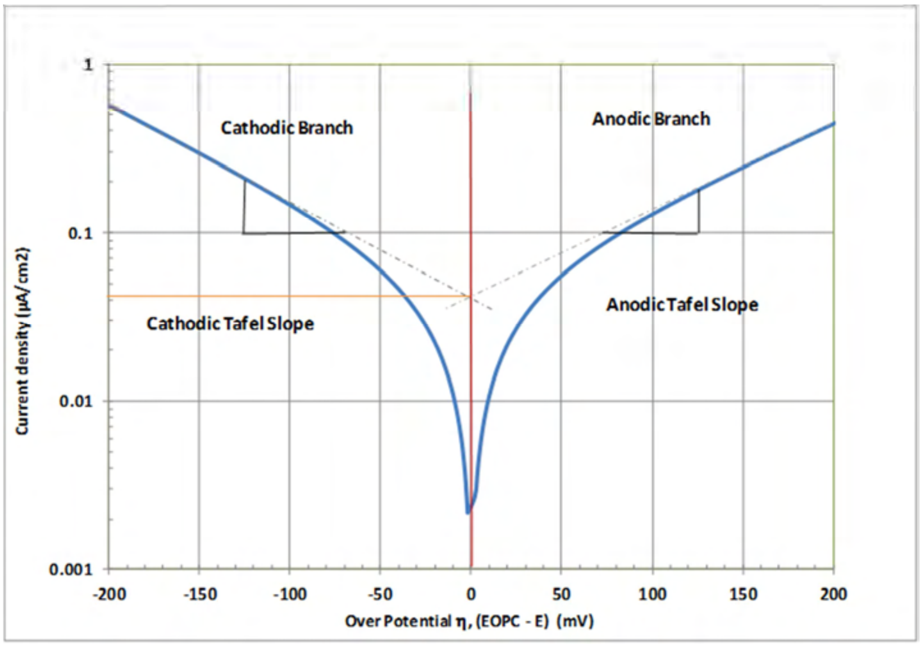

Figure 1-4 Plot of log | j | against η or Tafel plot showing the exchange current density can be obtained with the intercept

Similarly, when η is cathodic, that is negative, the first term in the Butler-Volmer equation becomes negligible and the cathodic current density (j_c) can be expressed by a simpler equation Eq. (1.30).

$$j = j_c = j_0 exp[(1-\alpha)\frac{nF}{RT}\eta_c] \qquad \textit{Eq. 1.30}$$

$$\eta = \eta_c = \beta_c log(\frac{j_c}{j_o}) \qquad \textit{Eq. 1.31}$$

β_c is the cathodic Tafel slope coefficient described in Eq. 1.32. It can be obtained from the slope of a plot of log $|j|$ against η, as shown in Figure 1-4. The intercept between the two straight lines yields the value for j_0 (Kear and Walsh, 2005).

$$\beta_c = -2.303 \frac{RT}{(1-\alpha)nF} \qquad \textit{Eq. 1.32}$$

1.2.4 Faradays Law

Faradays law is used to quantify the mass loss due to corrosion. To determine the life of a structure it is necessary to evaluate the mass loss as a function of time.

$$m = \frac{A.J_{corr.t}}{nF} \qquad \textit{Eq. 1.33}$$

A: Atomic mass of metal (g)
J_{corr}: Intensity of corrosion current (Amp)
t: Time (sec)
n: Number electrons
F: Faradays constant 96500 $Coul./mole$

Mass loss is proportional to the corrosion current, mass is measured in mm/year (Ha-Won Song, 2007; Nasser, 2010).

1.3 Corrosion of steel in Concrete

Corrosion in concrete is due to ingress of chloride ions to the steel surface or carbonation of concrete cover. The pH of concrete pore solution is normally above 12. In such an alkaline environment, an oxide film is formed on steel surface, which protects steel from corroding. It is referred to as steel passivation. Both carbonation and chloride ingress cause this oxide film to breakdown (Broomfield, 2007; Elsener et al., 2003), steel is then depassivated and corrosion process is initiated. The corrosion of steel in concrete is essentially an electrochemical process involving two half-cell reactions occurring simultaneously at steel surface (Figure 1-5). The anodic reaction is the oxidation of iron in aqueous environment, represented by the following half-cell reaction (Eq.1.34) (Ahmad, 2009; Elsener et al., 2003).

$$Fe \leftrightarrow Fe^{2+} + 2e^{-} \qquad \textit{Eq. 1.34}$$

To preserve electro-neutrality, electrons produced by this anodic reaction are consumed by oxygen reduction reaction at cathodic sites on the steel surface Eq. (1.35) (Andrade and Alonso, 2004).

$$\frac{1}{2}O_2 + H_2O + 2e^{-} \leftrightarrow 2OH^{-} \qquad \textit{Eq. 1.35}$$

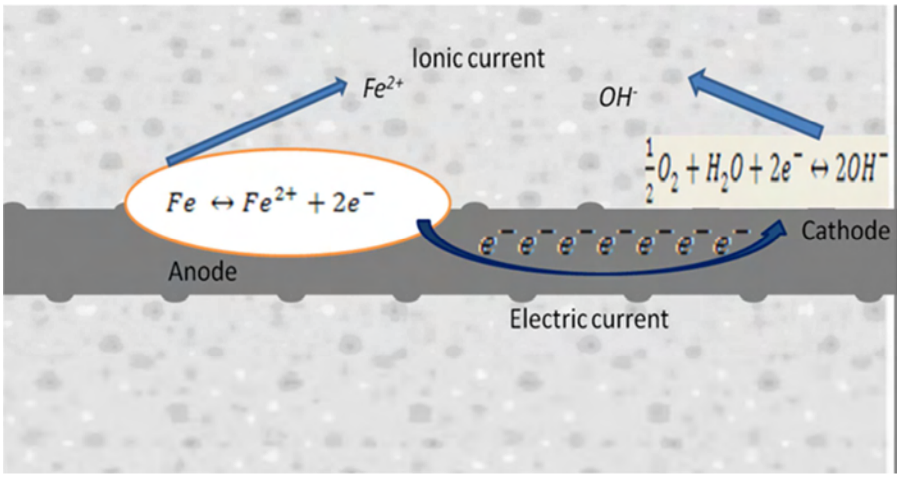

Figure 1-5 Schematic diagram of corrosion process in concrete

The Addition of Eq. 1.34 to Eq 1.35 results in Eq 1.36, where Fe^{2+} ions react with hydroxide ion OH^- and produce ferrous hydroxide $(Fe(OH)_2)$, which forms on the surface of the reinforced steel (Figure 1-6). At the outer surface of this oxide layer, oxygen reacts with the ferrous hydroxide to form hydrous ferric oxide or ferric hydroxide, as represented by Eq (1.37). Ferric hydroxide then becomes hydrated ferric oxide Eq (1.38). The majority of ordinary rust consists of hydrous ferric oxide and is orange to red-brown in colour (Ahmad, 2009; Broomfield, 2007; Roberge, 2000).

$$Fe^{2+} + 2OH^- \rightarrow Fe(OH)_2 \qquad \text{Eq. 1.36}$$

$$4Fe(OH)_2 + O_2 + 2H_2O \rightarrow 4Fe(OH)_3 \qquad \text{Eq. 1.37}$$

$$2Fe(OH)_3 \rightarrow Fe_2O_3.H_2O + 2H_2O \qquad \text{Eq. 1.38}$$

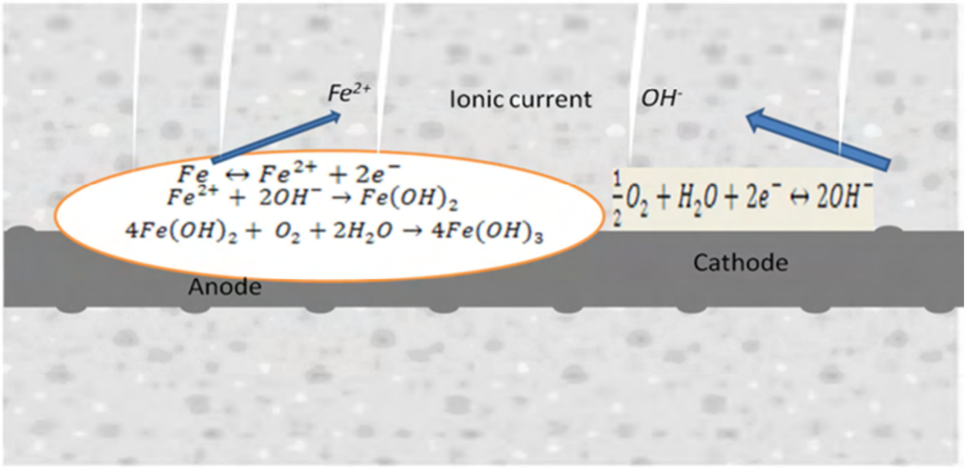

Figure 1-6 Schematic of rust production at steel-concrete interface

Unhydrated ferric oxide Fe_2O_3 has a volume of about twice that of the steel it replaced when fully dense. When it becomes hydrated it swells even more and becomes porous. The volume is increased two to ten times at the steel-concrete interface (Nasser, 2010). This leads to the cracking and spalling that we observe as the usual consequence of corrosion of steel in concrete, rust in the bar and the rust stains could be seen easily at cracks in the concrete (Broomfield, 2007).

1.3.1 Causes of Corrosion in Concrete

1.3.1.1 Carbonation of Concrete

Carbonation is the result of the interaction of carbon dioxide gas in the atmosphere with the alkaline hydroxides in the concrete. Like many other gases carbon dioxide dissolved in water to form an acid. Unlike most other acids the carbonic acid does not attack the cement paste, but just neutralizes the alkalis in the pore water, mainly forming calcium carbonate that lies in the pores (Fortuné, 2009; Haselbach, 2009).

$$CO_2 + Ca(OH)_2 \rightarrow CaCO_3 + H_2O \qquad \textit{Eq. 1.39}$$

Normally there is a lot of calcium hydroxide in the concrete pores than can be dissolved in the pore water. This helps maintain the pH at its usual level of around 12 or 13 as the carbonation reaction occurs. However, eventually all the locally available calcium hydroxide ($Ca(OH)_2$) reacts, precipitating the calcium carbonate and allowing the pH to fall to a level where steel will corrode (Broomfield, 2007). The carbonation can occur even when the concrete cover depth to the reinforcing steel is high. This may be due to a very open pore structure where pores are well connected together and allow rapid CO_2 ingress. It may also happen when alkaline reserves in content, high water cement ratio and poor curing of the concrete. Carbonation depth is the average distance, from the surface of concrete or mortar where the carbon dioxide has reduced the alkalinity of the hydrated cement (Poursaee, 2007). A carbonation front proceeds into the concrete following the laws of diffusion (Broomfield, 2007). The carbonation depth is considered to be dependent on square root of time, and a coefficient which takes account of the concrete conditions.

$$x = K\sqrt{t} \qquad \textit{Eq. 1.40}$$

Where:

x carbonation depth, t is time and K is the diffusion coefficient.

K depends upon the concrete quality, temperature, RH% and the CO_2 concentration around concrete. Depending on the concrete quality and curing condition, the carbonation depth is different (Balayssac et al., 1995). The depth of carbonation can be determined by different techniques. As carbonation reduces the pH, therefore determination pH of concrete by applying pH indicators such as phenolphthalein to a freshly fractured or freshly cut surface of concrete can be used to estimate the depth of carbonation. Upon application of phenolphthalein, noncarbonated areas turn red or purple while carbonated areas remain colorless. Maximum color change to deep purplish red occurs at pH of 9.8 or higher. Below 9.8 the colour may be pink and at pH of 8 colorless (Verbeck, 1958).

1.3.1.2 Chloride ingress in concrete

Chloride ions can be present in the concrete due to the use of chloride contaminated components or the use of $CaCl_2$ as an accelerator when mixing the concrete, or by diffusion into the concrete from the outside environment (Broomfield, 2007). A localized breakdown of the passive layer occurs when sufficient amount of chlorides reach reinforcing bars, and the corrosion process is then initiated. Chlorides in concrete can be either dissolved in the pore solution (free chlorides) or chemically and physically bound to the cement hydrates and their surfaces (bound chlorides). Only the free chlorides dissolved in the pore solution are responsible for initiating the process of corrosion.

1.3.2 Uniform Corrosion

When anode and cathode sites are microscopically small and spatially indistinguishable, i.e oxidation of iron and reduction of oxygen are happening simultaneously at same place, the corrosion is said to be uniform corrosion (Marques and Costa, 2010). Anodically and cathodically acting surface location is not fixed and randomly changed with the time (Figure 1-7). This case is often encountered when corrosion is initiated by carbonation of concrete (Nasser et al., 2010; Warkus et al., 2006). Whole surface of affected steel is corroded homogenously.

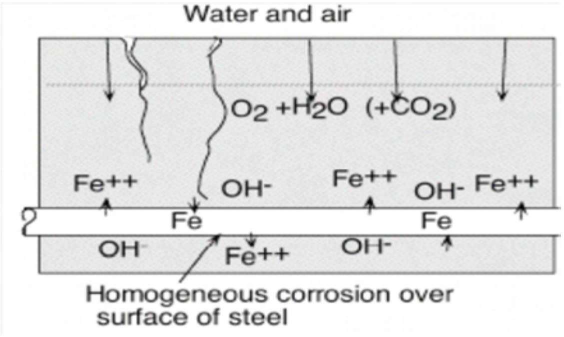

Figure 1-7 Schematic of uniform corrosion in concrete (Hansson et al., 2007)

1.3.3 Localized corrosion

Other form of corrosion observed on steel surface in concrete is localized or pitting corrosion. Where corrosion is concentrated on a particular area and loss in cross section of steel is much higher than that in uniform corrosion. Anode and cathode sites are spatially distinguishable i.e they are easily identified by electrochemical potential measurements. This form is normally observed in chloride induced corrosion. Figure 1-8 shows the schematic of uniform and localized corrosion phenomena (Elsener et al., 2003).

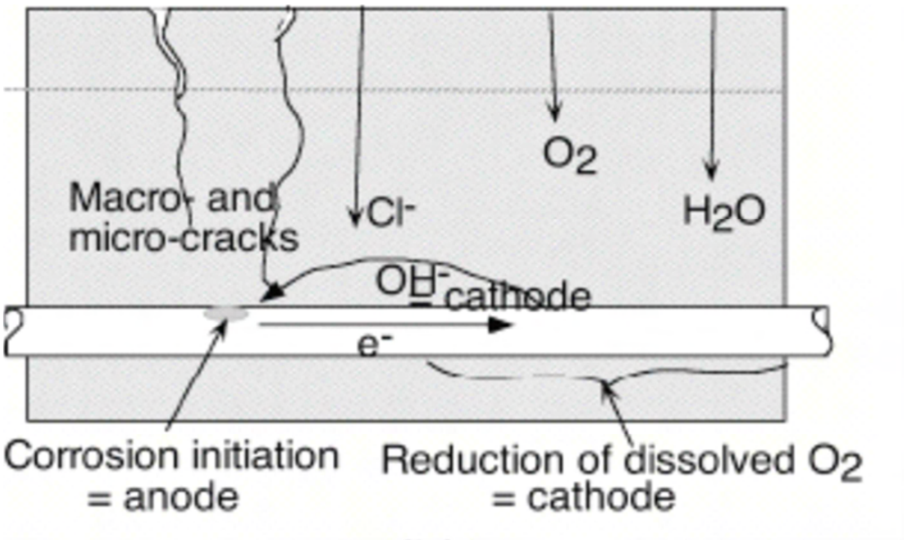

Figure 1-8 Schematic of localized corrosion in concrete (Hansson et al., 2007)

1.4 Corrosion measurement Techniques

For measurement of the corrosion rate of reinforcing steel in concrete many electrochemical and non-destructive techniques are available, which help to monitor the corrosion of steel in concrete structures. Following are some common techniques used to assess the reinforced corrosion:

1. Half Cell Potential Measurement Technique
2. Linear Polarization Resistance Technique (LPR)
3. Tafel Extrapolation
4. Electrochemical Impedance Technique

1.4.1 Half-cell Potential

The half-cell potential measurement is practical and widely employed technique to identify the presence of corrosion in reinforced concrete structures. The corrosion potential E_{corr} (half-cell rebar potential) is measured as potential difference (or voltage) against a reference electrode (Figure 1-9). As a corrosion detection technique, this was first used by Richard Stratful (Stratfull, R. F, 1957). The numerical value of the measured potential difference between the steel in concrete and the reference electrode will depend on the type of reference electrode used and on the corrosion condition of the steel in concrete. In addition, half-cell potentials of steel in concrete cannot be measured directly at the steel-concrete interface due to the presence of the concrete cover (Figure 1-9), the potentials are thus influenced by ohmic drop in the cover (Elsener et al., 2003; Ha-Won Song, 2007).

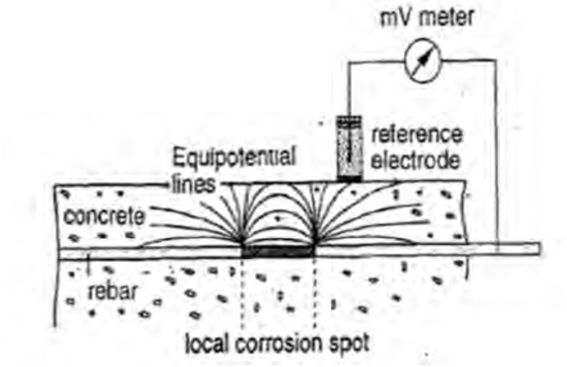

Figure 1-9 Schematic showing basics of the half-cell potential measurement technique

To measure half-cell potential a connection has to be made with the steel bar as shown in Figure 1-9. The reinforcing steel bar is connected to the positive terminal of a high impedance voltmeter, and the reference electrode is connected to the negative terminal. In this arrangement half-cell potential readings generally will be negative. The occurrence of positive potentials is possible on a passive rebar in dry concrete.

It is essential to quote always which type of reference electrode being used for half-cell potential measurements. The Table 1-1 presents the reference electrodes used in practice, with their defined constant and reproducible potential versus the standard hydrogen electrode (SHE) are used (ASTM C876-09, 2009).

Table 1-1 Selected half-cell electrodes used in practice, their potentials, given versus the Standard Hydrogen Electrode (SHE) at 25 ◦C and temperature coefficients (Nygaard, 2009).

Half-cell electrode	Potential (mV/SHE)	Temperature dependency (mV/°C)
Copper /Copper-sulfate sat. (CSE)	+ 0.318	0.90
Saturated Calomel (Hg/Hg_2C1_2) KCl (SCE)	+ 0.241	0.22
Silver/Silver-chloride (Ag/AgCl) KCl sat. (SSCE)	+ 0.199	0.09

For onsite work, the saturated copper/copper-sulfate electrode is most common and is sufficiently accurate, although errors may arise due to contamination of the concrete surface with copper sulphate. Saturated calomel electrode (SCE) and silver/silver-chloride electrodes (Ag/AgCl) are used more in laboratory work. The base potential of the reference electrodes depends on the concentration of the electrolyte, thus care has to be taken to operate in saturated conditions. The temperature dependence of the reference electrodes has no practical influence on the readings on site.

The potential obtained is analyzed to determine whether the steel is corroding or not. Potential survey can be carried out at different points and measurement can be done for large number of points. Half-cell potential survey can primarily indicate whether or not the steel embedded in a structure is corroding and the areas where the corrosion activity is greatest. The ASTM standards (ASTM C876-09, 2009) and RILEM recommendations (RILEM TC154-EMC) (Elsener et al., 2003) are established standards for half-cell measurement and as per standards probability of corrosion is as in Table 1-2.

Table 1-2 Corrosion condition related with half-cell potential (HCP) measurement

Half-cell Potential		Corrosion condition
(mV vs. SCE)	(mV vs. CSE)	
< -426	< -500	Severe corrosion
< -276	< -350	High (<90% risk of corrosion)
-126 to -275	-350 to -200	Intermediate corrosion risk
> -125	> -200	Low (10% risk of corrosion)

Since half-cell potential value is defined as the thermodynamic measure of the ease of removing electrons from the metal in steady state condition, it can not be used as direct measurement of corrosion rate. It should be noted that half-cell potential is the probability of the corrosion activity while corrosion current density j_{corr} is the direct measurement of corrosion rate. The measured half-cell potentials can be affected by several factors which should be considered in their interpretation. A simple comparison of the half-cell potential data with the ASTM guidelines on steel reinforcement corrosion probability could cause mistakes in the evaluation of the structure. It has been accepted by the people who work in the field that a more negative reading of potential means a higher probability of corrosion. But as explained above, this general rule may not always be correct. Some precautions are necessary in interpreting the data from half-cell potential measurements because there are many factors that may affect the magnitude of the potentials. For example, a surface layer with high resistance gives less negative surface potential which may cover underlying corrosion activity (Elsener et al., 2003). And the cathodic polarization due to the lack of oxygen results in more negative potentials while the corrosion rate is reduced (Gu P., 1998). (Soleymani and Ismail, 2004) mentioned that very high moisture content can decrease the half-cell potential to -1000 mV vs. CSE, while corrosion does not exist at all. (Feliú et al., 1996) found that generally there is a poor correlation between half-cell potential values and corrosion current density measured by polarization resistance method.

1.4.2 Linear Polarization Resistance Technique (LPR)

This technique is mostly widely used and has become a well-established for determining the corrosion rate of reinforcing steel in concrete. The advantage of this technique is that it is rapid and non-intrusive, requiring only localized damage to the concrete cover to enable an electrical connection to be made to the reinforcing steel.

1.4.2.1 Basic Theory

First Stern and Geary (Stern and Geary, 1957) based on the general principles of electrochemistry, formulated the fundamentals of corrosion rate values from the recording of the polarization curves around the E_{corr}. The proposed technique is derived from the approximation to a linear behavior of the logarithmic dependence of potential and current when they are recorded around the corrosion (mixed) potential Figure 1-10. So the LPR technique is based on the observation of the linearity of the polarization curves just around E_{corr} , that is, the slope of the polarization curves just around E_{corr}. Corrosion current density at steel surface in concrete is at equilibrium during free corrosion conditions, and at this point potential is called E_{corr} this condition is shown by the polarization curves, now if this state is disturbed by applying overpotential ΔE, a net current ΔI starts flowing in the system, the polarization resistance R_p of reinforced steel is ratio between ΔE and ΔI (Andrade and Alonso, 2004, 1996).

$$R_p = \frac{\Delta E}{\Delta I} \qquad \textit{Eq. 1.41}$$

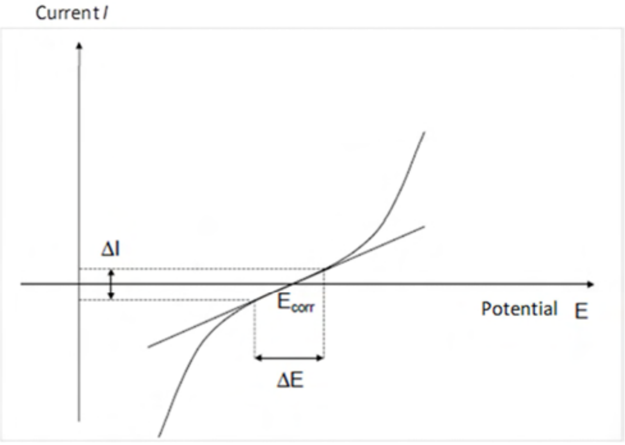

Figure 1-10 Polarization curve has a linear portion, where ΔE has linear relation with ΔI.

The applied voltage should not be more than 20 mV as to remain in the linear zone of polarization curve, if applied voltage is higher than recommended one, then polarization can fall in nonlinear zone of curve and this theory not valid any more (Andrade and Alonso, 2004). The instantaneous corrosion current density i_{corr}, is obtained by dividing a constant B, by R_p value,

$$i_{corr} = \frac{B}{Rp} \qquad \textit{Eq. 1.42}$$

Where $i_{corr} = \Delta I/S$, S is the steel surface area which is polarized, i_{corr}has units of µA/cm^2, R_p is expressed in $\Omega.cm^2$, B is Stern-Geary constant and expressed in volts (V). B depends on Tafel slope constants, and given as:

$$B = \frac{\beta_a \cdot \beta_c}{2.303(\beta_a+\beta_c)} \qquad \textit{Eq. 1.43}$$

Where βa and βc are anodic and cathodic Tafel slope coefficients respectively, and are taken in mV/dec.

1.4.2.2 Equipment required for Rp measurements

Three electrode arrangements is required to measure R_p, with reinforcing steel as working electrode as shown in Figure 1-11, a counter electrode CE (auxiliary electrode) which injects the polarization current in concrete, and a reference electrode RE to measure the potential shift in positive or negative direction. Guard rings are used when confinement of polarizing current is required. The state of steel corrosion can be interpreted by corrosion current i_{corr} measured (Ha-Won Song, 2007). To confine the injected current to a specific steel surface area guard rings are used as shown in Figure 1-12. The confinement of the current can lead to precise measurement of linear polarization resistance.

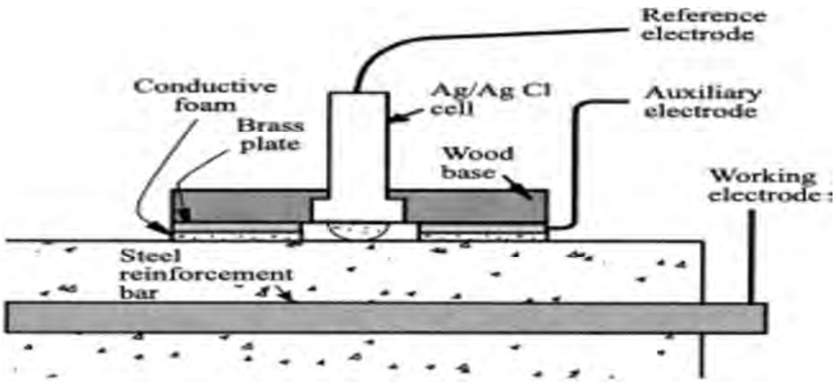

Figure 1-11 Equipment and measurement set up for LPR technique

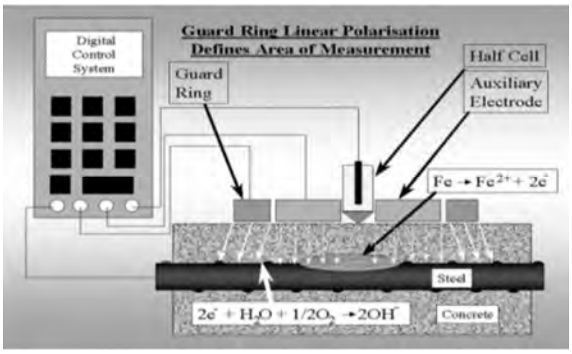

Figure 1-12 Linear polarization resistance measurements with confining guard rings (Ha-Won Song, 2007)

Table 1-3-Corrosion condition according to the current calculated with Linear Polarization Resistance

Corrosion current (j_{corr})	**Condition of the rebar**
< 0.1 µA/cm^2	Passive condition
0.1 - 0.5 µA/cm^2	Low to moderate corrosion
0.5 - 1.0 µA/cm^2	Moderate to high corrosion
> 1.0 µA/cm^2	High corrosion rate

1.4.3 Tafel Extrapolation Technique

Tafel 1905 proposed the most frequent used law in electrochemistry called after him the Tafel law (Kear and Walsh, 2005), according to which logarithm of current density in an electrochemical reaction varies with electrode potential (log i ~ E). This law was first empirically observed and became the first electrochemical technique used for measuring corrosion current density (I_{corr}) and subsequently corrosion rate. It is based on the extrapolation (Figure 1-13) of the cathodic and anodic branches of the polarization curve till the value of E_{corr}. Its use was very limited due to its destructive nature, as a new bar is needed for each measurement due to the alterations produced during the polarization of the anodic branch.

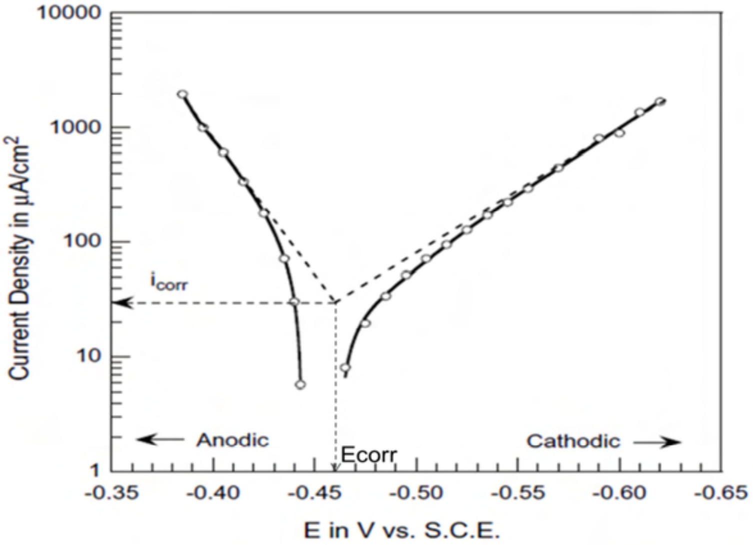

Figure 1-13 Polarization curve to measure Tafel slope coefficients and corrosion current density (McCafferty, 2005).

1.4.4 Electrochemical Impedance Spectroscopy

The electrochemical impedance spectroscopy (EIS) method is very useful in characterizing an electrode corrosion behavior. The electrode characterization includes the determination of the polarization resistance, corrosion rate and electrochemical mechanism (Ismail and Ohtsu, 2006). The usefulness of this method permits the analysis of the alternating current (AC) impedance data, which is based on modeling a corrosion process by an equivalent electrical circuit. The method allows the characterization of an electrochemical system in a nondestructive way, of both the diffusion of aggressive species within the cement-based materials and the kinetics of electrochemical reactions that occur on the steel (electrode) surface (Poupard et al., 2004).

The EIS technique is based on a transient response of an equivalent circuit for an electrode/solution interface. The response can be analyzed by transfer functions due to an applied small-amplitude potential excitation ΔE at varying signals or sweep rates. In turn the potential excitation yields current response ΔI and vice verse. So a sine-wave perturbation of small amplitude (20-50mV) is employed on a corroding system being modeled as an equivalent circuit for determining the corrosion mechanism and the polarization resistance (Feliu et al., 1998). The potential signal and current response can be expressed by Eq. 1.44 and Eq. 1.45.

$$E(t) = |\Delta E|.\sin(\omega t) \qquad \text{Eq. 1.44}$$

$$I(t) = \Delta I.cos(\omega t) = |\Delta I|.sin(\omega t - \varphi) \qquad \textit{Eq. 1.45}$$

Where: ω is angular frequency and equal to $2\pi f$, f is frequency in Hz, t is time in $s.|\Delta E|$ is the amplitude of potential signal. Impedance of any electrochemical interface is commonly depicted as a complex function, having both real and imaginary components. We can also use complexes numbers to present impedance (Perez, 2004).

$$E(t) = \Delta E.exp(j\omega t) \qquad \textit{Eq. 1.46}$$

$$I(t) = \Delta I.exp(j\omega t - \varphi) \qquad \textit{Eq. 1.47}$$

$$Z\,(\omega) = \frac{|\Delta E|}{|\Delta I|}\,.exp(j\varphi) \qquad \textit{Eq. 1.48}$$

φ is phase angle between current response and potential perturbation. Impedance in Cartesian system can be expresses as real and imaginary coordinates.

$$Z(\omega) = Re(Z) + \,jIm(Z) \qquad \textit{Eq. 1.49}$$

In a complex plan it can present by |Z| vector and phase angle.

$$|Z(\omega)| = \sqrt{Re[Z(\omega)]^2 + Im[Z(\omega)]^2} \qquad Eq.\ 1.50$$

$$\varphi(\omega) = arctan(\frac{Im(Z)}{Re(Z)}) \qquad Eq.\ 1.51$$

The impedance is usually plotted in the Nyquist diagram, in which at each excitation frequency, the real part is plotted on the x-axis and the imaginary part is plotted on the y-axis. The real part represents the faradic current i.e the electronic current of an electrochemical reaction, and the imaginary part reflects the contribution of ionic charge of the reaction. Normally analysis of impedance graph is done by relating it to an equivalent circuit model. For concrete a simple equivalent circuit as shown in Figure 1-14 (Song, 2000a), where Re is resistance of electrolyte (concrete) between the two electrodes (working electrode and counter electrode). C_{dl} is represents the capacitance of double layer near the steel concrete interface. R_{CT} is the resistance to charge transfer.

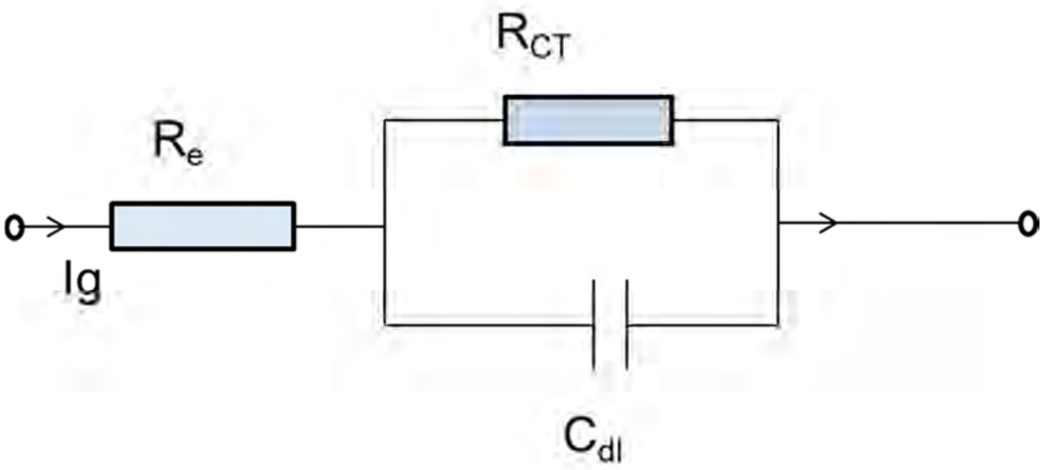

Figure 1-14 Equivalent circuit for concrete sample

The impedance of such a model can be expressed as following equation.

$$Z = R_e + \frac{R_{CT}}{1+j\omega C_{dl}(R_{CT})} \qquad Eq.\ 1.52$$

Graphical representation on Nyquist plot is given the Figure 1-15.

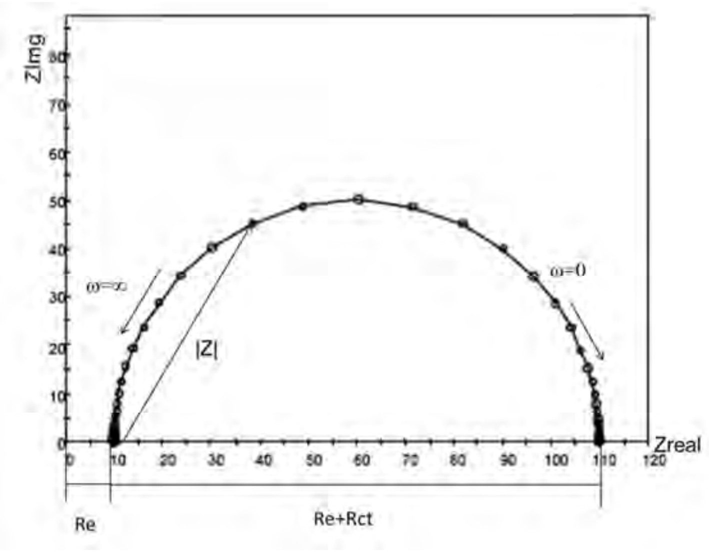

Figure 1-15 Nyquist plot for a simple corroding system.

The salient features of the spectrum are labeled as follows:

Re: Electrolyte resistance given by the high-frequency limit of the diagram,

R_{CT}: Charge transfer resistance given by the diameter of the high-frequency loop.

Although this typical behavior has not been systematically checked experimentally, researchers have agreed to describe the impedance spectra in three distinct features over a large frequency domain (1 MHz–10 MHz): high, intermediate and low frequencies.

1.5 Simulation of Reinforced concrete corrosion

The research has been carried out over the years to develop the models which are suitable to assess corrosion in reinforced concrete. Some of these models are based on empirical methods and correlate the corrosion rate to parameters like concrete resistivity, temperature and relative humidity. Other types of models are based on a quantification of the on-going electrochemical processes. Corrosion consists of two stages initiation period, and propagation period. Whereas the initiation stage of corrosion, i.e. chloride ingress and carbonation of concrete cover, has received considerable attention during recent years. Numerous publications are also available on modelling and simulation of propagation phase of reinforcement corrosion using numerical models, taking the polarization behaviour of anodically and cathodically acting steel surfaces into account (Warkus and Raupach, 2006; Warkus et al., 2006).

Numerical modelling of steel corrosion in concrete has its own challenges that can be summarized under the following categories:

1. Estimation of parameters to carry out the simulations,
2. Numerical difficulties in the solution of governing equations due to nonlinear boundary conditions,
3. And challenges in the modelling of complicated geometries (e.g. reinforcement details) and non-homogeneous material properties.

Numerical models of corrosion are often based on Boundary Element Methods (BEM) or Finite Element Methods (FEM). In BEM only the interfaces involved in the problem are considered. In FEM also the bulk phase of the concrete and if desired also the steel can be modelled (Redaelli et al., 2006). Therefore with FEM all three aspects, interfacial properties, transport through and changes of the concrete and the geometrical design can be accounted for. This constitutes the drawback of BEM compared to FEM, bulk properties cannot be modelled explicitly but can be accounted for implicitly at best. Draw backs of FEM however is that for practical situations the numerical size of the model can become impractically large.

1.5.1 Empirical Models

Empirical models are based on assumed direct relationships between the corrosion rate of the reinforcement and basic parameters of the concrete like w/c-ratio, type of binder, etc. and the exposure conditions considering water content, chloride content and temperature of the concrete.

In DuraCrete an empirical model is advocated in which concrete resistivity, ρ_{con}, serves as the major material parameter:

$$i_{corr} = \frac{k_o}{\rho_{con}} F_{Cl}.F_{Galv}.F_{Oxid}.F_{O2} \qquad \textit{Eq. 1.53}$$

This expression takes into account the influence of chloride content, galvanic interactions, oxide (rust) layers, and oxygen supply by adding correction factors (Raupach, 2006).

1.5.2 Numerical Models

A vast amount of publications are available for modelling the propagation phase of reinforcement corrosion, taking the polarisation behaviour of anodically and cathodically acting steel surface areas into account.

1.5.2.1 Equivalent Resistor model

Such models vary from simple resistor network models to complex 2- or 3-dimensional finite element (FEM) or boundary element (BEM) models. Same kind of model is proposed by Warkus et al., (2006) in which electrochemical corrosion process is compared to an equivalent electrical circuit, which contains different types of resistances. One resistance is given by the electrolytic resistivity of the surrounding concrete (Figure 1-16).

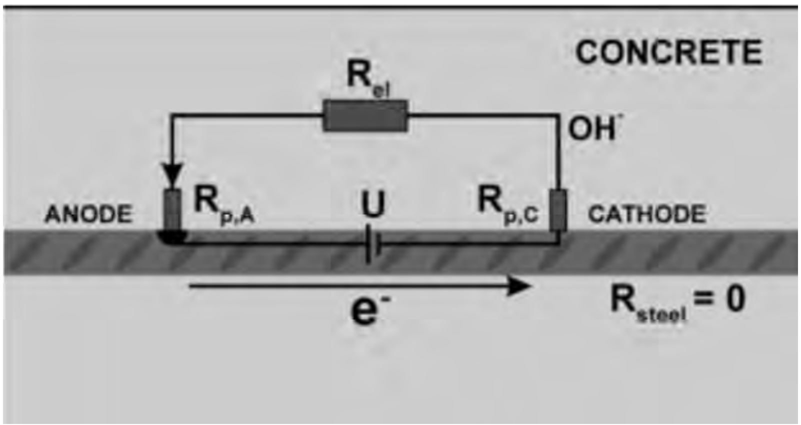

Figure 1-16 Simplified model of reinforced corrosion

The corrosion current is expressed as,

$$Icorr = \frac{U}{R_{P,A}+R_{p,C}+R_{el}} \qquad \text{Eq. 1.54}$$

Icorr: corrosion current: [A]

U: driving voltage: [V]

Rp,A: polarisation resistance of the anode: [ohm]

Rp,C: polarisation resistance of the cathode: [ohm]

Rel: electrolytic resistance: [ohm]

Mass loss of metal can be calculated by using Faradays law.

1.5.2.2 Models based on Butler-Volmer Equation

Many researchers, e.g. (Isgor and Razaqpur, 2006; Kim and Kim, 2008; Raupach, 2006; Redaelli et al., 2006; Warkus et al., 2006) have presented numerical models in which Butler-Volmer equation is used to model the polarization behaviour of steel concrete interface. Butler-Volmer equation explains the kinetics of half-cell reaction taking place at steel surface as presented in equation Eq 1.33 & Eq. 1.34 i.e.

Anodic reaction,

$$Fe \ \rightarrow Fe^{2+} + 2e^-$$

Cathodic reaction,

$$\frac{1}{2}O_2 + H_2O + 2e^- \rightarrow 2OH^-$$

$$j = j_{corr}\left[exp\left(\frac{log(10)(E-Ecorr)}{\beta a}\right) - exp\left(-\frac{log(10)(E-Ecorr)}{\beta c}\right)\right]$$

j_{corr}: Corrosion current density [µA/m^2]

E_{corr}: Free corrosion potential [mV]

β_a: Anodic Tafel constant [mV/dec]

β_c: Cathodic Tafel constant [mV/dec]

In these models, the flow of an electrical charge in a medium as a result of a potential field is modelled by using Ohm's law, which describes the current density is proportional to the gradient of the potential and inversely proportional to the resistivity.

$$\boldsymbol{j} = -\frac{1}{\rho}\ \nabla E \qquad \textit{Eq. 1.55}$$

Assuming electrical charge conservation and isotropic conductivity, the potential distribution is represented by the Laplace's equation. Following is the Laplace equation for potential distribution in an electrolyte,

$$\nabla^2 \phi = 0, \qquad \frac{\partial^2\phi}{\partial x^2} + \frac{\partial^2\phi}{\partial y^2} = 0 \qquad \textit{Eq. 1.56}$$

$$\phi = E - Ecorr \qquad \textit{Eq. 1.57}$$

The Laplace-equation is a partial differential equation of second order. An analytical solution for this equation can only be derived in case of certain geometries and boundary conditions. As it is not possible for arbitrary geometries, one has to use numerical means to calculate an appropriate approximation (Warkus and Raupach, 2006).

1.5.2.3 Modified Butler-Volmer Equation

The Butler-Volmer equation is valid for metals in liquid media, if no diffusion control is taken into account. This requirement is not always accomplished in case of reinforcement corrosion, because especially in dense or wet concrete having a think cover, a lack of oxygen can appear at the cathodic surface and then diffusion control will become important. To consider this effect the Butler-Volmer equation can be modified by incorporating the limiting cathodic current density i_{lim} (Kim and Kim, 2008; Warkus and Raupach, 2006).

$$i_N = \frac{1 - exp(-\frac{ln(10).(\phi - \phi_{corr})}{bc}}{\frac{1}{i_{corr} - \frac{exp(-\frac{ln(10).(\phi - \phi_{corr})}{bc}}{i_{lim}}}} \qquad \textit{Eq. 1.58}$$

The effect of concentration polarization on the cathodic reaction can be significant since the oxygen concentration around the cathodic sites on the steel surface are low, resulting in further polarization. The polarization of the cathodes due to oxygen concentration can be presented by,

$$\eta_{c,c} = -\frac{RT}{nF} ln \frac{i_L}{i_L - i_c} \qquad \textit{Eq. 1.59}$$

i_L: is limiting current due to oxygen concentration

$\eta_{c,c}$: Cathodic polarization due to concentration

Activation polarization of cathode is given as*:*

$$\eta_{c,a} = -\beta_c log \frac{j_c}{j_{cO}} \qquad \textit{Eq. 1.60}$$

Adding,

$$\eta_{c,c} = -\beta_c log \frac{j_c}{j_{cO}} - \frac{RT}{nF} ln \frac{i_L}{i_L - i_c} \qquad \textit{Eq. 1.61}$$

The limiting cathodic current density i_{lim}, which is dependent on the geometrical arrangement of the embedded steel (concrete cover, etc.) and the diffusion properties of the concrete, can be derived from Fick's first law of diffusion (Raupach, 2006; Warkus and Raupach, 2006).

$$i_{lim} = 3.62 * 10^9 \frac{D_{Ox}}{c} . \frac{A_{con}}{A_{steel}} \qquad \textit{Eq. 1.62}$$

i_{lim}:	limiting cathodic corrosion current [A/m^2]
D_{Ox}:	Oxygen diffusion coefficient: [m^2/s]
c:	Concrete cover: [mm]
A_{con}/A_{steel}:	Concrete surface to steel surface ratio, only to take into account if <1

1.5.2.4 Limiting Current

Limiting current during electrochemical reaction comes into account when the dissolved reactants are being consumed or transformed by electron transfer at the electrode; their concentration near the electrode is diminished. A concentration gradient dc/dx will form. Given a reasonably high exchange current density, the reaction rate and thus the current may become limited by rate at which the reactant arrives at the electrode by diffusion. The diffusion limited current density is given by,

$$j = -FD \left[\frac{d_c}{d_x}\right] \qquad \textit{Eq. 1.63}$$

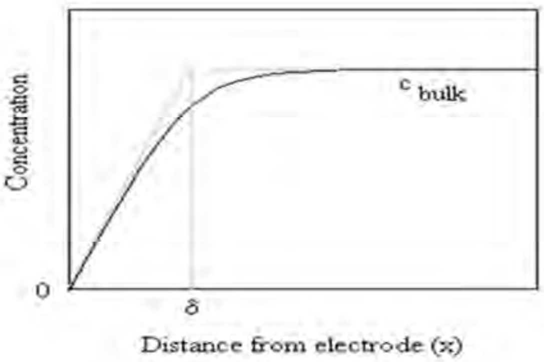

Figure 1-17 Concentration profile of reactants near electrode surface (Tanner's Chemistry, n.d.)

Where F is the Faraday constant in coul.mol^{-1}, D is the diffusion coefficient in cm^{2}.sec^{-1}, and dc/dx is in mol.cm^{-4}. The current density *j* is in coul.cm^{-2} sec^{-1}. In the presence of convection, stirring for example, the bulk concentration will be maintained up to the hydrodynamic stagnant layer at the surface of the electrode. It is in this stagnant layer that the concentration gradient exists. Although there is no sharp distinction between the stagnant and moving regions an approximation is used to give a definite linear quantity to this layer called the Nernst diffusion layer and symbolized by *d*. This is illustrated in Figure 1-17.

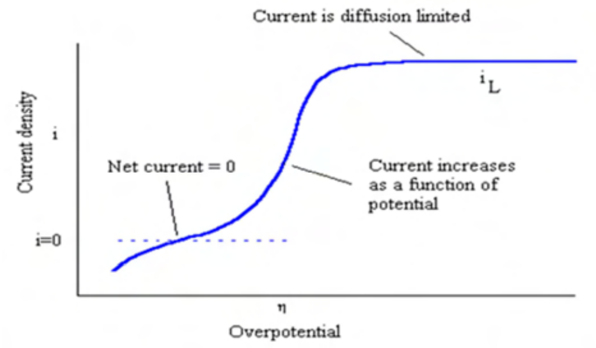

Figure 1-18 Polarization curve showing Limiting current due to diffusion of reactant.

The Butler -Volmer equation seems to indicate that with increasing field strength the current will increase without limit. Of course this is not right as the reaction soon becomes limited by the rate at which the reactant arrives at the electrode. The limiting current density is:

$$j_L = -FD[\frac{C_{bulk}-C_{x=0}}{\delta}] \qquad \text{Eq. 1.64}$$

Which is obviously at a maximum when the concentration at x=0 is zero. In this case the concentration goes from the bulk concentration to zero. The relationship between the Butler-Volmer equation curve and the effect of diffusion limited current is shown in Figure 1-18 (Tanner’s Chemistry, n.d.).

1.6 Accelerated Corrosion Testing

Normally concrete provides a good resistance to corrosion due it's another important characteristic i.e. the high alkalinity of the pore solution, which is comprised of mainly sodium and potassium hydroxides, with a pH ranging from 12.6 to 13.8. At this pH level a protective (or passive) film is spontaneously formed during the early stages of cement hydration. This passive film may grow to a thickness of the order of 10^{-3} to 10^{-1} μm and contains hydrated iron oxides (Ramachandran et al., 2001). The theory of the existence of this passive layer is based on indirect evidence of anodic polarization measurement. There is still much to be learned concerning this passive film, such as the conditions of its formation, and its chemical and mineralogical composition. It is possible that this passivation film consists of several phases (Smith, 2007). The concrete cover also provides good physical protection to steel from chloride ions and prevents carbonation. So it takes a long time for steel to depassivate and allow corrosion process to start. That makes it very difficult to replicate, study and to understand the corrosion phenomena in laboratories. To overcome this problem Accelerated Corrosion Tests are developed, by using them we can induce corrosion in reinforced concrete samples in laboratory in short period of time (Ahn, 2001; Yingshu et al., 2007).

Tuutti (Tuutti, K, 1982) proposed a corrosion model; according to which the corrosion process can be divided in two distinct time phases: initiation phase and propagation phase Figure 1-19. The initiation phase corresponds to the progressive ingress of the aggressive agents like carbon dioxide CO_2 and chloride ions Cl^- through the concrete cover. As previously discussed, concrete provides excellent protection for steel reinforcement thanks to the high alkalinity of concrete pore solution. The quality of the concrete cover is also involved in the physical protection of steel from environment, because concrete transport properties control the ingress kinetics of aggressive agents. During this phase, no corrosion occurs and it usually takes many years for aggressive agents to reach steel surface and depassivate steel (Yingshu et al., 2007).

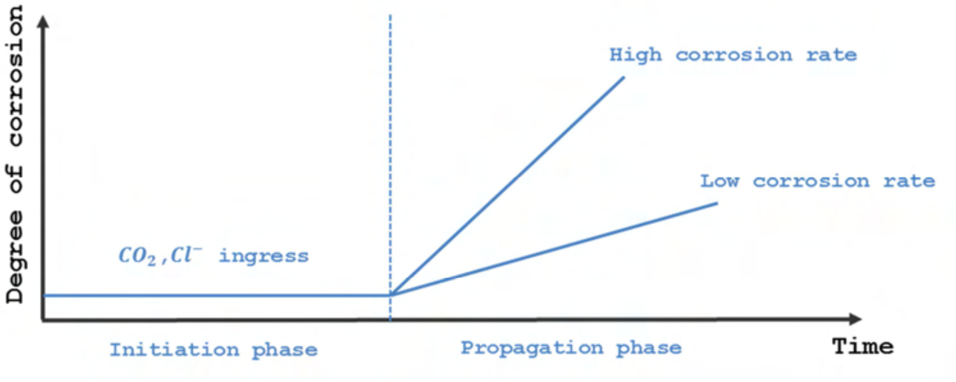

Figure 1-19 Tuutti corrosion model

The laboratory acceleration of corrosion is primarily consists on the acceleration of the initiation phase so that the depassivation of steel is quickly achieved.

1.6.1 Artificial Climate Technique

In this technique corrosion process is accelerated by way of high temperature, high humidity, and repeated wetting-and drying cycles. Artificial environment techniques, in which the samples are kept in controlled environment, are often used to accelerate initiation period. The artificial climate conditions given by (Yingshu et al., 2007) are temperature $T = 40\,°C\ (104\,°F)$, relative humidity $(RH) = 80\%$, and salt water ($5\%\,NaCl$ solution) spraying (1 hour) and infrared light shining (7 hours) for the wetting-and-drying cycle. The most commonly used techniques are:

- Carbonation chamber with 50% CO2 and 65% RH,
- Samples contaminated by 3-5% NaCl solution (permanent immersion or wetting-drying cycles).

The corrosion process and corrosion characteristics of the steel bar under artificial environments are similar to that of corrosion under natural environment. Artificial climate environment as an accelerated laboratory test method is more representative than the galvanostatic method.

1.6.2 Impressed current technique/ Galvanostatic method

The impressed current technique consists of applying a constant current from a DC source to the steel embedded in concrete. After applying the current for a given duration, the degree of induced corrosion can be determined theoretically using Faraday's law, or the percentage of actual amount of steel lost in corrosion can be calculated with the help of a gravimetric test conducted on the extracted bars after subjecting them to accelerated corrosion. Using the actual amount of steel lost in corrosion, an equivalent corrosion current density can be determined. At first to depassivate the steel, the samples are immersed in a solution of 3-5% NaCl for specific period of time depending on concrete quality (few weeks to a year) (Ahn, 2001). Then direct electric current is impressed on the steel according to the setup shown in Figure 1-20. The applied impressed current densities have typically ranged from 200 to 3,000 mA/cm^2 with a maximum of 10,400 mA/cm^2 (Almusallam et al., 1996), and a minimum of 45 mA/cm^2 (Lee et al., 2000). The steel bars (main tensile reinforcement in the beam) act as the anode and the stainless bar in the center of the beam section acts as the cathode in the setup, as shown in Figure 1-20.

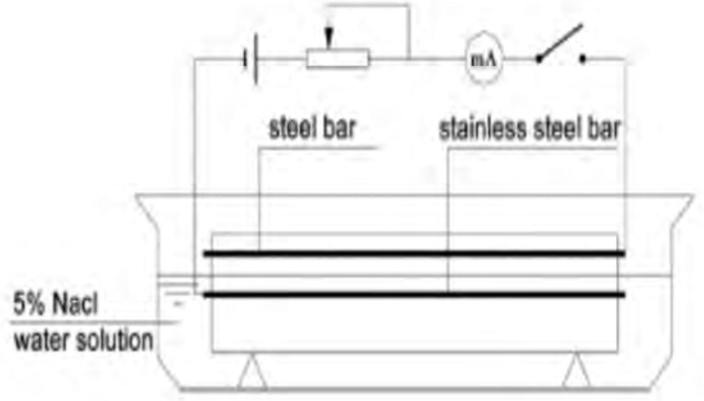

Figure 1-20 Schematic of Galvanostatic technique to induce corrosion (Yingshu Y, 2007)

Many researchers have used these techniques to induce the corrosion in reinforced concrete, and studied the concrete behavior after corrosion is occurred, e.g.

El Maaddawy and Soudki, (2003) performed accelerated corrosion test on concrete prism samples, the acceleration of corrosion was achieved by applying a direct current on the steel reinforcing bars by means of external power supplies. One of these power supplies allow application of a constant current and have a current accuracy of 61% at 500 mA full scale.

They used other two power supplies with a current capacity of 50 mA with an accuracy of 61% at full scale. The current intensity was selected in order to achieve the desired theoretical degree of corrosion of the steel within a certain time frame. Faraday's law was then used to determine the theoretical mass loss. The samples were subjected to current densities of 100, 200, 350, and 500 mA/cm^2, and the time of corrosion was 815, 766, 380, and 306 h, respectively with applied current densities. The circuit was assembled in series for each group, as shown in Figure 1-21. The direction of the current was adjusted so that the reinforcing steel served as the anode, while the stainless steel bar served as the cathode, so those electrons would flow from anode to cathode. After the time required to induce the theoretical degree of corrosion was reached, the steel reinforcing bars were retrieved, cleaned of rust using chemical cleaning procedures according to ASTM G-I-90, (1999), and then weighed to determine the actual mass loss of the steel reinforcing bars. Then the samples were used to measure the concrete strain response due to expansion caused by corrosion products, the influence of varying the applied current density was also observed.

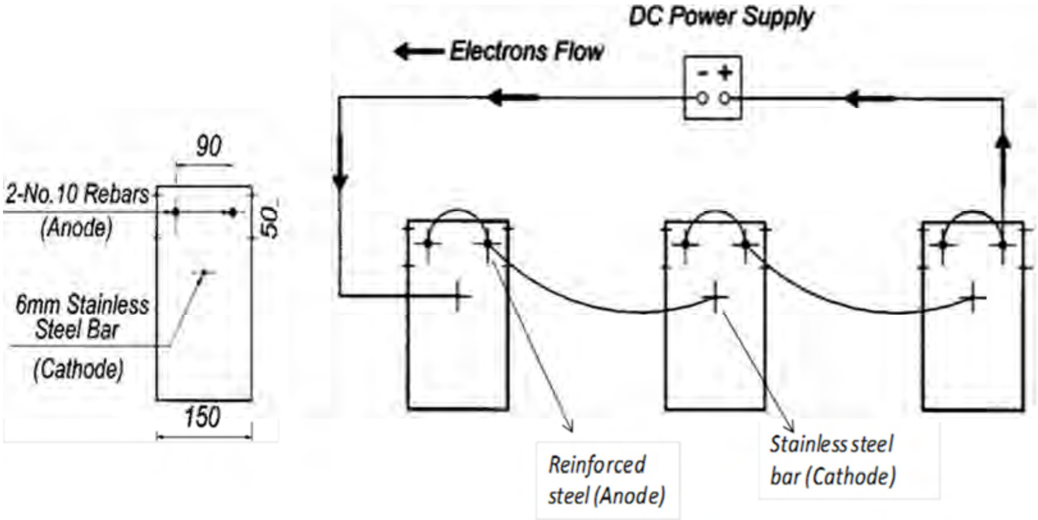

Figure 1-21 Accelerated corrosion test setup used by (El Maaddawy and Soudki, 2003)

Ahn, (2001) have used impressed current technique to induce the corrosion to study the durability of marine concrete structure. They have also galvanostatic technique was used to accelerate reinforcement corrosion by impressing anodic direct current. The beams samples were connected in series with the constant current flowing through all the beams Figure 1-22. Stainless steel bars were used as the counter electrodes; working electrode and counter electrode bars were mounted in parallel near the concrete surfaces in the maximum bending moment region. For the first 30 days the sample were just submerged and no current applied, from 30 to 60 days: 190 mA (current density = 1.721 A/m^2) and 24 mA (0.761 A/m^2) on each of the specimens. From the 60th day to the end of the exposure: 380 mA (3.442 A/m^2) and 48 mA (1.522 A/m^2) for each of the specimens. Current levels applied during the wet cycle were changed to observe the change of behavior of the beams at different current levels.

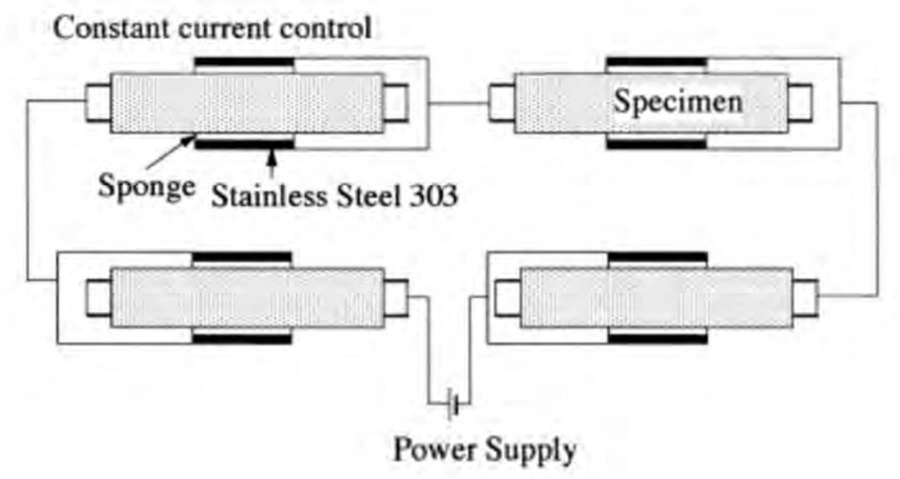

Figure 1-22 Arrangement of Accelerated corrosion test by (Ahn, 2001).

Ahmad, (2009) have also performed accelerated corrosion test. The set-ups used for inducing reinforcement corrosion through impressed current consist of a DC power source, a counter electrode, and an electrolyte. The positive terminal of the DC power source is connected to the steel bars (anode) and the negative terminal is connected to the counter electrode (cathode). The current is impressed from counter electrode to the rebars through concrete with the help of the electrolyte (normally sodium chloride solution). A typical lollypop reinforced concrete test specimen and set-up for accelerated corrosion study using the impressed current technique are shown in Figure 1-23.

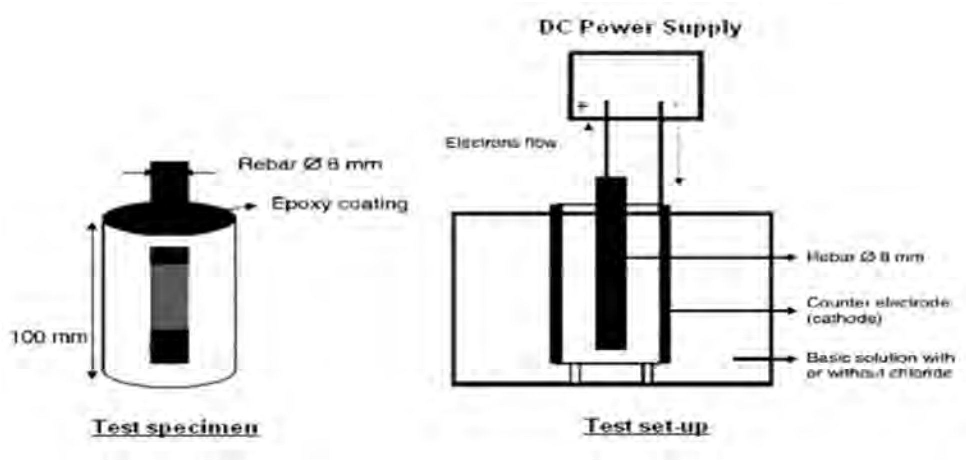

Figure 1-23 Set up used by *(Ahmad, 2009)*

Fortuné, (2009) has performed the accelerated test in laboratory, different types of accelerated corrosion tests were used to induce the corrosion, i.e. impressed current technique, carbonated environment, immersion of samples in chlorinated solution. The purpose was to test the acoustic emission to measure the corrosion.

Depassivation of steel bar in concrete was performed by carbonation, for this purpose the samples were placed in a chamber which is set at an environment of 50% CO2, 60% RH and 20°C. One part of the samples were covered with aluminum sheet to penetration of CO2, this is done to have a sound concrete and passivated steel bars (Figure 1-24). These steel bars serve as cathode afterwards. To get the corrosion in propagation phase cathode bars were connected to anode bars through a resister, as by Figure 1-24-b. The potential difference between two bars creates the electromotive force and electron starts flowing from anode to cathode, and hence corrosion process starts.

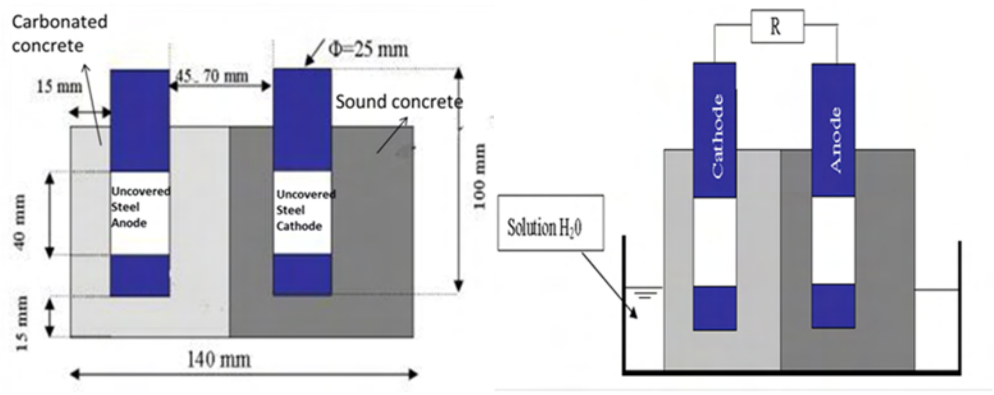

Figure 1-24 Sample geometry for Galvanic corrosion test b) sample is merged into water during the experiments (Fortuné, 2009).

Figure 1-25 Galvanic samples with active and passive bars (Fortuné, 2009)

The accelerated corrosion test designed in this work is an enhancement of Fortuné’s work. A cylindrical geometry is proposed here instead of a rectangular block. Moreover, the fabrication of carboanted concrete was performed separatly, so there was no threat of carbonating the supposedly sound concrete portion. The cylindrical geometry was selected for the reason that when active and passive steel bars are parallel to each the other, the effect of increase in Cathode/Anode surface is significantly larger than to an arrangement where steel bars are coplananr to each other. In addition, the selected geometry also makes it facile to change the Cathode/Anode ratio by just connecting the passive bars to active one.

CHAPTER # 2

2 Characterization of corrosion parameters

2.1 Introduction

This chapter characterizes all the corrosion parameters with respect to the condition of concrete and steel in it, i.e whether concrete is carbonated or sound, or if reinforcement steel is depassivated or in passive state. Moreover the chapter also explains the properties of materials used, the conditioning of concrete samples and the protocol of experiments performed to get the corrosion parameters in carbonated and non-carbonated concrete.

The corrosion parameters like corrosion potential E_{corr}, corrosion current density j_{corr}, anodic tafel slope β_a and cathodic tafel slope β_c are sensitive to different factors like temperature, relative humidity, pH and carbonate contents in the pore solution (Elsener, 2005; Garcés et al., 2005). The researchers who have modeled corrosion in reinforced concrete have used a wide range of the values of β_a & β_c. The variety of values used by different authors, shows the uncertainty exists in selecting these parameters.

For the measurement of linear polarization resistance (LPR) also supposes the values of Stern-Geary constant B between 26 and 52 for active and passive steel respectively. Constant B depends on Tafel slope coefficients and can be calculated with the help of Eq. 1.43. The value of B is 26 when β_a and β_c are $120\,mV/dec$, and B is 52 for β_a infinity and β_c $120\,mV/dec$. But in many of cases, these theoretical values of β_a and β_c could be much different, i.e. anodic Tafel slope of active steel could be much higher than $120\,mV/dec$. With different concrete conditions (RH%, Temperature, oxygen availability, carbonation, chloride contents) the constant B could be from 8 to ∞, so using B as $26\,mV$ and $52\,mV$ can be erroneous (Chang et al., 2008; Song, 2000b). Little literature is available on Tafel slopes (β_a, β_c) for different concrete conditions, especially in case of carbonated concrete.

In addition, to simulate numerically the electrochemical corrosion phenomena in concrete, the corrosion parameters have to be identified for different conditions encountered in real life structures. The literature review again shows uncertainty associated with the selection of corrosion parameters (Butler-Volmer parameters) to be used in simulation. Isgor and Razaqpur, (2006) used β_a values $60\, mV/dec$ for active bar, Gulikers and Raupach, (2006) has used $91\, mV/dec$, Brem, (2004) used $75\, mV/dec$ and Ge and Isgor, (2007) used β_a ranged from $26\, mV/dec$ to $91\, mV/dec$. Similarly, other corrosion parameters also show considerable variations in literature for active and passive conditions.

Bearing in mind this uncertainty, Tafel experiments were performed on carbonated and non-carbonated concrete. Total forty eight lollypop samples were casted with single embedded steel bars at the center, to obtain polarization curves. Twenty four samples were conditioned in order to depassivate the steel bar (Active). Other twenty four samples were kept in normal environmental conditions to have a sound concrete samples with passivated steel bar. The experiments were performed at a temperature 20 ± 3, and concrete samples were in saturated state. The extrapolation of the polarization curves gives Tafel slope coefficients and corrosion current density.

2.2 Experimental Procedure

2.2.1 Material characteristics

The cylindrical concrete samples with $65\, mm$ of diameter and $130\, mm$ of length were casted. The mould used (Figure 2-1) were consisted of two parts, the cylindrical PVC mould having length of $170\, mm$ and $65\, mm$ inner diameter. A cylindrical spacer having $40\, mm$ of length and a diameter of $64\, mm$ was placed at the bottom of the mould (Figure 2-1). A hole of $20\, mm$ diameter was drilled throughout the length of the spacer to adjust the steel bar into the mould.

A plane carbon steel bar of $20\, mm$ diameter with $140\, mm$ of length was used. The chemical composition of steel is given in Figure 2-2 shows the steel bar before and after the mechanical treatment. Higher the water to cement ratio (w/c) higher is the depth of carbonation in concrete in a given time. Hence, a porous concrete with w/c of 0.78 was formulated to achieve early carbonation of concrete sample to save the time in laboratory experiments. The porosity of carbonated and non-carbonated concrete was measured and given in Table 2-2. The Ordinary Portland Cement $CEM\ I\ R$ 52.5 with locally available aggregates was used. The

$0/4\ mm$ sand while $4/12\ mm$ coarse aggregates were used. The formulation of concrete is given in Table 2-2.

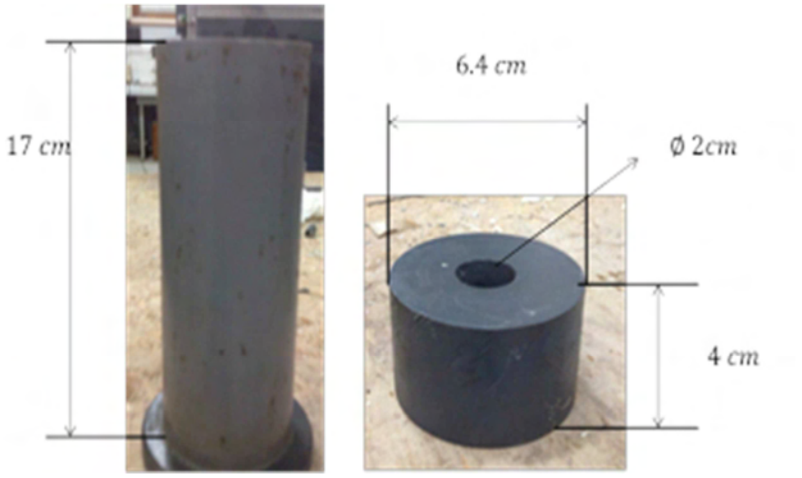

Figure 2-1 Cylindrical mould with spacer

Figure 2-2 a) Steel bar before treatment, oxide layer is covering the steel surface b) Steel bar after mechanical treatment of brushing

Table 2-1- Chemical composition of steel bars (% by weight)

C %	Si%	Mn%	P%	S%
0.45	0.30	0.70	0.035	0.035

Table 2-2- Formulation of Concrete

Cement CEMI 52.5R	(kg/m^3)	280
Water	(kg/m^3)	218
Sand 0/4 mm	(kg/m^3)	854
Gravel 4/12.5 mm	(kg/m^3)	1068
Water-to-Cement	ratio	0.78

2.2.2 Sample preparation

The steel bars were first cleaned with mechanical brushing to remove the oxide layer from the surface. Then the bars were weighted so that at the end of experiments weight loss due to corrosion can be measured and comparison can also be made between gravimetrical weight loss and the weight loss calculated by Faraday's law. Then the bars were mounted into the spacers (Figure 2-3), only $20\ mm$ of steel bar was inserted into the hole of spacer. This $20\ mm$ part of the steel bar was remained outside of the concrete sample and was used for the electrical connections later. The spacers with an inserted steel bar were placed into the cylindrical moulds. Then the concrete was poured into the moulds. To have a uniform concrete around the steel bar, a normal vibration effort by vibrating table was applied until the air bubbles are seen at concrete surface. The final shape and dimension of samples are given in Figure 2-4.

Figure 2-3 Sample preparation before pouring of concrete

2.2.3 Sample conditioning

After 24 hours of casting, the samples were demoulded. The top surface of the samples at which the steel bar was projected outside, was protected with an epoxy resin (Figure 2-4; Figure 2-5). This was to stop the penetration of carbon dioxide from the top surface along the steel-concrete interface. The steel bar portion outside was covered with auto-adhesive aluminum foil to avoid the corrosion of bar during curing and carbonation period. The samples were then placed into the curing chamber for 28 days. After the curing, the samples were kept in the laboratory environment for two weeks for drying before putting them into the carbonation environment.

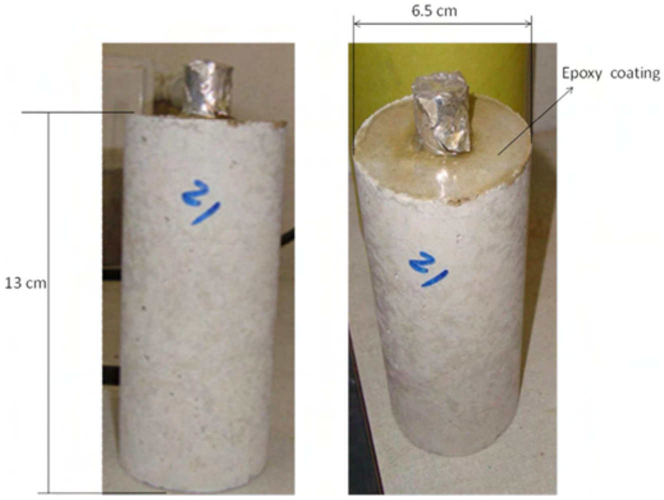

Figure 2-4 Final shape and size of lollypop samples

Figure 2-5 Samples in controlled environment

The samples to be carbonated were then placed into a carbonation chamber, which was set at 50% CO_2, 60 % RH and the temperature was kept at 20 $°C$. The other samples were stored in a room temperature. To follow the carbonation depth five reference samples were casted with the same procedure. They were broken to observe the carbonation depth at a regular interval of time. The samples were completely carbonated in 8 weeks.

To detect the carbonation of concrete, phenolphthalein test was performed; results are shown in Figure 2-6. The spray of phenolphthalein on the broken surface of carbonated sample gave no change in color, which confirmed that the concrete was fully carbonated and pH is less than 9. Moreover, brown rust was visible all around the steel bars and some rust species had travelled into the concrete pores confirming that a corrosion process was started. Some sound concrete samples were also broken to observe if there is any carbonation during these 8 weeks. The steel bars in these sound concrete samples had a shining surface, no corrosion process was occurring. Phenolphthalein spray gave a pink color at broken concrete surface which means that the pH is near 13, and the concrete around the rebar is not carbonated. Only the first few millimeters of the sample were carbonated (Figure 2-7). The porosity of carbonated and non-carbonated samples was determined; the values are given in Table 2-3. During carbonation $\mathrm{Ca}Co_3$ is formed which fills the pores of concrete and hence reduces the porosity (Broomfield, 2007; Poursaee, 2007).

Table 2-3-Porosity of concrete samples (in water)

	Carbonated	Non-Carbonated
Porosity (%)	15.7	18.1

Figure 2-6 Carbonated sample, corrosion products are visible at steel surface and nearby concrete

Figure 2-7 Non- carbonated sample; phenolphthalein test gives a pink color due to higher pH values. Steel bar has a shining surface and no corrosion products.

2.3 Measurement set up

2.3.1 Three electrode set up

The Tafel experiments were performed on carbonated and non-carbonated samples by using Gamry® DC module. The three electrodes arrangement as shown in Figure 2-8 was used to obtain polarization curves. The working electrode (WE) (steel bar in this case) at which the potential is applied and its current response is observed. The counter electrode (CE) which is a titanium grid, it was placed all around the cylindrical concrete samples. The counter electrode (CE) is used to apply either current or potential to polarize the working electrode. The third electrode is a reference electrode (RE), which measures the instantaneous potential E at any time on working electrode. For these experiments the Saturated Calomel Electrode (SCE) was used. The samples were completely saturated before the tests and were submerged into water. To not completely block the oxygen availability, 1 cm of sample was kept out of water (show in Figure 2-8 and Figure 2-9) during the Tafel experiments and corrosion potential measurements.

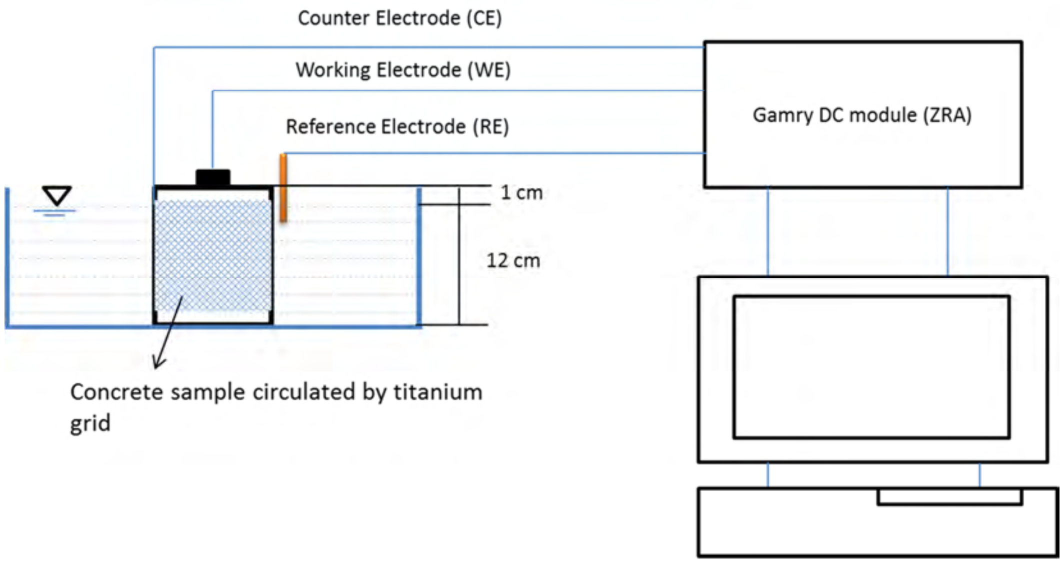

Figure 2-8 Schematic of Three electrode arrangement measurements, b) Experiments underway

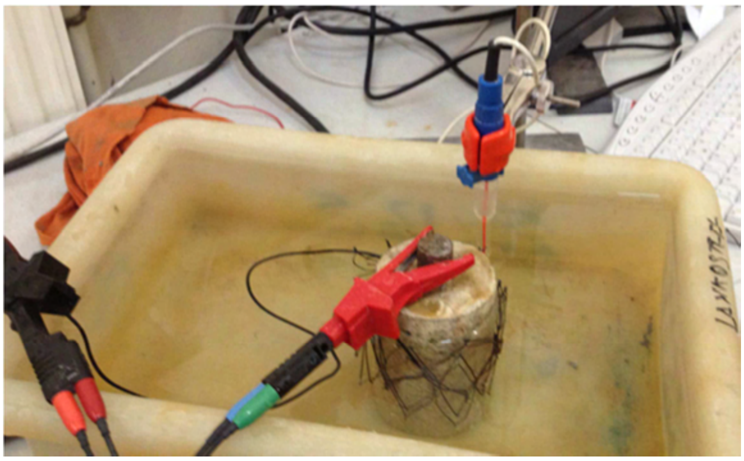

Figure 2-9 Tafel experiment underway

2.3.2 Experimental Program

In total, forty eight samples were tested to measure the corrosion parameters. Twenty four of these samples were subjected to carbonation (Table 2-4), other samples were non-carbonated (Table 2-5). The carbonated samples were named with a number which followed with a letter "C". Similarly noncarbonated samples were designated with a letter "N" after their corresponding number as shown in Table 2-4 and Table 2-5. These samples were tested on three different scan rates, i.e. $0.1, 0.5$ and $0.8\ mV/sec$. The scan rates are selected from available literature on Tafel experiments (Chang et al., 2008; Garcés et al., 2005; Poursaee, 2007). Six carbonated and six non-carbonated samples were tested at each scan rate.

The steel bars were subjected to a cyclic polarization of $-200\ mV\ to\ +200\ mV$ around the corrosion current potential (E_{corr}). Table 2-4 and Table 2-5 show the samples which are tested in these conditions. The selected range of applied polarization was also available in literature (Alonso et al., 2002; Chang et al., 2008). The polarization is applied in one step, i.e. Gamry® directly applies $-200mV$ of polarization with respect to the E_{corr}, and then potential comes back to equilibrium potential (corrosion potential E_{corr}) at a given scan rate, this is called cathodic polarization. Once steel bar is arrived at equilibrium potential, the anodic polarization i.e. E_{corr} to $+200\ mV$ is applied.

The drawback of one step polarization is that the potential of steel bar often does not come back exactly at E_{corr} before starting anodic polarization. Which means the equilibrium could be disturbed with strong cathodic polarization.

In addition some samples were tested under a partial polarization. In these experiments the applied polarization was only in one direction on a sample, i.e. either anodic ($Ecorr + 200mV$) or cathodic ($Ecorr - 200mV$) polarization was applied. Three carbonated and three non-carbonated samples were tested for each type of partial polarization. The scan rate was kept at $0.5mV/s$ for all these applied polarizations. These tests were performed to observe the effect of the polarization procedure (continuous/cyclic) on the polarization curve.

Table 2-4 Carbonated sample with scan rate and type of applied polarization

Sample name	Measured Corrosion Potential (mV/SCE)	Scan rate mV/sec	Type of Polarization Applied
07-C	-645	0.1	Cyclic
16-C	-653	0.1	Cyclic
22-C	-702	0.1	Cyclic
28-C	-642	0.1	Cyclic
42-C	-652	0.1	Cyclic
43-C	-652	0.1	Cyclic
02-C	-665	0.5	Cyclic
17-C	-641	0.5	Cyclic
19-C	-662	0.5	Cyclic
30-C	-676	0.5	Cyclic
40-C	-668	0.5	Cyclic
41-C	-645	0.5	Cyclic
01-C	-658	0.8	Cyclic
06-C	-600	0.8	Cyclic
20-C	-660	0.8	Cyclic
21-C	-662	0.8	Cyclic
34-C	-661	0.8	Cyclic
03-C	-619	0.5	Anodic
04-C	-598	0.5	Anodic
05-C	-554	0.5	Anodic
55-C	-601	0.5	Cathodic
56-C	-613	0.5	Cathodic
57-C	-692	0.5	Cathodic

Table 2-5 Non-carbonated samples with the scan rate and type of polarization applied to them

Name of sample	Measured Corrosion Potential (mV/SCE)	Scan rate (mV/Sec)	Type of polarization
15-N	-186	0.1	Cyclic
51-N	-300	0.1	Cyclic
23-N	-221	0.1	Cyclic
39-N	-186	0.1	Cyclic
53-N	-143	0.1	Cyclic
25-N	-261	0,1	Cyclic
10-N	-253	0.5	Cyclic
14-N	-239	0.5	Cyclic
24-N	-172	0.5	Cyclic
35-N	-218	0.5	Cyclic
47-N	-318	0.5	Cyclic
48-N	-214	0.5	Cyclic
09-N	-223	0.8	Cyclic
26-N	-290	0.8	Cyclic
37-N	-267	0.8	Cyclic
39-N	-186	0.8	Cyclic
46-N	-260	0.8	Cyclic
49-N	-319	0.8	Cyclic
13-N	-157	0.5	Anodic
52-N	-215	0.5	Anodic
12-N	-137	0.5	Anodic
36-N	-148	0.5	Cathodic
38-N	-89	0.5	Cathodic
11-N	-124	0.5	Cathodic

2.3.3 IR Compensation

The polarization curves were recorded without taking the ohmic drop (IR) due the concrete resistance into the account. Gamry® DC module has a function of recoding the log(i) ~ E data after IR compensation calculation. The correction is done based on extrapolation of the current response considering the stationary conditions are achieved. The output is a curve with lots of noise, and it is not possible to extrapolate the curve to obtain the values of corrosion parameters. That is why the IR correction was done manually on the obtained log *(j)* ~ *E* data afterward. The resistance of concrete (R_e) can be measured by galvanostatic pulse technique. The cylindrical samples show the behavior of Randle's equivalent model as shown in Figure 2-10. The model depicts that to an applied current there is electrolytic resistance $R_{e,}$ and then the resistance to charge transfer (Resistance to charge transfer/polarization resistance (R_{ct})) and double layer capacitance (C_{dl}) of steel-concrete interface in parallel to each other. For carbonated and noncarbonated samples a galvanostatic impulse current of 50µA was applied. The resistance of the concrete was calculated by following equation;

$$\frac{\Delta E}{\Delta I} = Re + \left(1 - e^{-\frac{t}{R_{ct} C_{dl}}}\right) R_{ct} \qquad \textit{Eq. 2.1}$$

At initial time t=0, the second term in the Eq. 2.1 becomes zero, and it gives the values of electrolytic resistance. On other hand when t=∞, we have the response in terms of electrolytic resistance plus the resistance to charge transfer. The Figure 2-11 and Figure 2-12 are the galvanic pulse responses of carbonated and non-carbonated concrete samples respectively. E_0 is the initial potential, before the application of current pulse *I*, and E_i is the potential just after the pulse is applied.

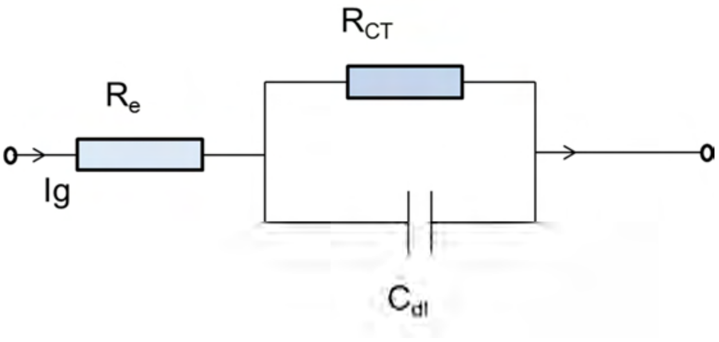

Figure 2-10 Randle's equivalent circuit model for steel in concrete

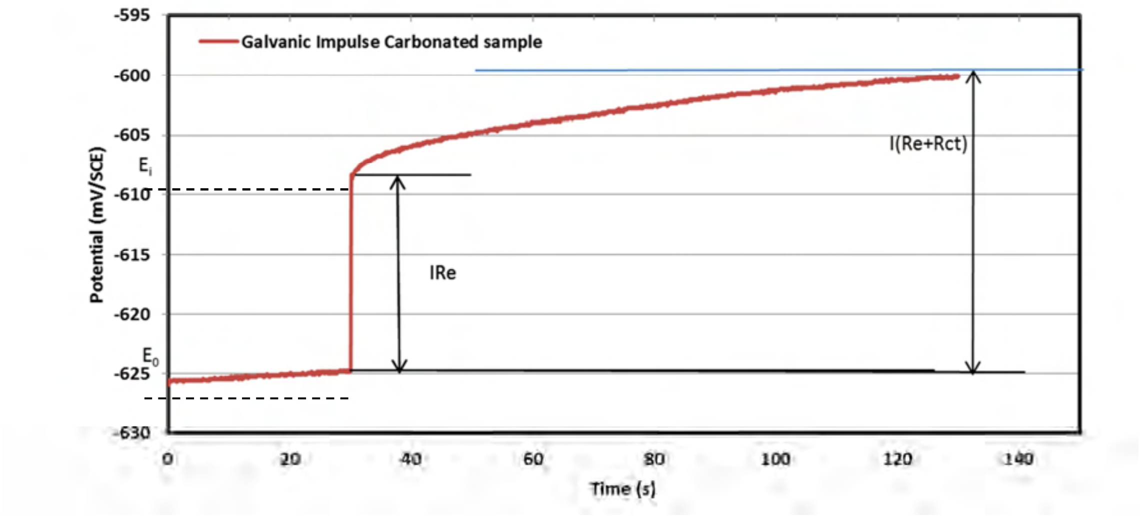

Figure 2-11Response of a carbonated sample to a galvanic pulse of 50μA

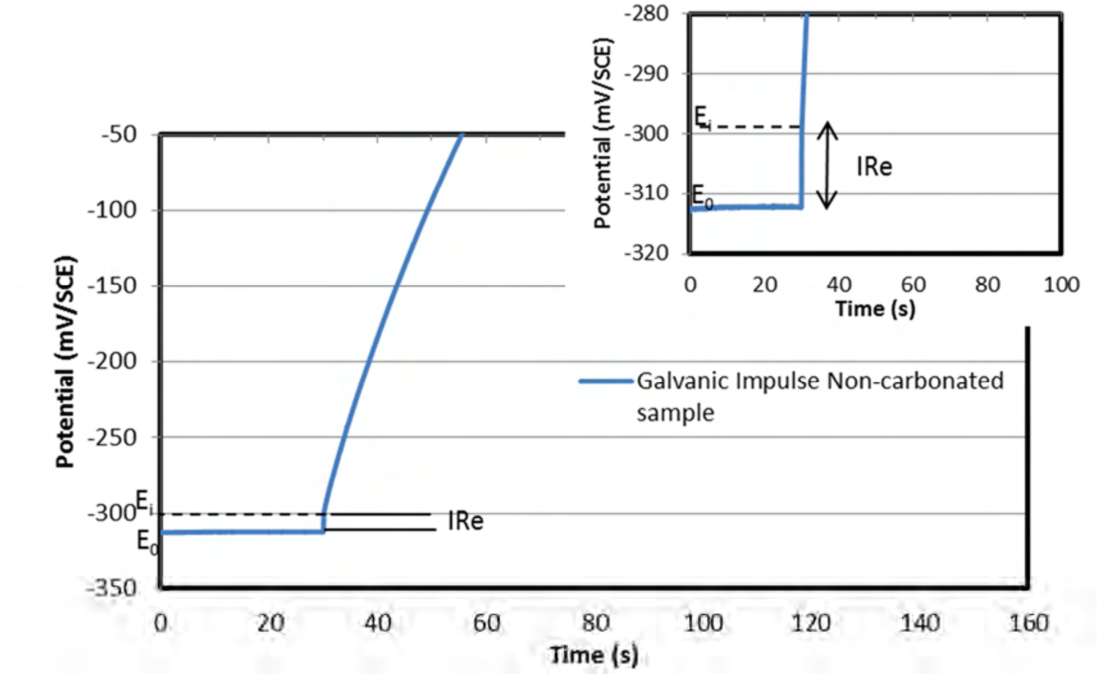

Figure 2-12 Response of a non-carbonated sample to a galvanic pulse of 50μA

The resistance of concrete R_e in case of carbonated concrete was found to be around 350 Ω. While in the case of non-carbonated concrete it was found around 200 Ω. Once the resistance is obtained from galvanic pulse technique, the correction is applied by following relation,

$$Ecorrected = Emeasured \pm I * Re \qquad Eq.\ 2.2$$

The positive correction is applied on cathodic while negative on anodic branch of polarization curve.

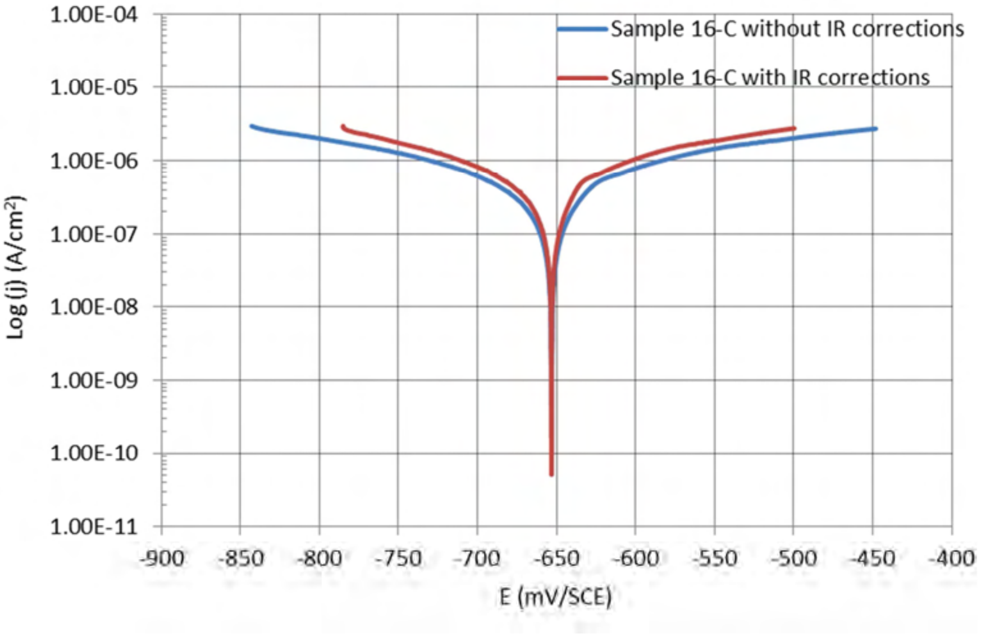

Figure 2-13 Polarization curve of a carbonated sample with and without IR compensation

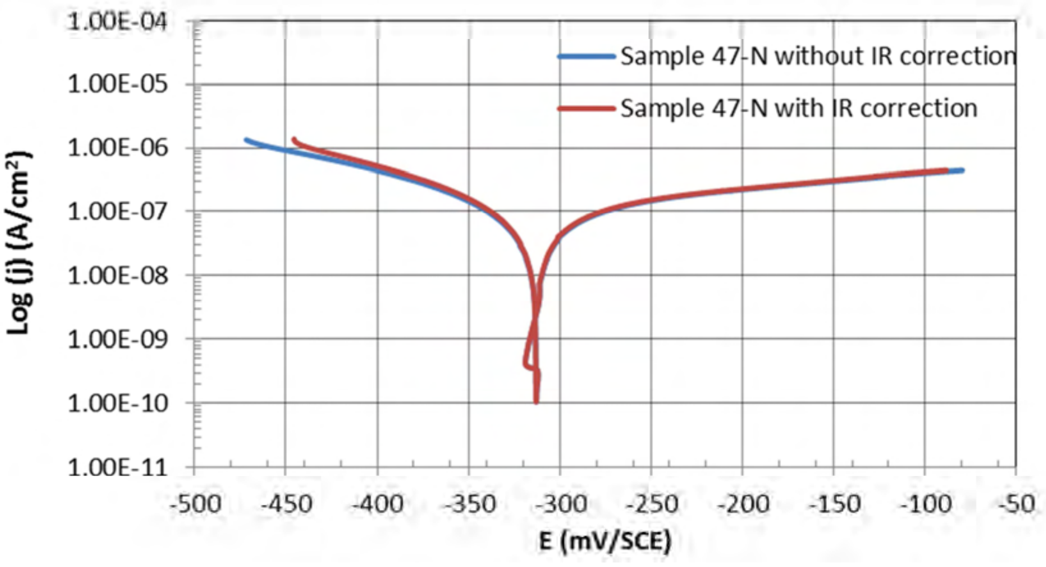

Figure 2-14 Polarization curve of a non-carbonated sample with and without IR compensation

Figure 2-13 and Figure 2-14 show the polarization curves with and without ohmic drop effect for carbonated and non-carbonated concrete samples respectively. In case of carbonated concrete the resistance R_e as well as the current I are higher, so the *IR* effect is rather significant as shown in Figure 2-13. While in noncarbonated concrete the resistance calculated is lower with the current produced is also lower, so the *IR* effect is quiet negligible (Figure 2-14).

2.3.4 Polarization Curves and Extrapolation:

The Tafel experiments in DC module of Gamry® are potentiodynamic tests. To obtain the polarization curves the applied potential on working electrode is plotted on horizontal axis at a linear scale, and the current response of working electrode (steel bar) on y-axis at a log scale. The current values were divided by the steel surface area which was supposed to be polarized, to obtain current density. In this case as 12 cm steel bar was embedded in concrete, and counter electrode was circulated all around the sample such that the whole embedded steel bar was uniformly polarized, so current values were divided by the surface area of 12 cm steel bar.

Figure 2-15 shows a polarization curve obtained by Tafel experiments on a steel bar in carbonated concrete after the IR compensation. Generally the curves are extrapolated by extending the straight lines of linear portions till the corrosion potential as shown in Figure 2-15. The value of corrosion current density is the point where these extended slopes intersect the perpendicular drawn at corrosion potential. Figure 2-16 is a polarization curve for passive steel in a non-carbonated concrete. The cathodic polarization of this steel bar gives a higher current at the start of the scan, this current is called serge current, and it is due to the charging of double layer of steel-concrete interface (Chang et al., 2008).

When the anodic and cathodic tafel slopes are quite different from each other the extrapolation of the polarization curve gives two different points of interception of Tafel slopes at the perpendicular, as in the case of a noncarbonated sample shown in Figure 2-16. The curve gives two values of corrosion current density *Jcorr1* and *Jcorr2*. The one with lower value of these two currents is taken, because this current limits the reaction rate of electrochemical system. The values of all corrosion parameters were at first taken from Tafel extrapolations. Then these values were used to perform curve fitting by using Curvefit tool of Matlab®. The Butler-Volmer model was fitted against experimental values to obtain the more precise corrosion parameter values. The optimization was made in the values of these parameters to obtain the best fit. The values of corrosion parameters obtained through fitting were close to each other and curve fit was in tolerable limits ($R^2 = 0.97$). The curves fit for one carbonated and one noncarbonated sample are shown in Figure 2-17 and Figure 2-18 respectively.

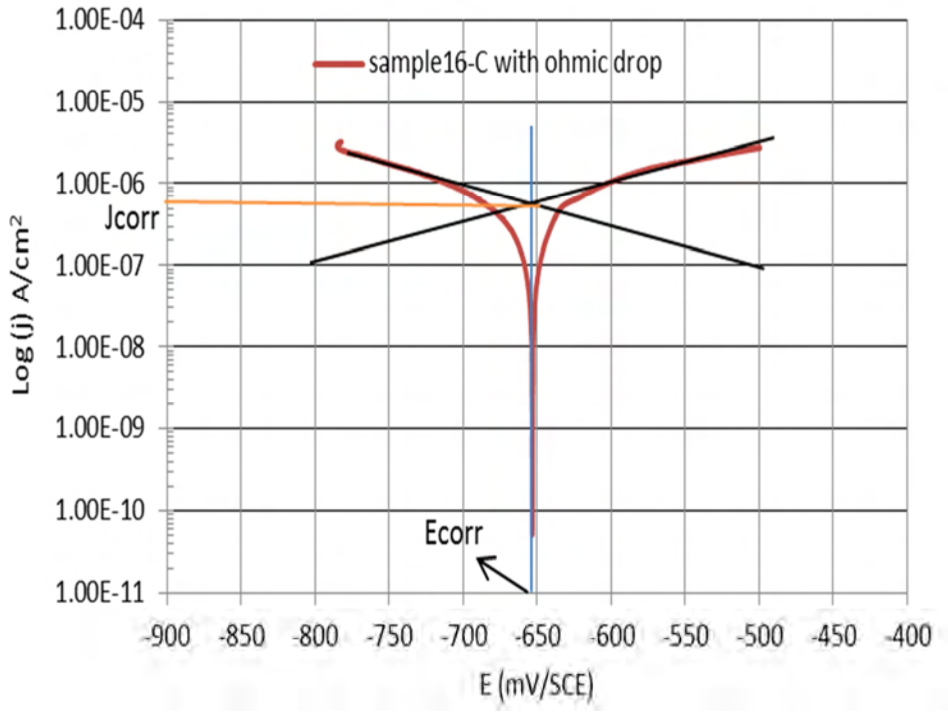

Figure 2-15 Polarization curve for a steel bar in carbonated sample

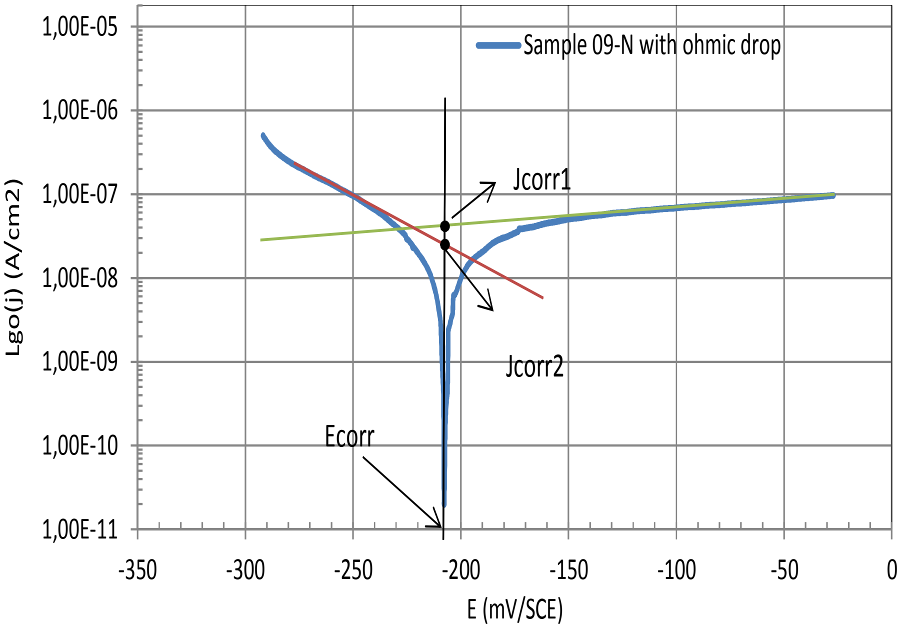

Figure 2-16 Polarization curve for a passive bar in non-carbonated concrete

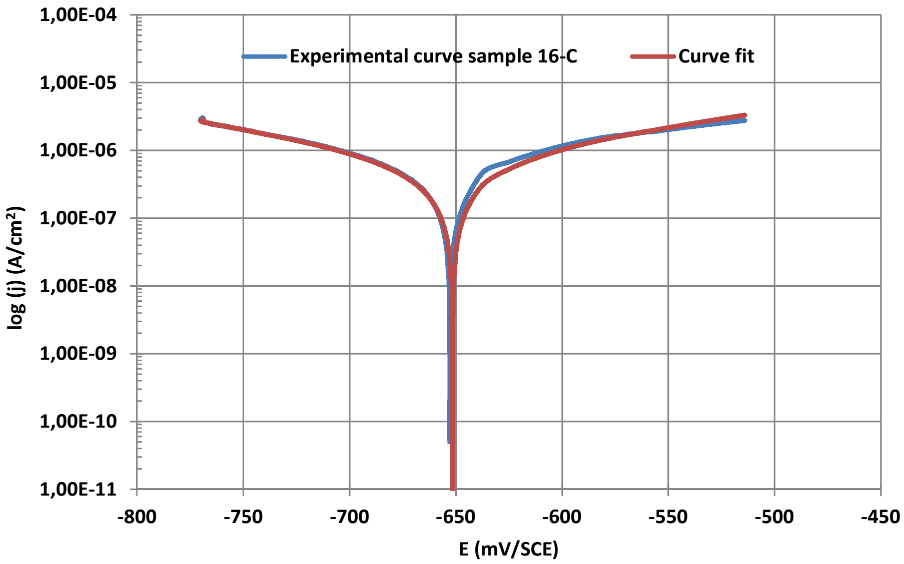

Figure 2-17 Curve fit for a steel bar in carbonated concrete

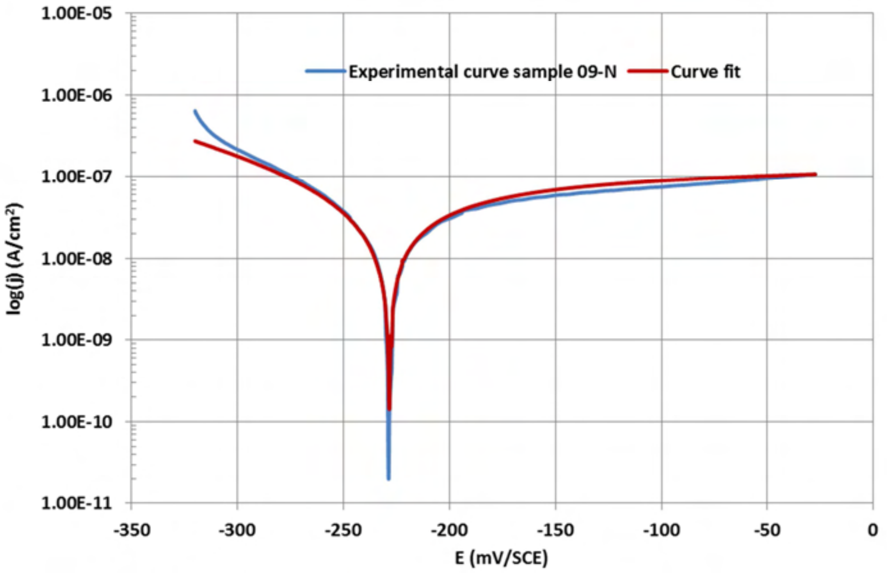

Figure 2-18 Curve fit for a steel bar in non-carbonated concrete

The curves obtained from partial polarization are shown in Figure 2-19 to Figure 2-22. The Figure 2-19 shows the partial anodic polarization of carbonated samples 03-C, 04-C and 05-C, these samples were not tested on cathodic polarization. Similarly samples 55-C, 56-C, 57-C were tested only for cathodic polarization (Figure 2-20). The noncarbonated samples tested on partial polarization are given at the bottom of Table 2-5. The extrapolation was performed same way as for complete polarization curves.

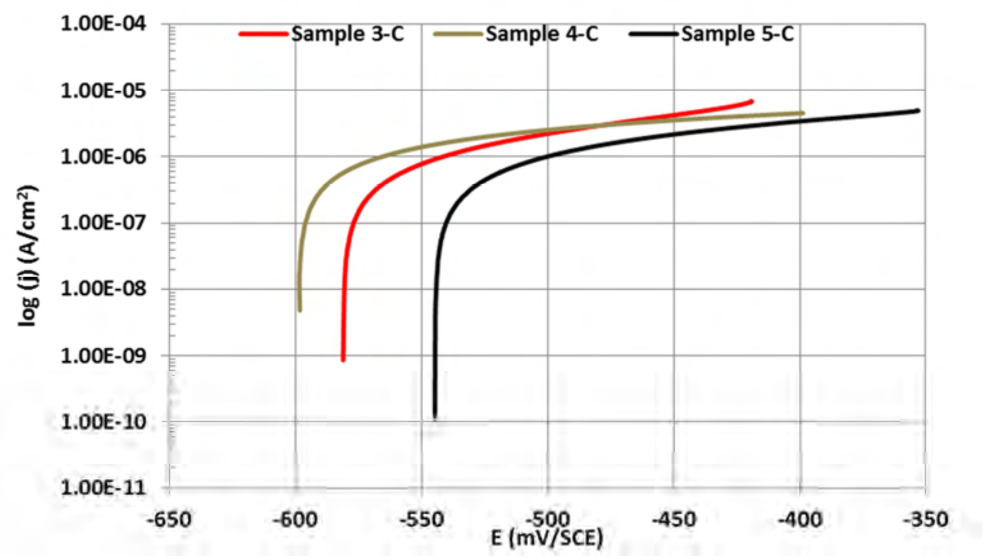

Figure 2-19 Anodic polarization for steel bars in carbonated samples

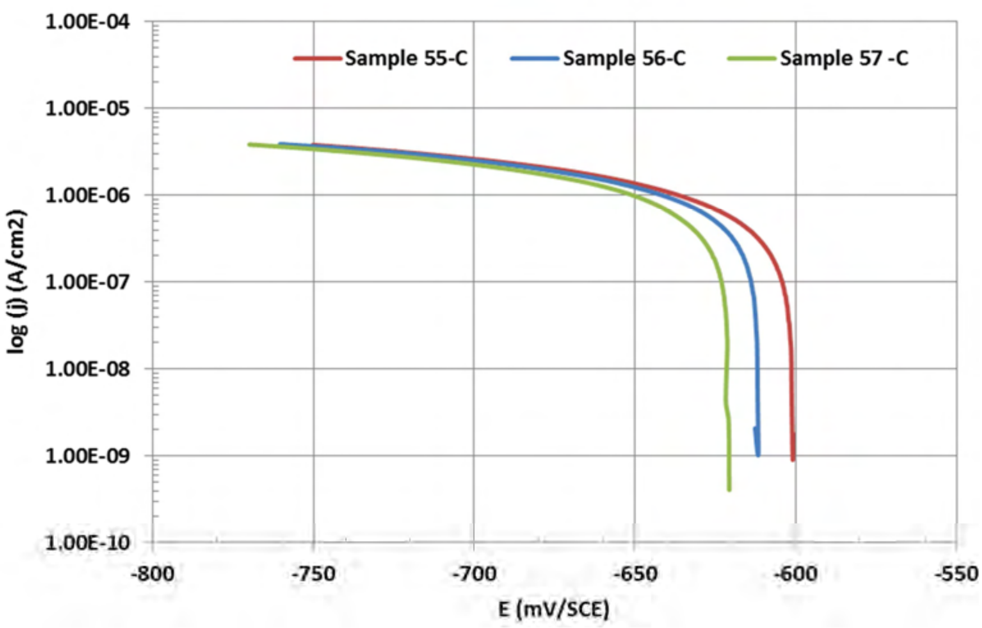

Figure 2-20 Cathodic polarization for steel bars in carbonated samples

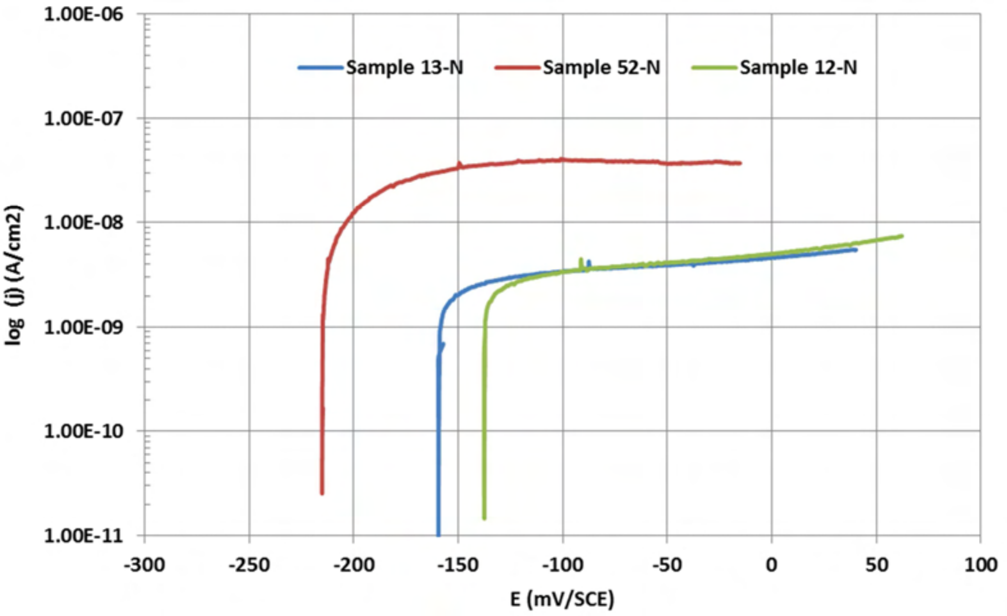

Figure 2-21 Anodic polarization of steel bar in non-carbonated samples

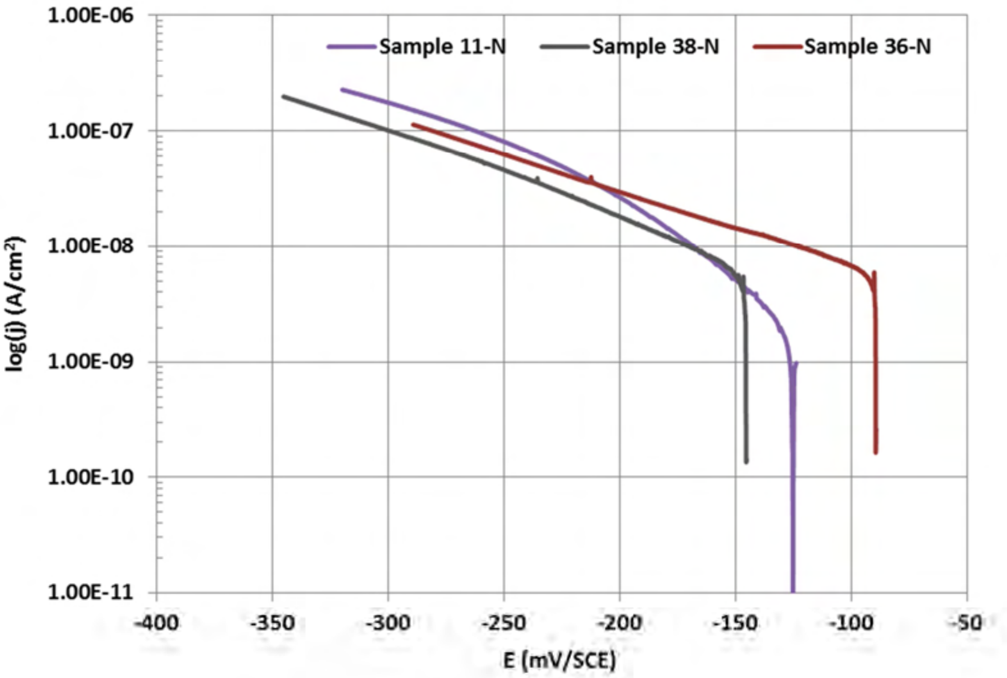

Figure 2-22 Cathodic polarization of steel bar in non-carbonated sample

2.4 Experimental Results

2.4.1 Corrosion Potential Distribution

The corrosion potential was measured for every sample before performing the Tafel experiments. The results are shown in the Table 2-4 and in Table 2-5. All the potential values in these tables are in mV against Saturated Calomel Electrode (SCE). The corrosion potentials were measured after stabilization of the values. Normally $30\ to\ 60$ minutes are required for potential values to stabilize after the connections are made. Figure 2-23 shows the potential measurements and time for stabilization. Figure 2-24 shows the distribution of corrosion potential of steel bars in carbonated concrete. The steel bars were depassivated and were in active state of corrosion, their potentials were observed to be in a range from -543 to $-650\ mV/SCE$. The average value of corrosion potential for active steel bars is $640\ mV/SCE$ and the standard deviation is $38\ mV/SCE$. The corrosion potential of these active steel bars are well in accordance to the available literature results on half-cell potential measurement, and to the ASTM C-879 standard which depicts the potential of a corroded bar more electronegative than $-350\ mV/CSE$.

The values of corrosion potential of passive steel bars in non-carbonated samples found to be in the range of$-89\ to - 319\ mV/SCE$, with an average of $-214\ mV/SCE$ and a standard deviation of $62\ mV/SCE$ (Figure 2-25). The large variability of passive bar potential has already been documented. Elsener et al., (2003) have mentioned that the potential of passive bar in sound concrete depends on oxygen availability and RH, and can vary over a wide range of values. These variations in corrosion potentials can also be the result of large passivity range of a steel bar in non-carbonated concrete. Figure 2-26 shows a range of passivity given by Bertolini et al., (2004), it also shows that the corrosion potential of passive bar in noncarbonated concrete can be found dispersed depending upon the concrete pore conditions, i.e. whether the oxygen is available or not, or if concrete is saturated or dry. The potential values found for these passive bars are more electronegative as observed in literature and in standards like ASTM C-876 and RILEM Recommendations, which depict that corrosion potential for passive steel is equal or higher than -200 mV/CSE. The more electronegative potential can be due to the higher degree of saturation of samples, as it was mentioned by Soleymani and Ismail, (2004), who have observed that when the concrete is saturated (RH is higher), the corrosion potential of steel bars drops to more electronegative values.

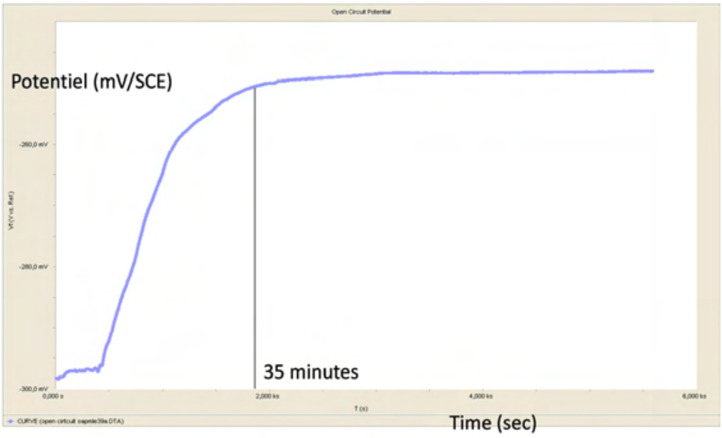

Figure 2-23 Corrosion potential monitoring before Tafel experiments

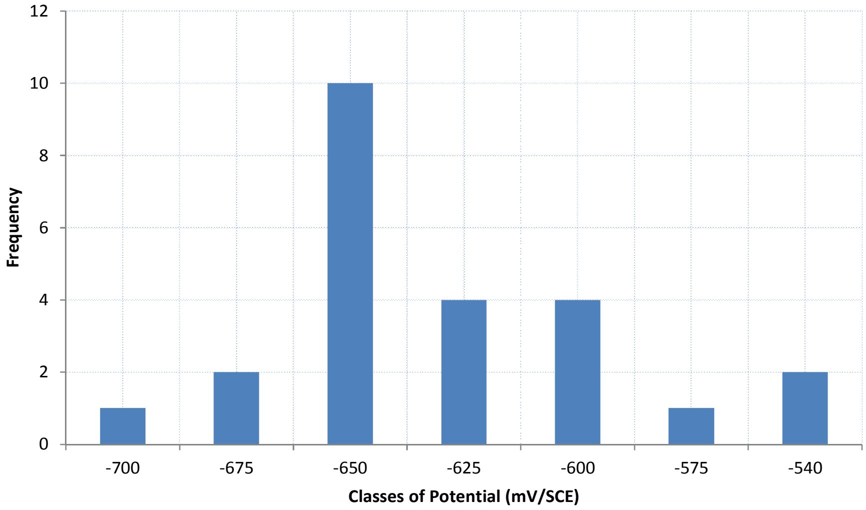

Figure 2-24 Corrosion potential distribution of steel bars in carbonated concrete samples

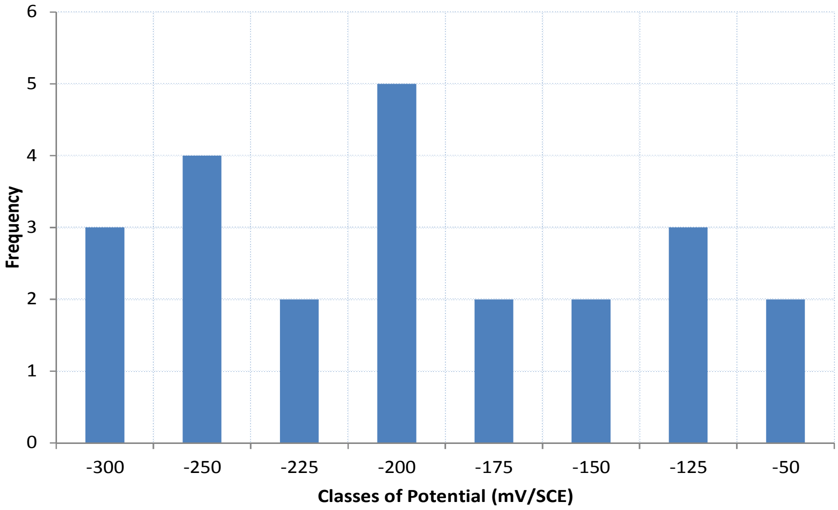

Figure 2-25 Corrosion potential distribution of steel bars in non-carbonated concrete samples

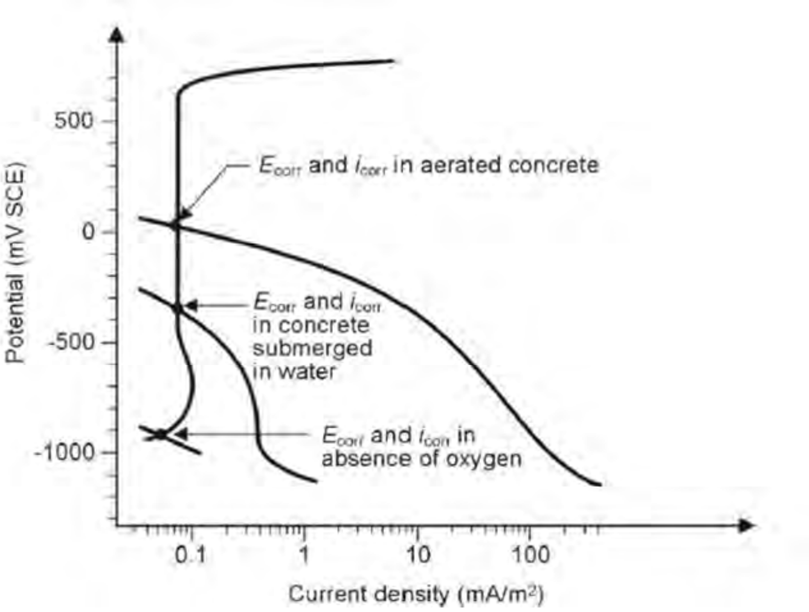

Figure 2-26 Schematic representation of the corrosion conditions of passive steel in concrete, under different conditions of moisture content (Bertolini et al., 2004).

2.4.2 Corrosion Current density

The corrosion current density of active steel bars in carbonated concrete samples was observed to be in the range of $0.3\ \mu A/cm^2$ to $2.60\ \mu A/cm^2$, with a median of $0.88\ \mu A/cm^2$ and an average of $0.86\ \mu A/cm^2$ (Figure 2-27). Corrosion current density obtained from carbonated samples (3-C, 4-C, 5-C, 55-C, 56-C and 57-C) which were tested on partial polarization had also the range of $0.5\ \mu A/cm^2$ to $0.9\ \mu A/cm^2$. Figure 2-28 shows the values of corrosion current density of passive steel bars in non-carbonated samples. The corrosion current density was found in the range of $0.01\ \mu A/cm^2$ to $0.15\ \mu A/cm^2$, with a median of $0.05\ \mu A/cm^2$ and an average of $0.058\ \mu A/cm^2$. The corrosion current density of sample tested on partial polarization (12-N, 13-N, 52-N, 17-N, 36-N and 38-N) was to be around 0.008 to $0.01\ \mu A/cm^2$. The values have a close resemblance with values found with cyclic polarization. The corrosion current density at active steel bar in carbonated concrete is about 10 times higher than that of passive steel bars in non-carbonated concrete. The values of corrosion current density in carbonated concrete are found to be less than those measured in chloride contaminated concrete, this is due to the higher concrete resistivity in the case of carbonated concrete (Miyazato, 2010). The corrosion current densities obtained from the sample tested on different scan rates were not significantly different, in fact there was no trend observed in case of carbonated sample. The average value for the sample tested at 0.1 mV/s was 0.95$\mu A/cm^2$, for a scan rate of 0.5 mV/s it was 0.92 $\mu A/cm^2$ and for 0.8 mV/s scan rate gave an average current of 0.83$\mu A/cm^2$.

While in noncarbonated concrete samples, the average values of corrosion current density obtained in case of a scan rate of 0.8 mV/s were higher than that for the other scan rates, i.e 0.070 $\mu A/cm^2$, while in case of 0.5 mV/s and in 0.1 mV/s the values were 0.055 $\mu A/cm^2$ and 0.035 $\mu A/cm^2$ respectively. The standard deviation in of these current values for the scan rates 0.1, 0.5 and 0.8 mV/s were 0.021, 0.052 and 0.022 respectively.

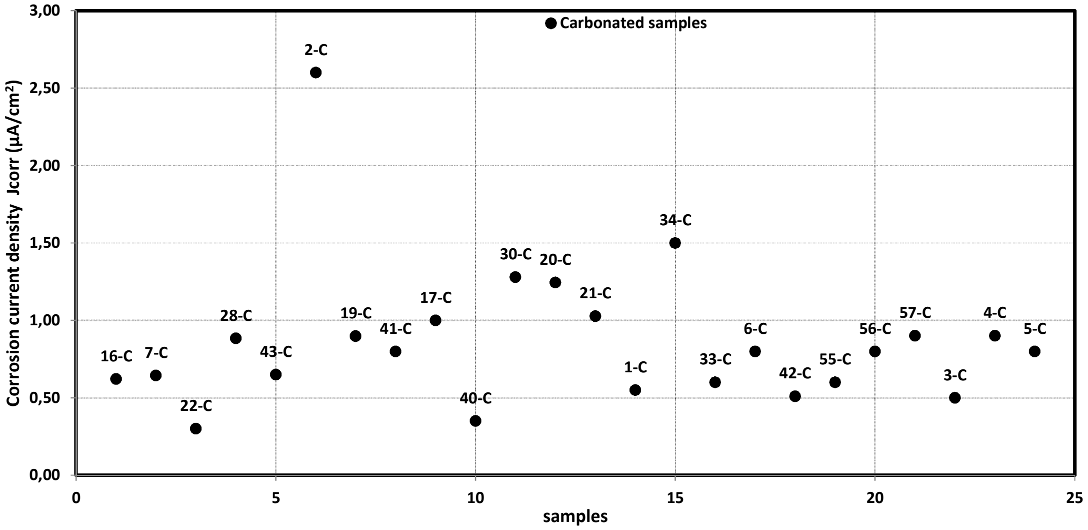

Figure 2-27 Corrosion current density at steel surface in carbonated samples

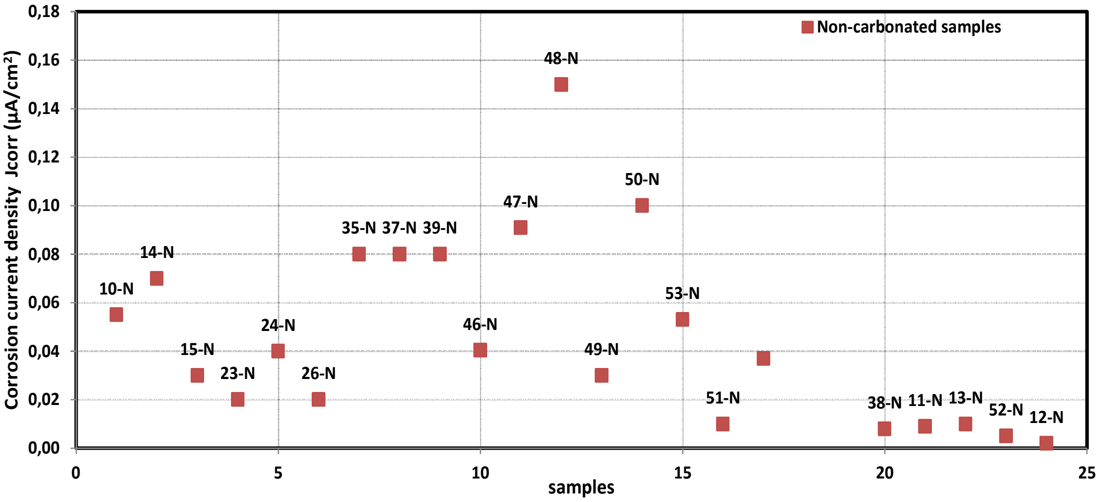

Figure 2-28 Corrosion current density at steel surface in Non-carbonated samples

Figure 2-29 and Figure 2-30 present the corrosion current density as a function of electrochemical corrosion potential for carbonated and non-carbonated samples respectively. The corrosion current density is normally increased with the decrease in electrochemical corrosion potential. Same tendency found with these Tafel experiments, the effect of the decrease in corrosion potential is more prominent in case of carbonated sample, as the slope of the trend line (Figure 2-29) is almost 10 times higher than that of the noncarbonated sample (Figure 2-30). The sample 5-C had a corrosion potential -543 mV/SCE and a corrosion current density of 0.6 $\mu A/cm^2$, while sample 34-C had a corrosion potential -661 mV/SCE, and it produced a corrosion current density of 1.5 $\mu A/cm^2$.

Some samples had much negative electrochemical potential but less corrosion current density, e.g 22-C which had a corrosion potential -702 mV/SCE but the corrosion current density was found to be 0.3 $\mu A/cm^2$ (Figure 2-29). This shows that the corrosion potential (half-cell) is not always a good indication of higher corrosion rate on steel surface because its value can be very negative due to the saturation of concrete with water and consequently lack of oxygen near steel concrete interface. (Feliú et al., 1996) has shown that generally there is a poor relationship between corrosion potential and corrosion current density measured by Linear Polarization Resistance (LRP).

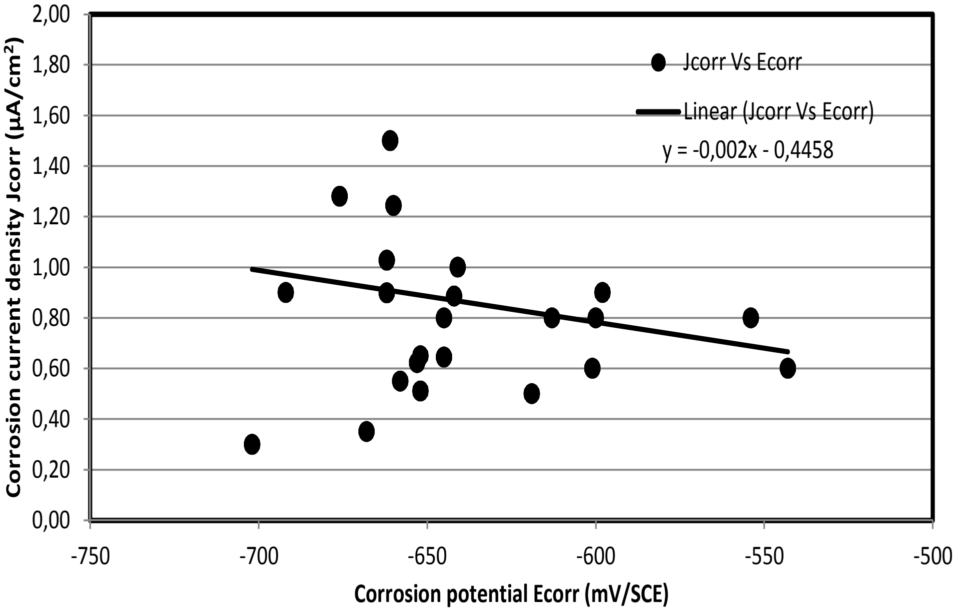

Figure 2-29 Corrosion current density Vs Corrosion potential in carbonated samples

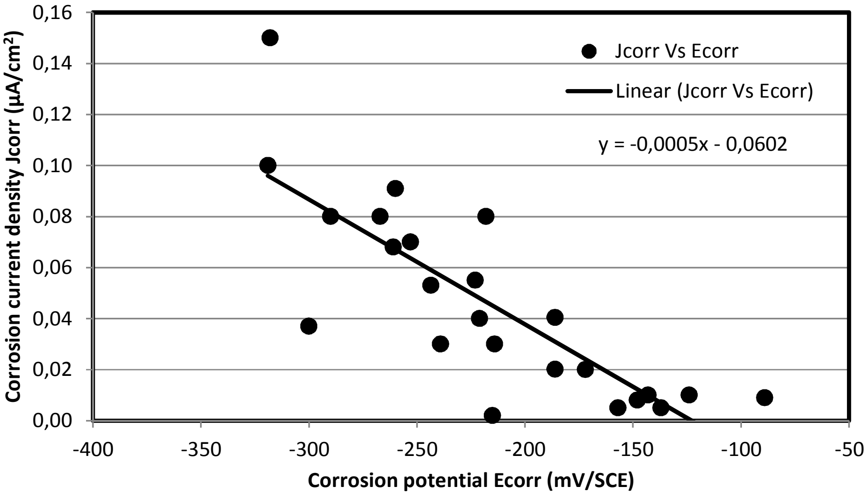

Figure 2-30 Corrosion current density Vs Corrosion potential in Non-carbonated samples

2.4.3 Anodic Tafel slope in carbonated and Non-carbonated sample

Literature is available on corrosion parameters like Tafel slope coefficients in case of corrosion induced by chloride ingress in concrete. However there is not a lot of work done to find out these corrosion parameters in carbonated concrete. The anodic Tafel slope coefficient β_a for steel bar in carbonated concrete was in the range of $180\ to\ 280\ mV/dec$ (Figure 2-31). The average value over 18 samples was $244\ mV/dec$. Poursaee, (2007) has performed cyclic polarizarion test on different types of cocnrete, he found the values of β_a around $247\ mV/dec$ in carbonated concrete. This is very close to the average values of anodic Tafel slope coefficient found in our work. While the values for the passive steel in non-carbonated concrete samples were in the range of $374\ to\ 700\ mV/dec$ with an average of $505\ mV/dec$. As the steel in non-carbonated concrete is in passive state, the rate of the anodic reaction is very slow, this gives a very flat slop of anodic part of the polarization curve, that is why values of anodic Tafel slope coefficients are very high. As the anodic curve of passive steel bar in carbonated concrete is very flat in slope, and the fact that the current is plotted on a logarithmic scale, so a small deviation in the straight line drawn at Tafel region could cause a huge difference of mV to cross a decade. That is why the β_a values for noncarbonated concrete sample are so dispersed. In literature, some researchers have used the values as infinity due to no effect of anodic Tafel slope on corrosion system after certain value ($550 - 700\ mV/dec$). The carbonated samples 3-C, 4-C and 5-C were tested under anodic polarization; the values of β_a were 160, 250 and $180 mV/dec$, respectively. These values are in accordance with the values found with cyclic polarization. The non-carbonated sample 13-N, 52-N and 12-N were also tested under anodic polarization of 200 mV from E_{corr}. The β_a values were 700, 1000 and 650 mV/dec, respectively.

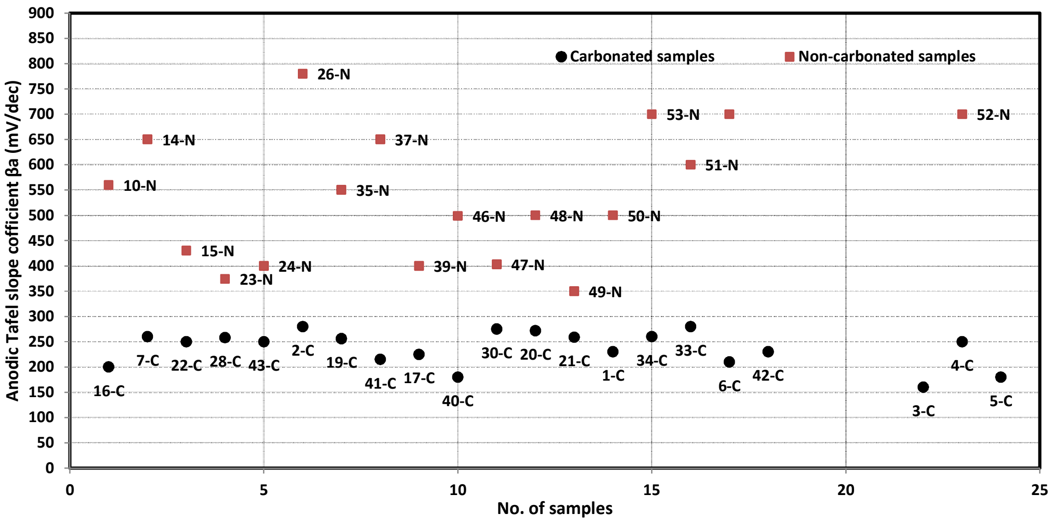

Figure 2-31 Anodic Tafel slope coefficient β_a for Active and Passive steel bars

2.4.4 Cathodic Tafel slope in carbonated and Non-carbonated samples

The cathodic Tafel slope coefficients obtained from the polarization curves of active steel bars in carbonated concrete are in a range of $190\ to\ 350\ mV/dec$, with an average value of $260\ mV/dec$ (Figure 2-32). Normally the values of β_c are higher than β_a in carbonated concrete, we have found the same tendency but the difference is not as large as given in previous works. The polarization curves in carbonated concrete were quasi symmetric and both slopes were identical. The β_c values of partial cathodic polarization on sample 55-C, 56-C and 57-C are 210, 190 and 220 mV/dec respectively.

In case of steel bar embedded in non-carbonated concrete the cathodic Tafel slope coefficient‘s values are less than those of its anodic Tafel slope coefficients. The range found is from $70\ to\ 160\ mV/dec$. These β_c values are also less than the value found for steel in carbonated concrete, which means the oxygen reduction reaction is faster at passive steel bar than on active steel bar. The values of β_c with partial polarization on sample 36-N, 38-N and 11-N were 140, 150 and $110 mV/dec$, respectively. These values also fall the same range as found with cyclic polarization.

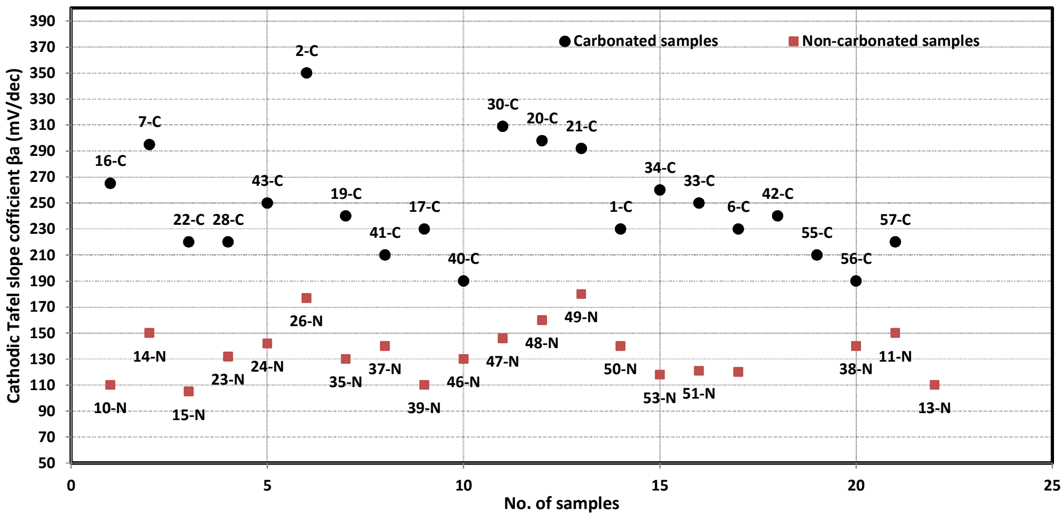

Figure 2-32 Cathodic Tafel slope coefficient β_c for Active and Passive steel bars

2.5 Conclusions

- The values of Tafel slope coefficients found in carbonated concrete are different from the available literature. This is because the literature available on corrosion parameters mostly deals with corrosion induced by chloride contamination, and the corrosion induced by carbonated environment has different kinetics than that of chloride contamination. The corrosion current density has also lower value even though the half-cell potential is found to be the same as in chloride contaminated environment; this is mainly due to the higher resistivity of carbonated concrete.
- The parameters obtained from partial polarization on carbonated and non-carbonated samples show same range as in cyclic polarization, except for the corrosion current density obtained in case of noncarbonated samples tested at partial anodic polarization. The corrosion current density in these samples was fractionally lower than others.
- The values of corrosion parameters obtained from these polarization curves were used to numerically simulate the corrosion phenomena in carbonated and in non-carbonated concrete. The numerical design of accelerated corrosion test is explained in third chapter.

CHAPTER # 3

3 Design of Acceleration Corrosion test

3.1 Introduction

This chapter explains the experimental and numerical design of the accelerated corrosion test proposed in this thesis. The long time periods involved in replicating reinforcement corrosion within laboratories has resulted in a number of accelerated test methods being developed. We first proposed to accelerate the corrosion in the initiation phase by carbonation, and to achieve the higher corrosion current density in propagation phase, we propose to increase the Cathode/Anode (C/A) ratio. To easily increase and decrease cathode/anode ratio in laboratory experiments, we decided to have a cylindrical concrete sample with different number of steel bars embedded in the concrete. The central cylindrical concrete was carbonated to have a depassivated steel bar. Then another concrete ring was casted around the inner cylinder, having four different steel bars embedded at a constant distance from center and also from each other.

As laboratory experiments are often time consuming and laborious, that is why at first the accelerated corrosion test was designed by means of numerical simulations. The simulations were performed by using the commercially available software COMSOL Multiphysics which is based on FEM. A same geometry with one interior concrete cylinder and one exterior cylinder was used to simulate corrosion. It was supposed that interior cylinder was carbonated and steel embedded in it was in active state, while steel bars in sound concrete were in passive state.

3.2 Details of the test

3.2.1 Geometry of Sample

The specimens proposed for accelerated corrosion tests are composed of two coaxial cylindrical concrete samples with embedded steel bars: one inner cylinder of carbonated concrete with one depassivated steel bar, and one outer cylinder of sound (non-carbonated) concrete enclosing 4 passive bars and surrounding the inner one. The moulds used to cast samples for accelerated corrosion test are shown in Figure 3-1, these moulds have 19.2 cm inner diameter and 15 cm height. A 2 cm thick movable base plate is placed in the bottom of moulds with 5 holes of 2 cm diameter throughout the thickness of the plate. One of the holes is at center to mount carbonated sample, while other four holes are around the central hole at 6.5 cm center-to-center distance, which allow fixing the 4 other steel bars at controlled distances.

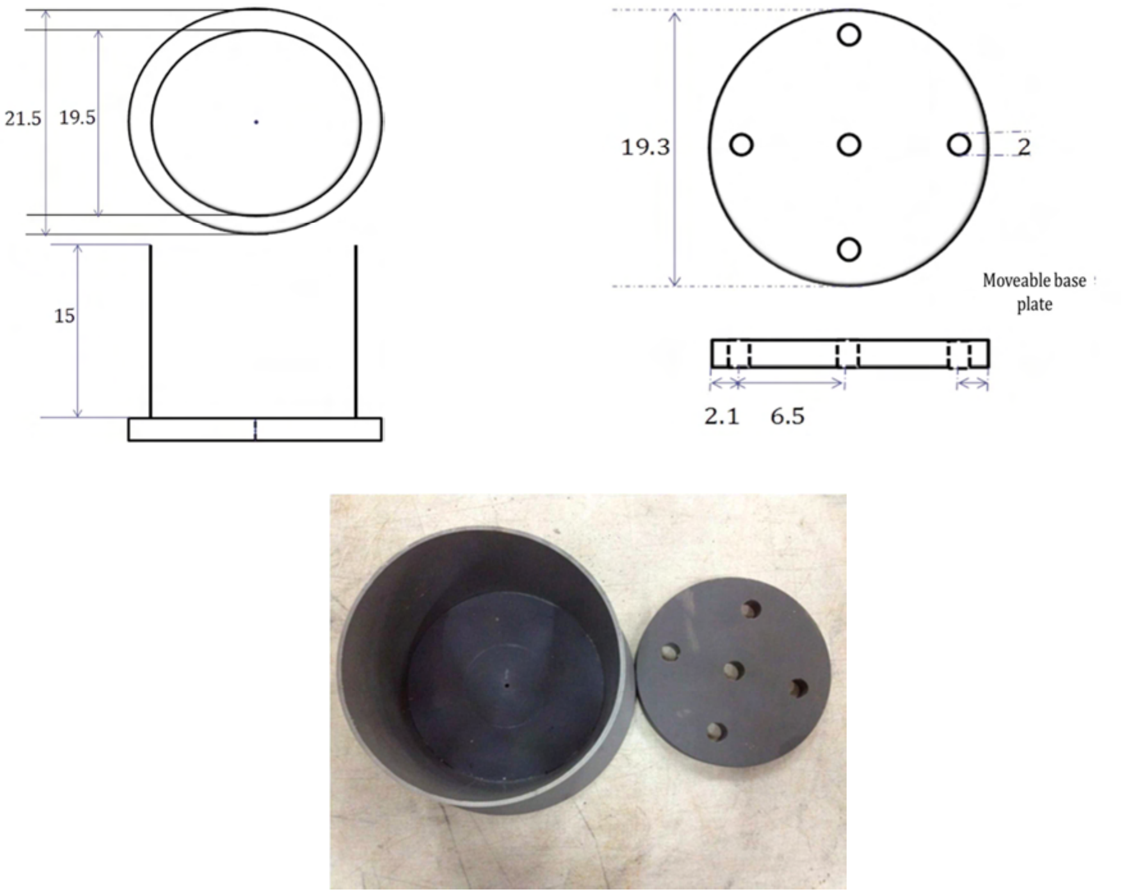

Figure 3-1 The preparation of specimen for accelerated corrosion tests, used mould with all the dimensions. (Dimensions are in cm).

3.2.2 Sample preparation and conditioning

Inner concrete cylinders enclosing one axial steel bar were casted first. They were casted using same procedure as for the cylinders used in Tafel slope experiments in chapter 2. The formulation of concrete was also kept same as given in Table 2-2, the mild steel bars having dimensions as previously used i.e 20 cm diameter and 14 cm length were used for these cylinders. After casting, the samples were kept in curing chamber (20°C, 95% RH) for 28 days; these samples were then stored in a controlled room (20°C and 65% RH) for two weeks before placing them into carbonation chamber. The carbonation chamber was set to 65% RH, 50% CO_2 and the temperature was set at 20°C. Five reference samples were casted to monitor the progress of carbonation in concrete. These reference samples were broken after 5th, 7th and 8th week of preservation in carbonation chamber, respectively. The samples were completely carbonated after 8 weeks, and with reference samples it was clearly seen that the steel bars were uniformly depassivated.

After the carbonation, the outer surface of cylindrical samples was made rough by steel brush, so that they can have a strong bond with the fresh concrete to be casted around them. These samples were again placed in curing chamber (20°C, 95% RH) for two weeks to saturate the concrete, so that the inner cylinder should not absorb the water from fresh concrete, and should not disturb its hydration process.

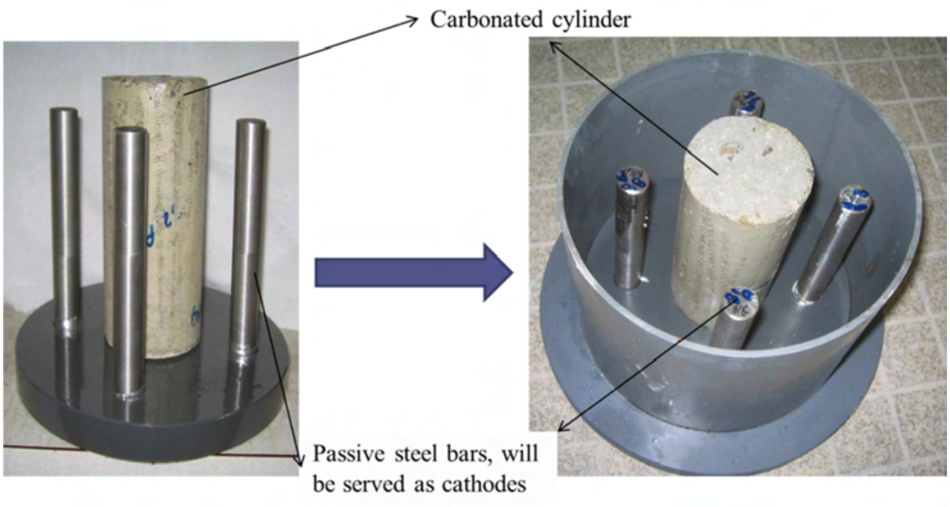

Figure 3-2 Fixation of carbonated inner cylinder and passive steel bars into the base plate and then in the mould.

Then carbonated samples were fixed into the central hole of moving plate, and four steel bars were also mounted all around the carbonated sample in respective holes, as shown in the Figure 3-2. Then, fresh concrete with same composition as used to cast inner cylinders was poured into the moulds. The samples were stored into a curing chamber for 28 days to optimize hydration of the newly poured concrete. At last, specimens were used to perform accelerated tests of galvanic corrosion by connecting the active central steel bar with one or several passive bars (Figure 3-3). The dimensions of galvanic corrosion specimens are summarized in the Figure 3-4 (cross-sectional view).

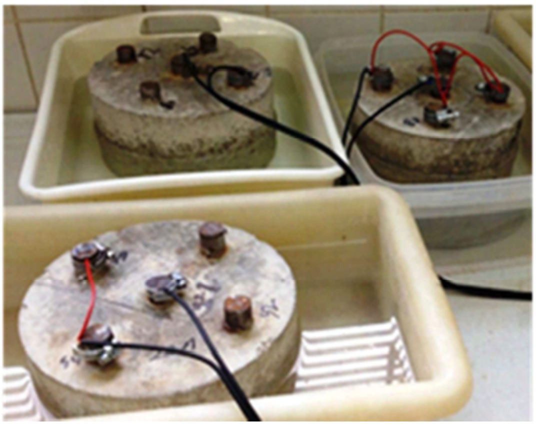

Figure 3-3 Accelerated corrosion test sample

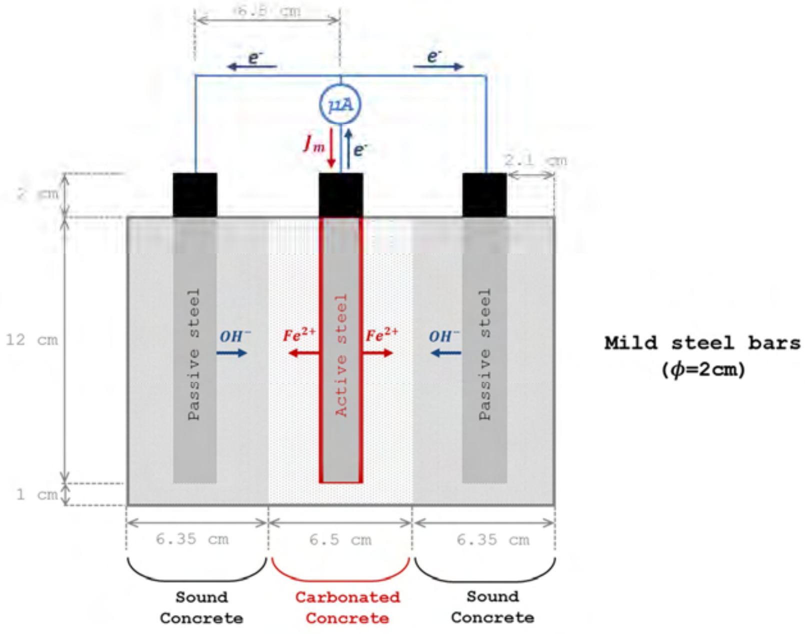

Figure 3-4 Cross-sectional view, dimensions of galvanic corrosion specimens and experiment principle

The reason for choosing this type of geometry is that it makes it easy to change the cathode surface in laboratory experiments by simply changing the number of passive bars connected with the active one. Moreover, cathodes located parallel and orthoradial around the central anode are expected to provide more macrocell current than cathodes placed co-planar with anode (Warkus et al., 2006).

3.3 Corrosion measurements

Corrosion experiments consists in electrical coupling of an active steel bar embedded in carbonated concrete with one or several surrounding passive bars embedded in sound concrete (Figure 3-4). This coupling allows electrons to be naturally exchanged between active and passive bars, resulting in the mutual polarization mentioned in the previous section: anodic polarization of the active bar (iron dissolution) and cathodic polarization of passive bars (formation of hydroxyl ions OH^-). This exchange of electrical charges is associated with the macrocell corrosion current J_m flowing from the active bar to the passive ones. The global electrochemical circuit involves both electronic current in the metallic wires used for bar coupling and ionic current in concrete. Therefore, the macrocell corrosion current is given by the measurement of the electronic current flowing within the coupling wires, as presented in the Figure 3-4.

For each specimen tested, a 1 Ω accurate resistance was connected in the circuit between anode (active bar) and cathodes (passive bars). Then, Yokogawa MW100® data acquisition device (Figure 3-5) is used to measure the voltage drop on the resistance and convert it into macrocell corrosion current. The low value of measurement resistance (1 Ω) is negligible with respect to ohmic resistance due to concrete and, consequently, it does not influence the galvanic system equilibrium. Thanks to 32 measurement channels, Yokogawa MW100® allows for monitoring galvanic current on several samples simultaneously. For each experiment, the macrocell current was considered after stabilization, in stationary condition. To monitor current stabilization, the sampling period was set at 1 minute. Before connecting the samples with Yokogawa MW100® acquisition, the galvanic current was first measured with the *galvanic current* module of Gamry®. These calculations were performed for comparison purposes.

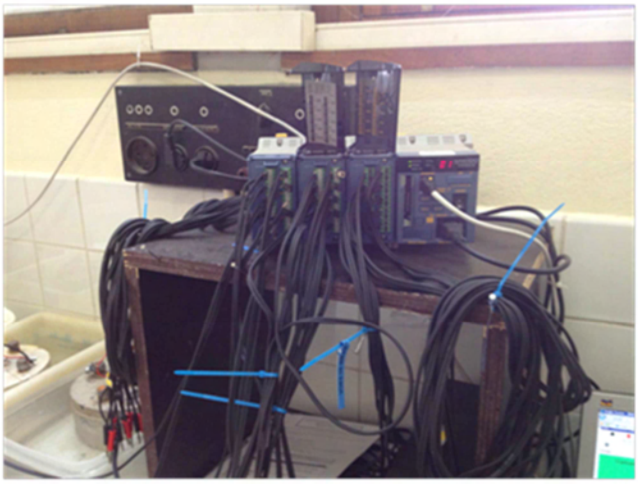

Figure 3-5 Yokogawa MW100® acquisition machine

3.4 Microcell and Macrocell Corrosion Systems

3.4.1 Microcell/Uniform corrosion system

This section describes the basic theoretical concepts relative to microcell (uniform) corrosion and macrocell (galvanic/localized) corrosion. As we know different environmental conditions result in different electrochemical equilibrium potentials at steel surface in concrete, e.g. when concrete is partially carbonated, some parts of steel have more negative electrochemical potentials, while in sound concrete steel is passive and has higher electrochemical potentials (Nasser et al., 2010; Warkus and Raupach, 2006). The steel in carbonated concrete would be in active state as the passive oxide layer would be destroyed by carbonation, and can be called as active steel or anode.

If the concrete environment of the steel reinforcement network is uniform, the electrochemical state of the bars and consequently the corrosion state (active or passive) are also uniform, meaning that anodic and cathodic reactions are not separated on steel surface. Each electron produced by anodic reaction is locally consumed by cathodic reaction and there is no current in the concrete volume. The potential field is also uniform.

The active and passive steel bars considered as independent electrochemical systems. In this case, the steel surface is assumed to be subjected to uniform electrochemical condition, resulting in uniform corrosion state (active or passive). As it is considered that anodic and cathodic reactions occur at the same location on the steel surface, therefore ohmic drop due to electrolytic resistivity is negligible. The polarization behavior of such uniform systems is usually modeled by the Butler-Volmer equation (derivation of equation is discussed in section 1.2.1, either for active Eq. 3.1 or passive steel Eq. 3.1.

$$j_a = j_{corr,a}\left(exp\left(ln(10)\,\frac{E_a - E_{corr,a}}{\beta_{a,a}}\right) - exp\left(-ln(10)\,\frac{E_a - E_{corr,a}}{\beta_{c,a}}\right)\right) \qquad \textit{Eq. 3.1}$$

$$j_p = j_{corr,p}\left(exp\left(ln(10)\,\frac{E_p - E_{corr,p}}{\beta_{a,p}}\right) - exp\left(-ln(10)\,\frac{E_p - E_{corr,p}}{\beta_{c,p}}\right)\right) \qquad \textit{Eq. 3.2}$$

Where:

- j_a and j_p are the net current densities flowing through the metal-electrolyte interface of the active and passive uniform systems forced at potential E_a and E_p, respectively (involving a polarization with respect to the equilibrium potentials $E_{corr,a}$ and $E_{corr,p}$);
- $j_{corr,a}$ and $j_{corr,p}$ are corrosion current densities (exchange current densities) for active and passive uniform corrosion systems, respectively ($j_{corr,a} \gg j_{corr,p}$);
- $E_{corr,a}$ and $E_{corr,p}$ are free corrosion potentials at equilibrium of active and passive uniform corrosion systems, respectively ($E_{corr,a} < E_{corr,p}$);
- $\beta_{a,a}$ and $\beta_{a,p}$ are anodic anodic Tafel coefficients of active and passive uniform corrosion systems, respectively ($\beta_{a,a} < \beta_{a,p}$);
- $\beta_{c,a}$ and $\beta_{c,p}$ are cathodic anodic Tafel coefficients of active and passive uniform corrosion systems, respectively ($\beta_{c,a} \approx \beta_{c,p}$).

The Butler-Volmer equation of a uniform corrosion system corresponds to the algebraic sum of the current density associated with anodic reaction (Eq.1.34) and the current density associated with cathodic reaction (Eq.1.35) (Warkus J R. M., 2006; Kim C.Y, 2008). The Figure 3-6 shows the qualitative polarization behavior of such active and passive corrosion systems, acting as independent electrochemical systems. For each system, the equilibrium corrosion potential ($E_{corr,a}$ or $E_{corr,p}$) corresponds to the value at which anodic current ($j_{corr,i}$) compensates cathodic current ($-j_{corr,i}$). Since anodic and cathodic reactions do not involve the same chemical species, it is actually referred to as dynamic equilibrium, in which steel is continuously dissolved and oxygen is reduced. At this dynamic equilibrium, corrosion of steel occurs, but no net current flows through the metal-electrolyte interface of the electrochemical system ($j_a = 0$ or $j_p = 0$), due to the compensation of anodic and cathodic current densities.

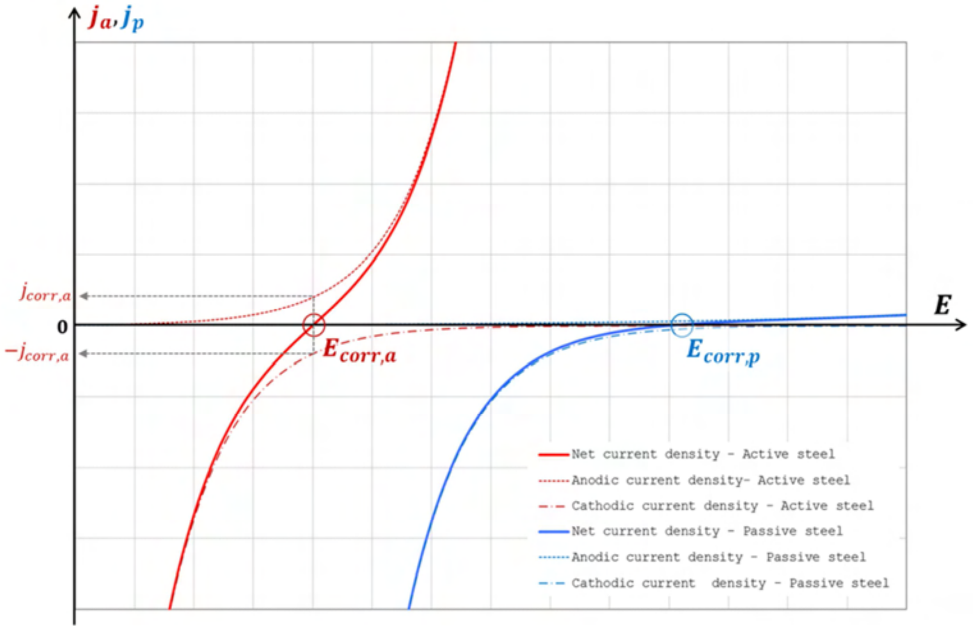

Figure 3-6 Qualitative electrochemical behavior of active and passive systems (no electrical connection)

A perturbation of such a system from the equilibrium corrosion potential is referred to as polarization and results in a net current density flowing through the metal-electrolyte interface, since one reaction is enhanced. An anodic polarization ($\Delta E = E_i - E_{corr,i} > 0$) enhances the anodic reaction in the electrochemical system (steel dissolution), resulting in a positive net current density flowing through the electrochemical interface ($j_i > 0$). On the contrary, a cathodic polarization ($\Delta E = E_i - E_{corr,i} < 0$) enhances the cathodic reaction in the electrochemical system (oxygen reduction), resulting in a negative net current density flowing through the electrochemical interface ($j_i < 0$). The relations $j_a(E_a)$ and $j_p(E_p)$ define the polarization curves of active and passive uniform corrosion systems, respectively (Figure 3-6).

3.4.2 Macrocell/Galvanic corrosion system

In case of non-uniform environment, such as partial carbonation of concrete leading to a local depassivation of steel, electrochemical state of the steel bar network may vary from one point to another. Since all steel bars in the reinforcing network are electrically connected, electrons produced by local anodic reaction may be consumed by cathodic reaction occurring somewhere else on the network (Figure 3-7) (Warkus and Raupach, 2006). This phenomenon is referred to as galvanic corrosion (also macrocell or localized corrosion) and is characterized by a gradient of the potential field and an ionic current flowing in the concrete volume from anodic areas towards cathodic areas (equal to electronic current exchanged through the metallic network).

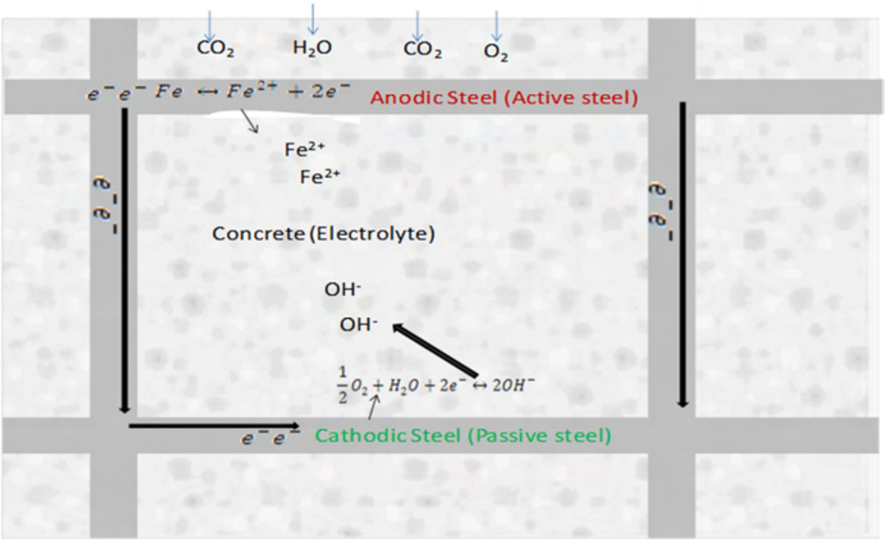

Figure 3-7 Macrocell current due to the connection of steel bars in concrete

A macrocell corrosion system may then be defined as the electrical coupling of two different uniform corrosion systems, making it possible for the two systems to exchange electrons thanks to a metallic connection (Clément et al., 2012; Nasser et al., 2010; Warkus and Raupach, 2006). Connecting an active uniform corrosion system with a passive one results in their mutual polarization, both active and passive potential being attracted by the other (Figure 3-8). Therefore, in a galvanic corrosion system, due to electrical connection, passive steel areas undergo cathodic polarization (passive steel potential is attracted towards active potential value, i.e. $E_p - E_{corr,p} < 0$) while active steel areas are subjected to anodic polarization (active steel potential is attracted towards passive potential value, i.e. $E_a - E_{corr,a} > 0$). Active and passive areas being spatially separated in case of galvanic corrosion,

E_a and E_p do not end up at same value, due to ohmic resistivity of the electrolyte (concrete) and passive potential E_p remains higher than active potential E_a.

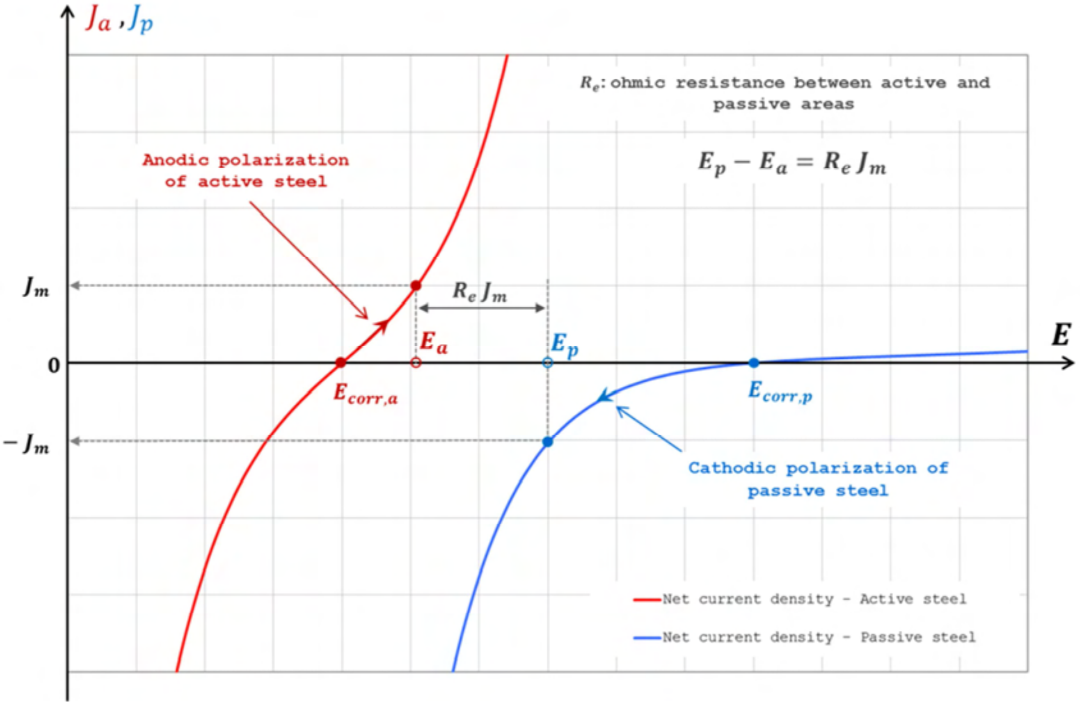

Figure 3-8 Qualitative description of the equilibrium of a 1D galvanic corrosion system (electrical coupling between active and passive steel bars)

In case of galvanic corrosion, active and passive surfaces may be different and it is therefore necessary to deal with current intensity values (J_a, J_p) to discuss about the equilibrium of a galvanic system. Due to the respective polarizations, net currents flow through both active and passive electrochemical interfaces ($J_a > 0$ and $J_p < 0$, respectively). At equilibrium of the galvanic system, the anodic current J_a produced by the active steel compensates the cathodic current J_p produced by the passive steel, so at the equilibrium anodic and cathodic currents define the macrocell (or galvanic) current J_m (Eq.3.3).

$$J_a = -J_p = J_m \qquad \textit{Eq. 3.3}$$

Macrocell current flows through the electrolyte from anodic areas (active steel) towards cathodic areas (passive steel) and ohmic effects due to electrolyte resistance influence the equilibrium state of the galvanic system. Therefore, to determine the galvanic system equilibrium, Eq. 3.3 has to be completed by Eq.3.4, which links the ohmic drop between passive and active potential values to macrocell current J_m and electrolytic resistance R_e.

$$E_p - E_a = R_e \, J_m \qquad \text{Eq. 3.4}$$

3.5 Numerical Model details

3.5.1 Geometrical model

Figure 3-9 shows the meshed geometry of simulated specimen corresponding to shape and dimensions of experimental samples. The geometrical model is composed of two coaxial cylinders. The inner cylinder simulates carbonated concrete and has active steel bar at the centre. The outer cylinder surrounds the inner one and simulates sound (non-carbonated concrete). According to the experimental test to be simulated, the outer cylinder may have one or several steel bars embedded in vertical direction. All steel bars have $20\,mm$ diameter and $120\,mm$ length. Distance between active and passive steel bars is $65\,mm$ from center to center. Both concrete cylinders have different values of resistivity, as carbonated concrete offers more resistance to current (Nasser et al., 2010; Warkus and Raupach, 2008). With numerical simulations we have observed the C/A ratio effects till 8/1 while in laboratory experiments we used only four cathode bars (i.e. 4/1 for C/A ratio).

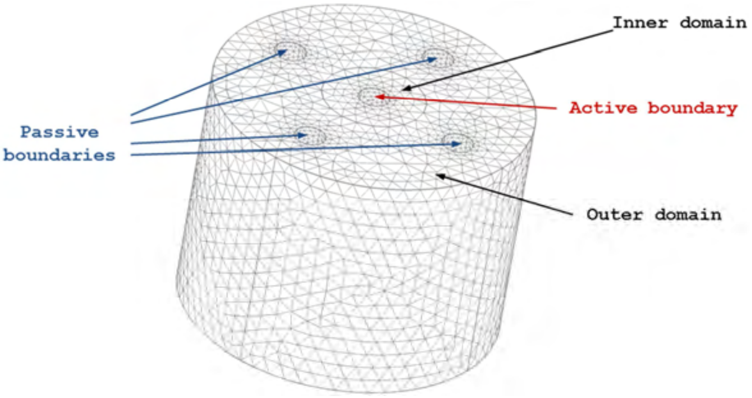

Figure 3-9 Geometrical model and meshing

3.5.2 Electrokinetics equations

In the concrete volume, the equations governing electrical phenomena are local Ohm's law (Eq.3.5) and charge conservation (Eq.3.6).

$$\boldsymbol{j} = -\frac{1}{\rho}\,\nabla E \qquad \text{Eq. 3.5}$$

$$\nabla.\boldsymbol{j} = 0 \qquad \text{Eq. 3.6}$$

Where $\boldsymbol{j}$ is the local current density, ρ is the electrical resistivity of concrete and E is the local value of the potential field (Clément et al., 2012; Nasser et al., 2010).

3.5.3 Boundary Conditions

The steel-concrete boundaries were modeled according to Butler-Volmer equation for both active and passive bars (Eq.3.1 and Eq.3.2, respectively) with specific parameter values. All other interfaces are modeled as electrical insulation, except for the internal boundary between inner and outer domains where a continuity condition is applied. The potential and the current density fields in concrete volume are computed by solving Eq.3.5 and Eq.3.6, subjected to the different prescribed boundary conditions (Ge and Isgor, 2007; Isgor and Razaqpur, 2006).

3.5.4 Simulation parameters

The corrosion parameters show considerable variations in literature for active and passive conditions as already discussed in Chapter 2. Bearing in mind the uncertainty, Tafel experiments were performed on carbonated and non-carbonated concrete samples with embedded steel bars to obtain polarization curves. Concrete samples were saturated and experiments were performed at room temperature (20°C). Majority of these parameters matched well with those given in the literature, e.g corrosion potential, corrosion current density of active and passive steel bar, anodic and cathodic Tafel slope coefficients of passive steel bar, cathodic Tafel slop coefficient of active steel bar. Only the anodic Tafel slope coefficients value of active steel was found to quite high than those given in literature. The simulations were first performed by using the corrosion parameters given in Table 3-1, and then a detailed parametric study was performed to observe their effects on macrocell corrosion system. The geometry of sample was such that the use of Wenner probe to measure the resistivity was not possible. With Gamry® Get Ru module, the values obtained were much dispersed. For these simulations, the resistivity of carbonated and non-carbonated concrete was selected from usual range available in literature (Gjorv et al., 1977; Nasser et al., 2010; Polder et al., 2000).

The numerical solution was achieved by the finite element method (FEM), the simulations were performed thanks to the AC/DC module of the commercial FEM software Comsol Multiphysics®. AC/DC module allows simulating concrete as continuous resistive medium with Ohm's law and law of conservation of charge.

Table 3-1 – Corrosion parameters used for simulations	**Passive Steel (Cathode) Non-carbonated Concrete**	**Active Steel (Anode) Carbonated Concrete**
Concrete resistivity ρ $(ohm.m)$	300	600
Corrosion rate j_{corr} $(\mu A/cm^2)$	0.025	0.5
Corrosion potential E_{corr} (mV/SCE)	-150	-650
Anodic Tafel slope b_a (mV/dec)	400	90
Cathodic Tafel slope b_c (mV/dec)	150	150

3.6 Numerical results

3.6.1 Face to face polarization

To introduce the results of numerical experiments, attention is paid first to the face-to-face polarization effect illustrated in the Figure 3-10 in case of one passive bar connected. This effect results from the tridimensional nature of the physical problem and the non-negligible resistivity of concrete. Actually, it occurs quite systematically since one-dimensional conditions of current flows are rarely encountered regarding problems of steel corrosion in concrete. According to the potential ranges presented in Figure 3-10 for both active and passive steel bars, it may be observed that the side of active bar facing the passive one ($E_a = -599\, mV/SCE$) is naturally more polarized than the opposite side ($E_a = -615\, mV/SCE$). According to the free corrosion potential involved in simulation parameters for active steel ($E_{corr,a} = -650\, mV/SCE$), it means that the side facing passive steel undergoes an anodic polarization of about $+51\,mV$ versus $+35\,mV$ for the opposite side. Taking account of the polarization curve of active steel, a difference of $16\,mV$ in steel polarization may result in significant differences in local current density at steel-concrete interface. For example, regarding this simulation, the macrocell current produced by the half active bar facing the cathode bar is $58.4\,\mu A$, while opposite half-bar produces $45.4\,\mu A$ (22 % less than the side facing the passive bar). Therefore, the side facing the passive bar may have a significantly higher corrosion rate than the opposite side. This effect may be referred to as face-to-face polarization phenomenon.

As presented in the Figure 3-10, this effect is also occurring on the passive bar, since the side facing the active one is much more polarized ($E_p = -414\,mV/SCE$) than the opposite side ($E_p = -388\,mV/SCE$), meaning that the rate of cathodic reaction is higher on the first one. According to the free corrosion potential involved in simulation parameters for passive steel ($E_{corr,p} = -150\,mV/SCE$), it is observed that the polarization amplitude (absolute values) of passive steel is much higher than that of active steel (about 5 times higher). It is well in accordance with the shapes of polarization curves illustrated in Figure 3-7, which shows that to produce equal amounts of current to achieve equilibrium, passive bar has to be much more polarized than active bar. Nasser et al. (2010) already has reported same kind of polarization behavior. Warkus and Raupach, (2008) have also observed that passive steel polarized more than active both in laboratory experiments and in numerical simulations.

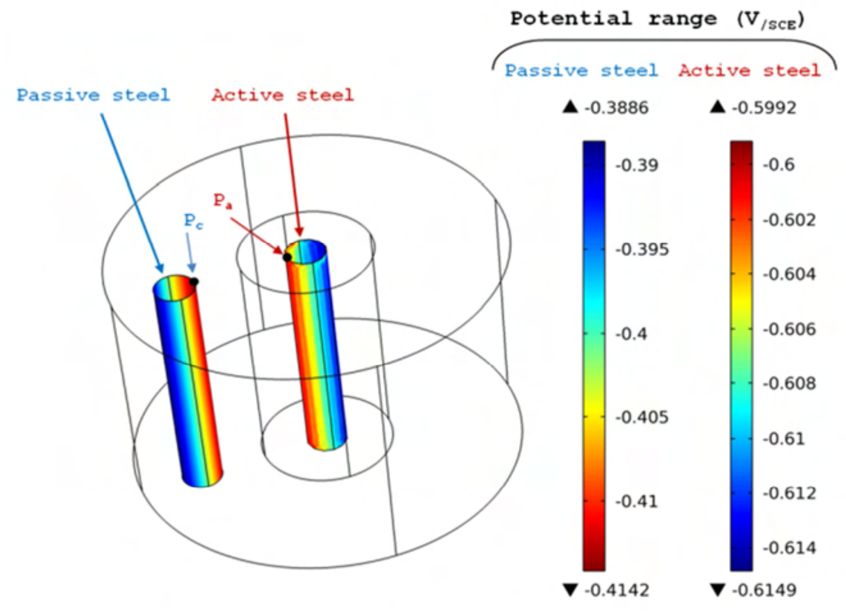

Figure 3-10 Face-to-face polarization effect (only one passive bar connected)

3.6.2 Potential distribution

The Figure 3-11 shows the potential gradients achieved in the concrete volume with different numbers of passive bars connected to the active one. As expected, regarding galvanic equilibrium condition, for each simulation case, active steel undergoes anodic polarization (with respect to $E_{corr,a} = -650\ mV/SCE$) while passive steel bars are subjected to cathodic polarization (with respect to $E_{corr,p} = -150\ mV/SCE$).

As expected according to galvanic corrosion theory, it is observed that increasing the number of connected passive bars results in higher anodic polarization of active steel, which is accompanied by an increase in anodic reaction rate. This galvanic coupling effect is well known and the numerical simulation allows here for taking into account of system geometry in equilibrium determination. When only one passive bar is available, active steel undergoes $+51\ mV$ maximum polarization, from -650 to $-599\ mV$ (values collected at point $\mathbf{P_a}$ defined in Figure 3-10, for which the polarization is maximum due to face-to-face effect), while with four passive bars connected, it undergoes $+62\ mV$ uniform polarization. On the contrary, increasing the number of passive bars results in a decrease of the global polarization range of passive steel, because larger area is available to produce the cathodic current necessary to achieve equilibrium.

Regarding the geometry of the specimens studied here, since passive bars are located in the circumferential direction and at equal distances from the active bar, the simulation case involving 4 passive bars connected produces a radial potential field (Figure 3-11-d). In this case, the active steel bar is quite uniformly polarized, while passive bars still undergo face-to-face polarization effect. The surface potential field on the outer circumferential boundary is quite uniform in this case. Regarding other simulation cases (1, 2 and 3 connected passive bars), surface potential fields on circumferential outer boundaries are non-uniform.

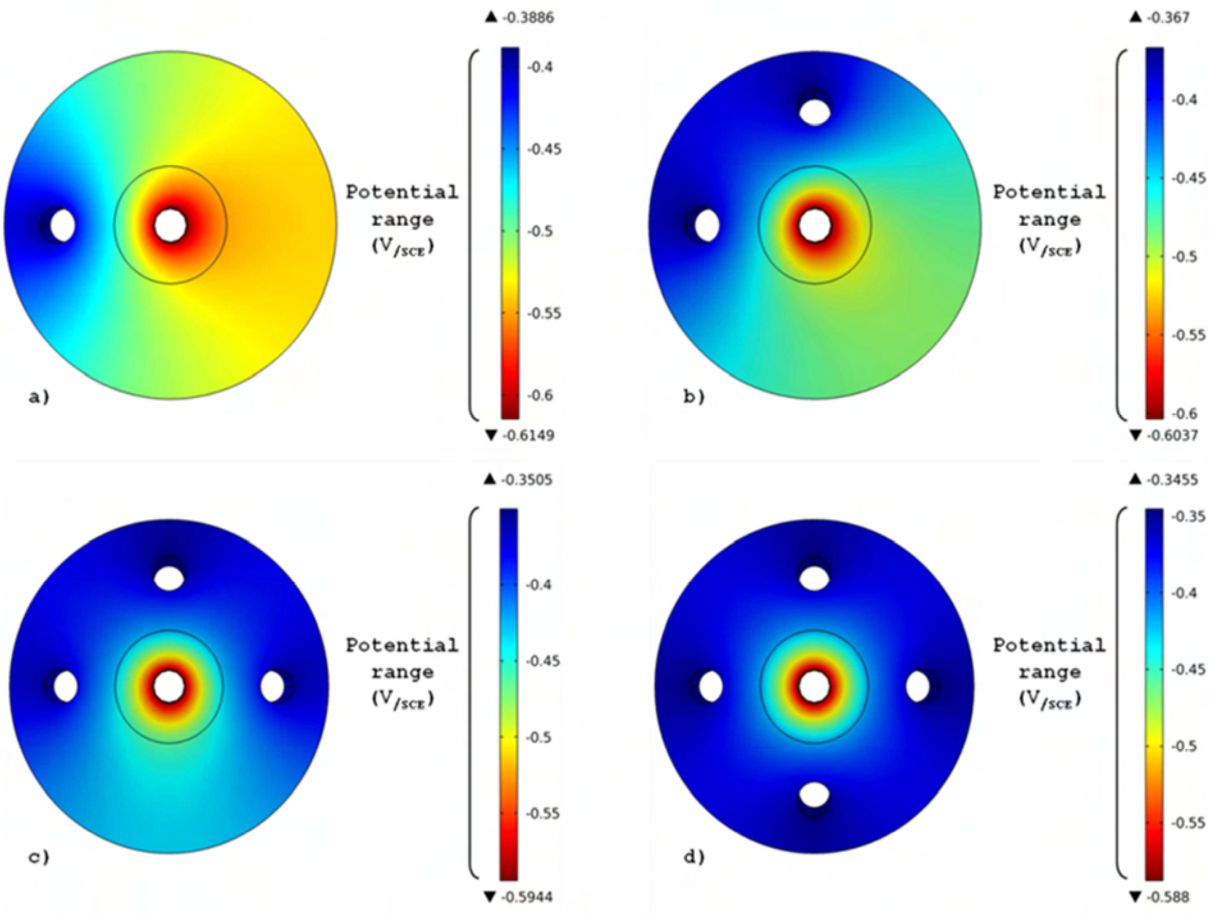

Figure 3-11 Potential field (top view) – a) One passive bar connected - b) Two passive bars connected - c) Three passive bars connected - d) Four passive bars connected

3.6.3 Galvanic current in corrosion specimens

The Figure 3-12 shows macrocell current density streamlines achieved in two simulation cases: one with one passive bar and another with three passive bars connected. Both color and thickness of lines highlight the local norm of the current density vector. In Figure 3-12-a, the effect of the non-negligible resistivity is well illustrated by the fact that most of the exchanged current is flowing straightly from the active bar to the passive one (red and light blue areas). The face-to-face polarization effect is also highlighted since the facing sides of the two bars are revealed by red areas (meaning that the current density is high). Far from the bars, the current lines are thinner, meaning that very little current density is flowing in far areas. As expected, the Figure 3-12-b shows that adding passive bars in the circumferential direction makes more uniform the normal current density produced by the active bar.

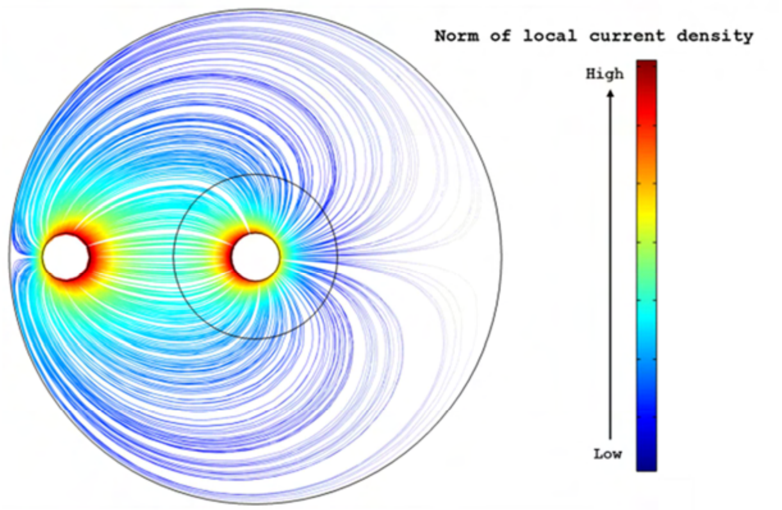

a)

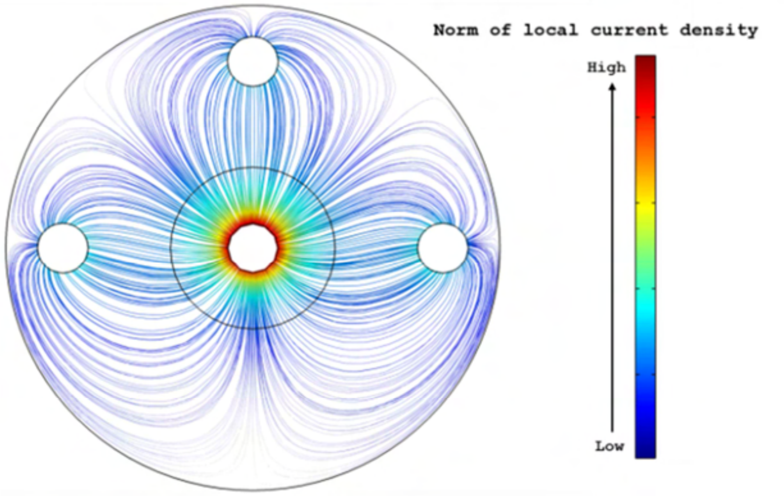

b)

Figure 3-12 Macrocell current density streamlines (top view of the specimens): a) one passive bar connected, b) three passive bars connected

3.7 Parametric study

Parametric study of corrosion current densities (j_{acorr}, j_{pcorr}), corrosion potentials (E_{acorr}, E_{pcorr}) and Tafel slope coefficients (β_{aa}, β_{ca}, β_{ap}, β_{cp}) was performed. To study one parameter its value was varied for selected range while all other parameters were kept constant at base values as in Table 3-1. While selecting the range of parameter’s values under study, the available values in literature and obtained values from Tafel experiments were kept in mind. To measure electrical potential for all parametric values, one point was selected on each bar as shown in Figure 3-13, P_a on active steel and P_c on passive steel respectively.

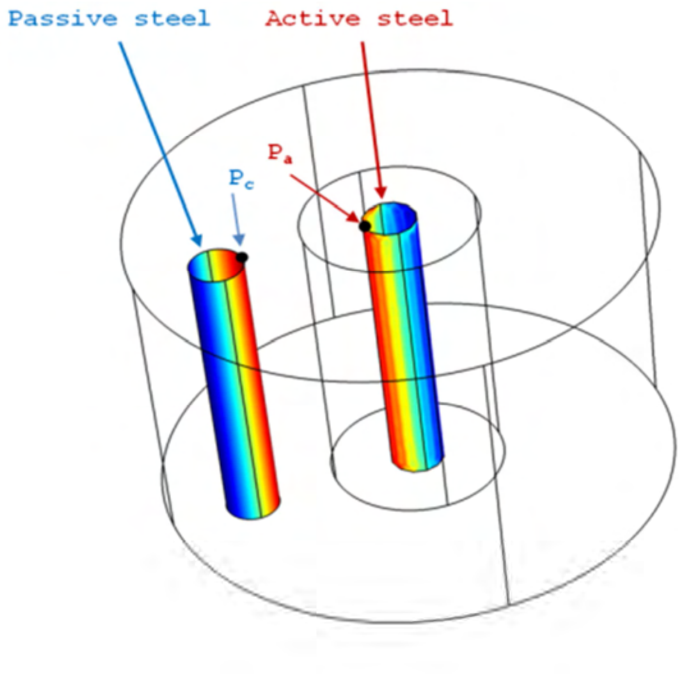

Figure 3-13 Active and passive steel bars with points Pa and Pc respectively, at these points potential values were observed for comparison purposes.

3.7.1 Effects of Corrosion current densities of Active (jacorr) and Passive (jpcorr) steel

The base value of j_{acorr} is 0.5 μA/cm^2 for simulations, which is calculated from extrapolation of polarization curves obtained from steel in carbonated concrete. Effect of change in j_{acorr} on macrocell system is studied by changing its values from 0.1 μA/cm^2 to 1 μA/cm^2. This range is practically logical and available in literature (Warkus et al., 2006). With increase in j_{acorr} the potential at active steel bar (E_a) significantly decreases to more negative values (Figure 3-14), while passive bar potential (E_p) also moves towards negative values but not highly influenced. The difference between two potentials is increased by increasing $j_{acorr,}$ and producing higher driving voltage, hence higher are the macrocell current values. The base value of passive corrosion current density is 0.0.25 μA/cm^2 which is obtained from polarization curves performed on steel in noncarbonated concrete. The effect of change in j_{pcorr} was studied by varying its values from 0.001 μA/cm^2 to 0.05 μA/cm^2, which is also well in accordance with literature. Change in j_{pcorr} has greater influence on passive bar's potential than on active bar's potential, passive bar's potential is attracted towards more positive values (Figure 3-15) with increase in j_{pcorr}, while active bar's potential also moves towards more positive values but change is not as significant as cathodic potential. This creates higher driving potential and results into increase in macrocell current.

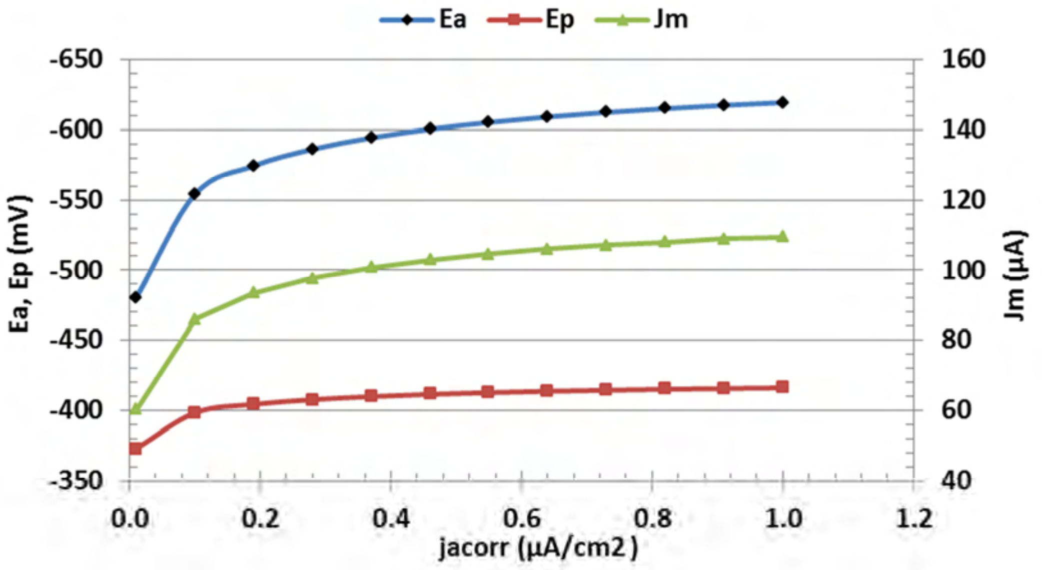

Figure 3-14 Effects of corrosion current density of active bar on macrocell corrosion system

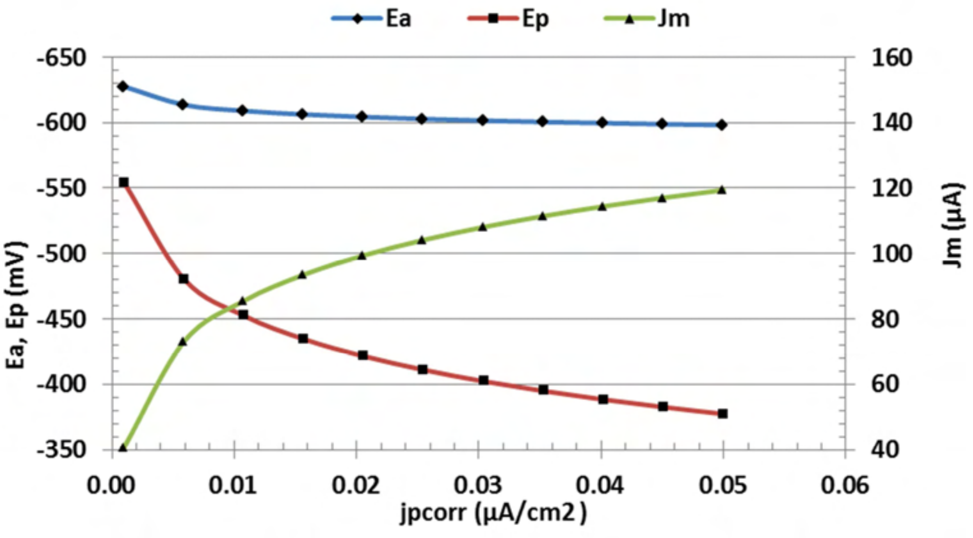

Figure 3-15 Effects of corrosion current density of passive bar on macrocell corrosion system

3.7.2 Effects of corrosion potential of active and passive steel

Normally in the simulation, anodic corrosion potential is set to $-650\ mV/SCE$. This value is obtained from corrosion potential measurement of steel bars in carbonated concrete while performing Tafel experiments. For these parametric studies its values were varied from -400 mV/SCE to -800 mV/SCE. The results are shown in Figure 3-16. The Change in E_{acorr} has a significant influence on anodic potential (E_a) than on cathodic potential (E_p). If E_{acorr} moves toward more negative values, the difference between anodic and cathodic potential increases and that results in higher driving voltage and macrocell corrosion current.

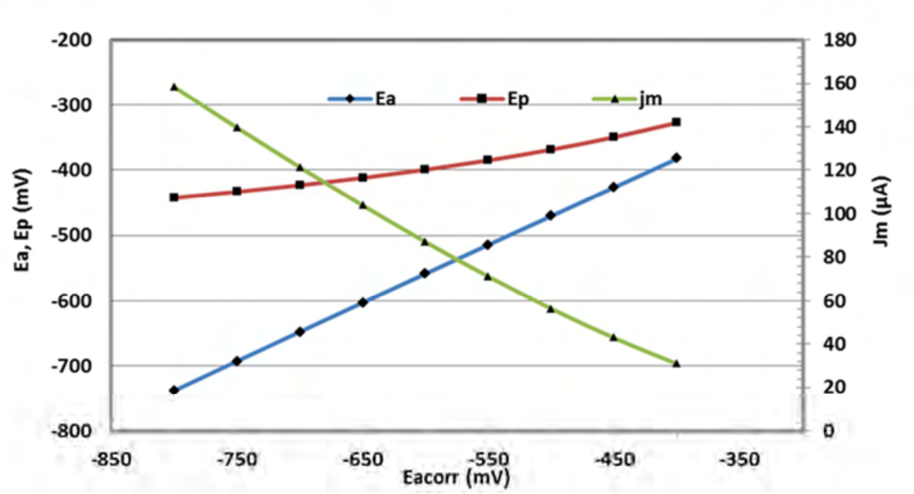

Figure 3-16 Effects of change in corrosion potential of active bar (E_{corr}) on macrocell corrosion system

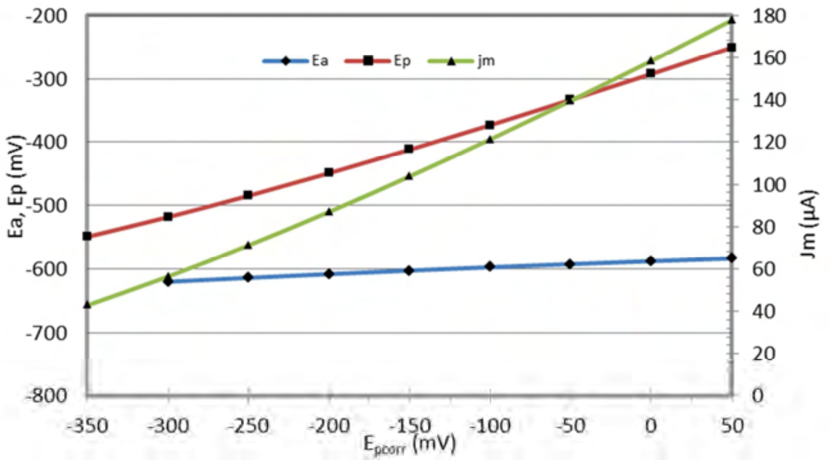

Figure 3-17 Effects of change in corrosion potential of passive bar (E_{pcorr}) on macrocell corrosion system

Macrocell corrosion current is exponentially proportional to E_{acorr}, so little change in E_{acorr} brings about large change in J_m, e.g. 12% change (from -600 $to\ -650\ mV/SCE$) causes 19% increase in macrocell corrosion current. Change from $-400\ to\ -800 mV/SCE$ provides $127\mu A$, which is 421 % increase in macrocell corrosion current.

The effect of corrosion current potential of passive bar (E_{pcorr}) was observed by changing its values from $50\ mV/SCE$ to $-350\ mV/SCE$. The change in E_{pcorr} affects significantly the potential distribution along the cathodic surface, but has less effect on anodic potential. Figure 3-17 shows the values of E_p, E_a and J_m with change in E_{pcorr}. When E_{pcorr} is around its most negative values, the difference between E_{pcorr} and E_{acorr} is small and less driving voltage is available and so macrocell current reduces. On the other hand when E_{pcorr} is more positive the driving voltage is large and hence more macrocell corrosion current is produced. Macrocell current increases or decreases exponentially with change in E_{pcorr} .

3.7.3 Effects of anodic and cathodic Tafel slope coefficients for active steel

In macrocell corrosion system four Tafel slope coefficients are involved, anodic Tafel slopes for active and passive systems and cathodic Tafel slopes for active and passive systems.

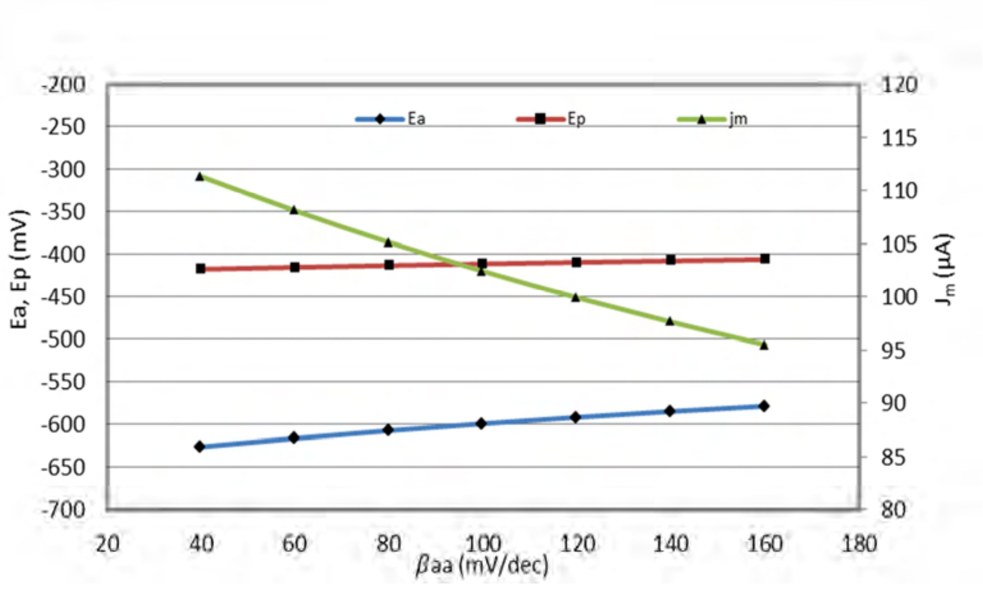

Figure 3-18 Effects of Anodic Tafel slope coefficients of active steel on macrocell corrosion system

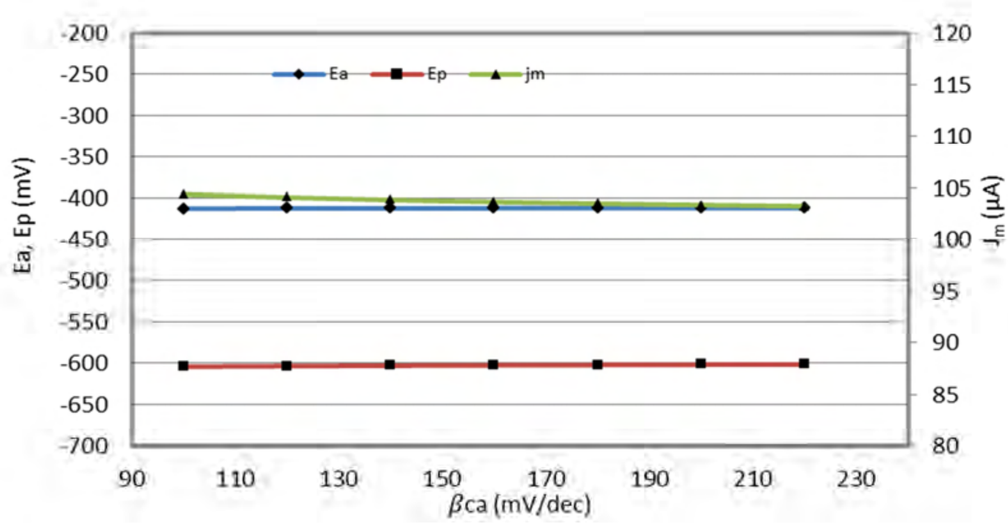

Figure 3-19 Effects of Cathodic Tafel slope coefficients of active steel on macrocell corrosion system

The effects of anodic Tafel slope of active bar β_{aa} are observed by changing its values from $40\ mV/dec$ (for steel with very high corrosion current) to $160\ mV/dec$ (steel with moderate to low corrosion current density). The change in β_{aa} mostly affects the potential distribution along the anodic surface, and has less influence on cathodic system Figure 3-18. As β_{aa} approaches the lower values, macrocell current increases, at $160\ mV/dec$ Jm is $95\ \mu A$ and at $40\ mV/dec$ Jm is $111.5\mu A$, which is only 16% increase with 300% decrease in β_{aa} .

Normally the values of cathodic Tafel slope coefficients are higher than that of anodic Tafel slope coefficients for active steel. The base value of β_{ca} is $150\ mV/dec$ for all other simulations, but when effect of β_{ca} is studied its values were varied from $100\ mV/dec\ to\ 220\ mV/dec$. Figure 3-19 shows that β_{ca} has no effect on macrocell corrosion system, which is well in accordance to the curves presented in Figure 3-7, which show that only the anodic branch of active steel is involved in macrocell corrosion system.

3.7.4 Effects of anodic and cathodic Tafel slope coefficients for passive steel

Figure 3-20 shows the effects of anodic Tafel slope coefficients of passive bar $\beta_{ap,}$ it was varied from 300 mV/dec to 400 mV/dec. It clearly from the Figure 3-20 that change in β_{ap} has no effect on macrocell corrosion system, because anodic branch of passive steel does not take part in reaction after two bars comes into contact.

The cathodic Tafel slope coefficient of passive bar tends to have lower values than anodic Tafel slope coefficient. The base value of β_{cp} used in simulations is 150 mV/dec, but for parametric studies it was varied from 100 to 220 mV/dec. The results are shown in Figure 3-21. The influence of β_{cp} is quite significant on macrocell corrosion system. When β_{cp} is increased the potential of passive bar moves towards negative potential, and potential of active steel also polarized towards negative potential, but not significantly. In result driving voltage is low and macrocell current is also reduced. On the other hand if its value is decreased from 200 to 100 mV/dec, the current is increased from 78.2 to 135.78 µA, which is an increase of 73%.

All the results of parametric study are well in accordance with the theoretical explanation of Butler-Volmer kinetics in case of macrocell corrosion system as in Figure 3-6 and Figure 3-7. The driving voltage which depends on active and passive corrosion potentials is a dominating factor in macrocell corrosion system, while corrosion current density does not influence the system significantly. Corrosion current density of active steel has very little influence on macrocell current after certain increment, as shown by the curve in Figure 3-14.

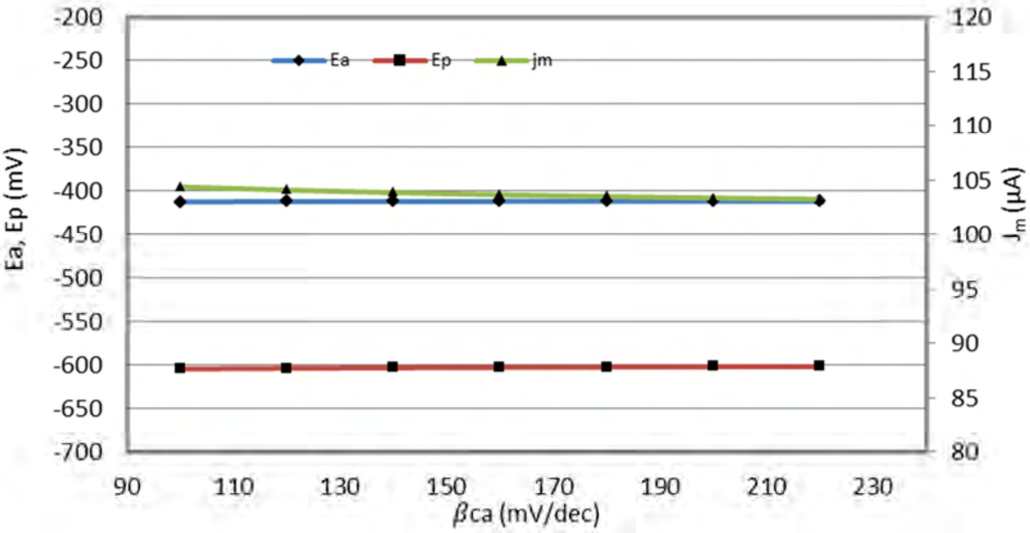

Figure 3-20 Effects of Anodic Tafel slope coefficients of passive steel on macrocell corrosion system

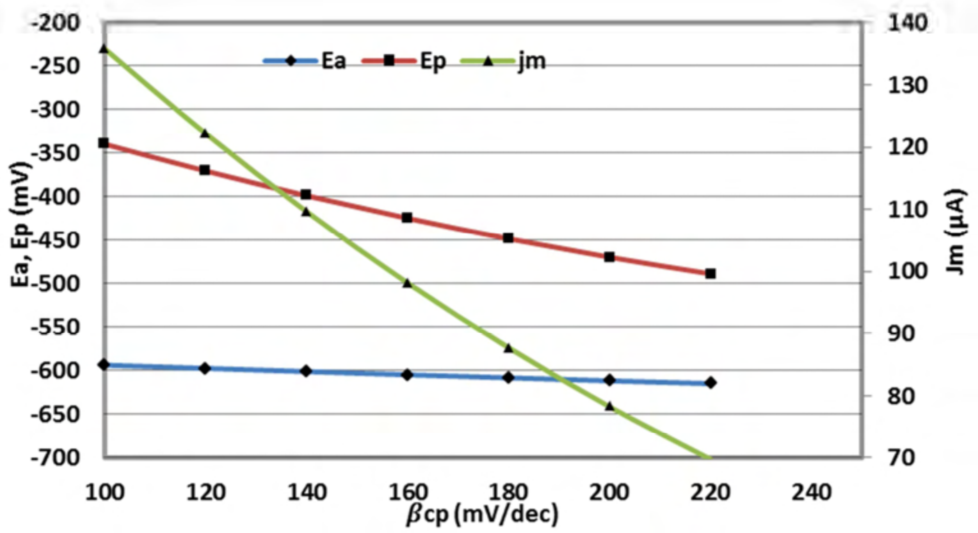

Figure 3-21 Effects of Cathodic Tafel slope coefficients of passive steel on macrocell corrosion system

The parameters of passive system are more influent than the parameters of active system, which shows that the controlling factor in macrocell reaction is cathode system. For example, 50 % increase in j_{acorr} from its base value (0.5µA/cm^2 to 0.75 µA/cm^2) produces 4.5% extra current, while 50 % increase in j_{pcorr} from its base value (0.025 to 0.0375 µA/cm^2) produces 8.5 % more current. Similarly, 30% decrease in β_{aa} from base values (90 to 63mV/dec) produces 2.9 % higher macrocell current, while 30% decrease in β_{cp} produces 9% increase in macrocell current. (Warkus et al., 2006) also have proved that if electrolytic resistivity is less than 1000 Ω.m the controlling factor in macrocell reaction is cathode system.

3.7.5 Effects of concrete resistivity

The theoretical effect of concrete resistivity on galvanic system equilibrium is studied here thanks to numerical simulations involving one active bar connected to one passive bar (C/A=1/1). Electrical resistivity was varied from a very low value of $50\ ohm.m$ (relative to saturated concrete) to a very high value of $3000\ ohm.m$ (expressing dry concrete) (Gjorv et al., 1977; Polder et al., 2000; Warkus and Raupach, 2008). In this section, the resistivity of whole geometry was considered as uniform in the concrete volume (no difference between inner and outer domain). The results are shown in Figure 3-22, where active and passive potential values are taken at points $\mathbf{P_a}$ and $\mathbf{P_c}$ defined in the Figure 3-13 respectively. The difference between passive and active potential values ($E_p - E_a$) will be referred to as the ohmic drop (or IR drop). The ohmic drop primarily depends on electrical resistivity of concrete, but also on electrochemical parameters. In case of one-dimensional electrical flow, the ohmic drop is easy to define since each reactive surface is uniformly polarized (all points of a reactive surface at the same potential). However, for three-dimensional electrical flows, which are normally encountered in galvanic corrosion problems associated with reinforced concrete, reactive surfaces are not uniformly polarized, i.e. potential gradients exist on active and passive areas. Therefore, ohmic drop also depends on the couple of active-passive points (**P_a**,**P_c**) considered. In this study, the attention is focused on the points $\mathbf{P_a}$ and $\mathbf{P_c}$ undergoing maximum anodic and cathodic polarization, respectively. The macrocell current J_m is deduced from integration of normal current density on active boundary.

When resistivity approaches to zero, active and passive potentials at equilibrium tend to be close to each other (low ohmic drop). On the other hand, if concrete resistivity is very high, ohmic drop is higher. As expected, the macrocell corrosion current reduces with the increase in concrete resistivity. It shows that even after the depassivation of steel bars the macrocell corrosion current can be insignificant if concrete has high resistivity, because ionic current encounters a large resistance.

Through numerical simulation Warkus and Raupach, (2008) and Warkus et al.(2006) have also observed the effect of resistivity on macrocell corrosion current and found same kinds of results.

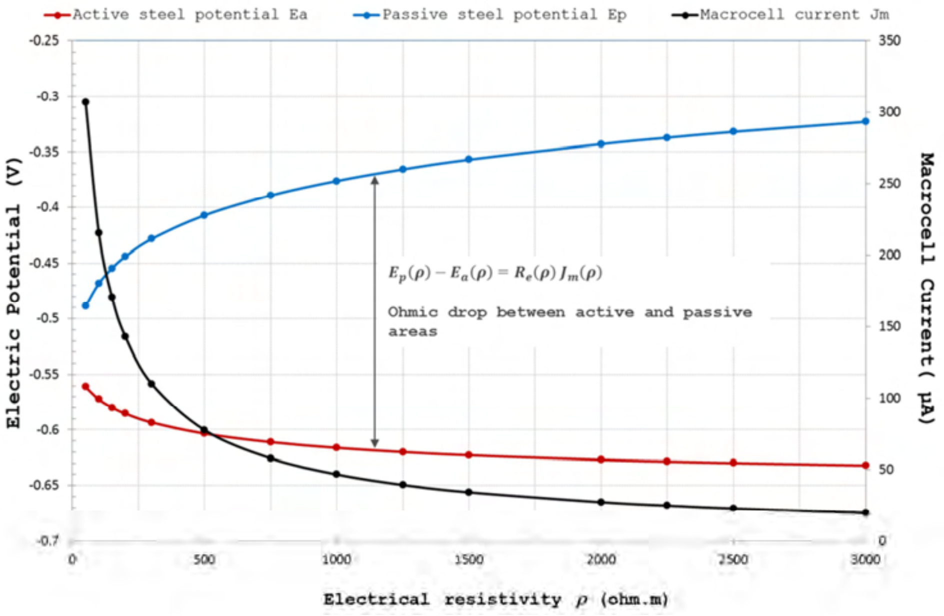

Figure 3-22 Effect of concrete resistivity on galvanic system variables: uniform resistivity

The ohmic resistance R_e is depending on electrical resistivity of concrete ρ and system geometry. Regarding the specific geometry of the specimen studied here, the relationship between R_e and ρ can be deduced from the three curves presented in the Figure 3-22, as follows:

$$R_e(\rho) = \frac{E_p(\rho) - E_a(\rho)}{J_m(\rho)} \qquad (10)$$

The result plotted in the Figure 3-23 involving all values of electrical resistivity tested in the simulation, highlights the linear relationship between concrete resistivity and ohmic resistance linking the specific points $\mathbf{P_a}$ and $\mathbf{P_c}$. As the macrocell current is a global information on the system (resulting from current density integration) while E_p and E_a are local information (depending on the points chosen), the ohmic resistance R_e is also a local information and only characterizes the set of points considered. Therefore, the slope of the linear regression could be defined as a local cell constant relative to the point set ($\mathbf{P_a}$,$\mathbf{P_c}$).

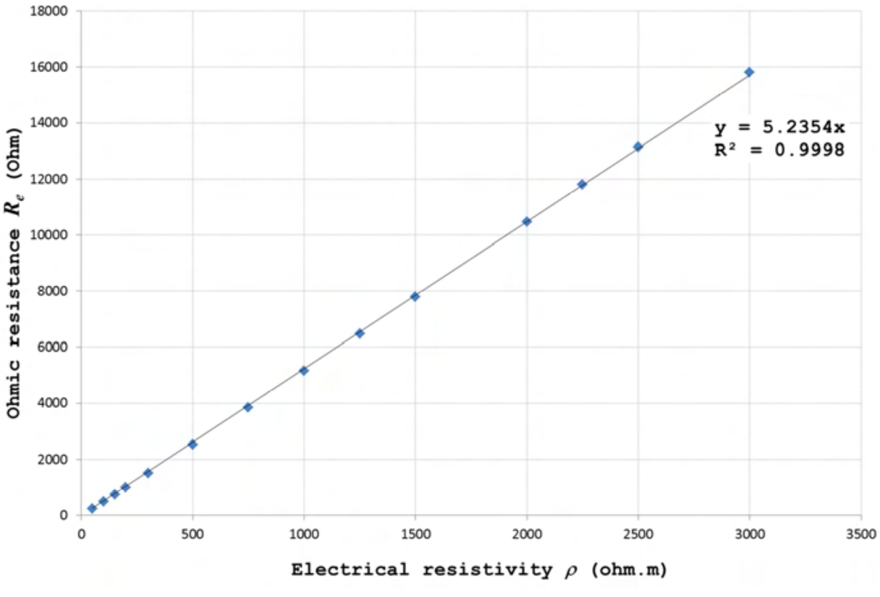

Figure 3-23 Local ohmic resistance versus electrical resistivity of concrete

3.8 Conclusions

Comsol Multiphysics® a powerful tool to simulate the physical phenomena, the convergence to a unique solution was achieved easily. The model of corrosion in reinforced concrete, where current flow in concrete volume is governed by the ohm’s law, the law of charge conservation is applied and the steel-concrete interface is model by Butler-Volmer equation, such model show exactly the same behaviour as elaborated by the theoretical polarization curves of a galvanic/macrocell corrosion system.

The parametric study shows that in a macrocell corrosion system where is resistivity of concrete is not very high, the passive (cathodic) system is a governing factor.

CHAPTER # 4

4 Experimental and Numerical Validation of the Accelerated Corrosion Test

---

4.1 Introduction

In the previous chapters the acceleration of initiation phase of corrosion process was discussed. This chapter elaborates the experimental and numerical results to validate that the corrosion can also be accelerated in propagation phase by galvanic coupling of one or several passive steel bars with an active steel bar. The results of experiments and numerical simulations are also compared in this chapter. By changing Cathode/Anode ratio two main parameters of macrocell corrosion system were studied numerically as well as experimentally. Those two parameters are potential distribution during the course of experiment and macrocell corrosion current.

4.2 Experimental program

Fifteen cylindrical concrete samples were casted for accelerated galvanic corrosion tests. With the geometry of samples used (as discussed in chapter 3) it was possible to connect up till four cathodically acting passive steel bars with the anodically acting active bar. To observe the effect of increase in cathodic surface area on corrosion current density and on the polarization behavior of active and passive corrosion systems, two configurations of laboratory experiments were used.

4.2.1 **Configuration** A

In this configuration only one sample was used to configure a connection between a certain amount of passive steel bars with the active bar. On the basis of connected passive bars this configuration is divided into further four sub configurations, i.e.

- A1: one passive bar is connected with central active bar (Figure 4-1)
- A2: two passive bars are connected to central active bar (Figure 4-2)
- A3: three passive bars are connected to central active bar (Figure 4-3)
- A4: four passive bars are connected to central active bar (Figure 4-4).

Figure 4-1 to Figure 4-4 show a schematic of all samples before the electrical connection. For configuration A1 only three samples were tested, while for the other three configurations 4 samples were tested for galvanic corrosion current. The reason of adopting configuration A was to have an undisturbed galvanic system at which direct effect of available cathodic area can be studied. This configuration also gives us the choice to select the passive bars which had a potential value near to the average value, and to ignore those who showed a large deviation from average value. With this configuration we can create the galvanic systems which would not be influenced greatly by the difference of cell potential but only by the increase or decrease in number of passive bars.

The name of the samples are given according to the active bar's number and the number of passive bars (cathodes) connected with, e.g. 1C-38 is a sample whose active bar was 38 and was connected to one passive bar. Similarly the sample 2C-08 (Figure 4-2) has an active bar whose number was 08 and where 2 passive bars are connected to the active bar.

Table 1 shows the potential of active and passive bars of all the samples. It also shows the cell potential (electromotive force), which depends on the potential of both active bar and the number of passive bars connected to it. In case where more than 1 passive bar is connected, electromotive force is calculated by following equation (Eq.4.1).

$$Cell\ potential\ (emf) = \left(\sum_{i=1}^{n} \frac{Ecorr_{p_i}}{n}\right) - E_{acorr} \qquad \text{Eq. 4.1}$$

Where n is the number of passive bars connected to the active one (1, 2, 3 and 4).

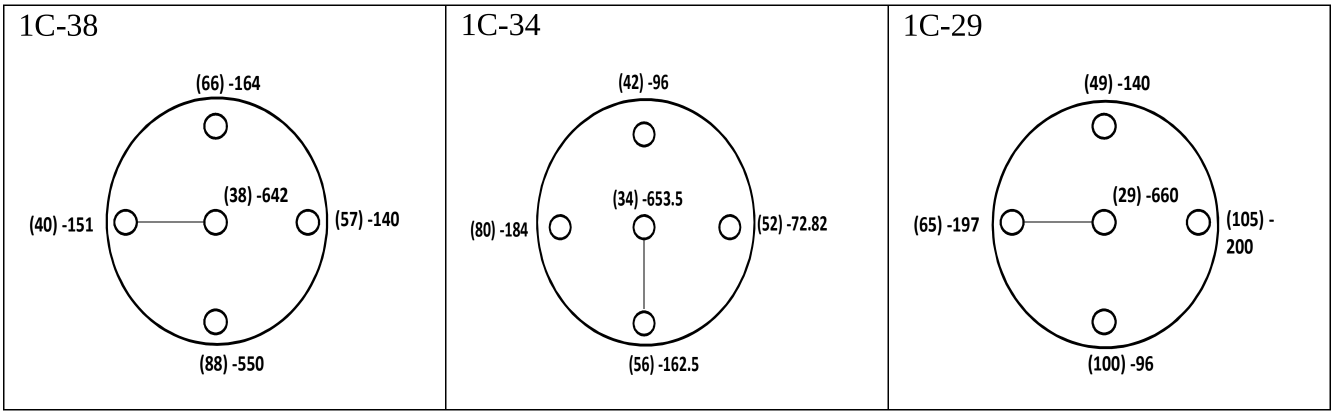

Figure 4-1 Configuration A1, : one passive bar connected with central active bar. The bar connected is shown by a line, connecting it to central active bar. In parenthesis are the designated names of bars, the open circuit potential of the bars is given in mV/SCE.

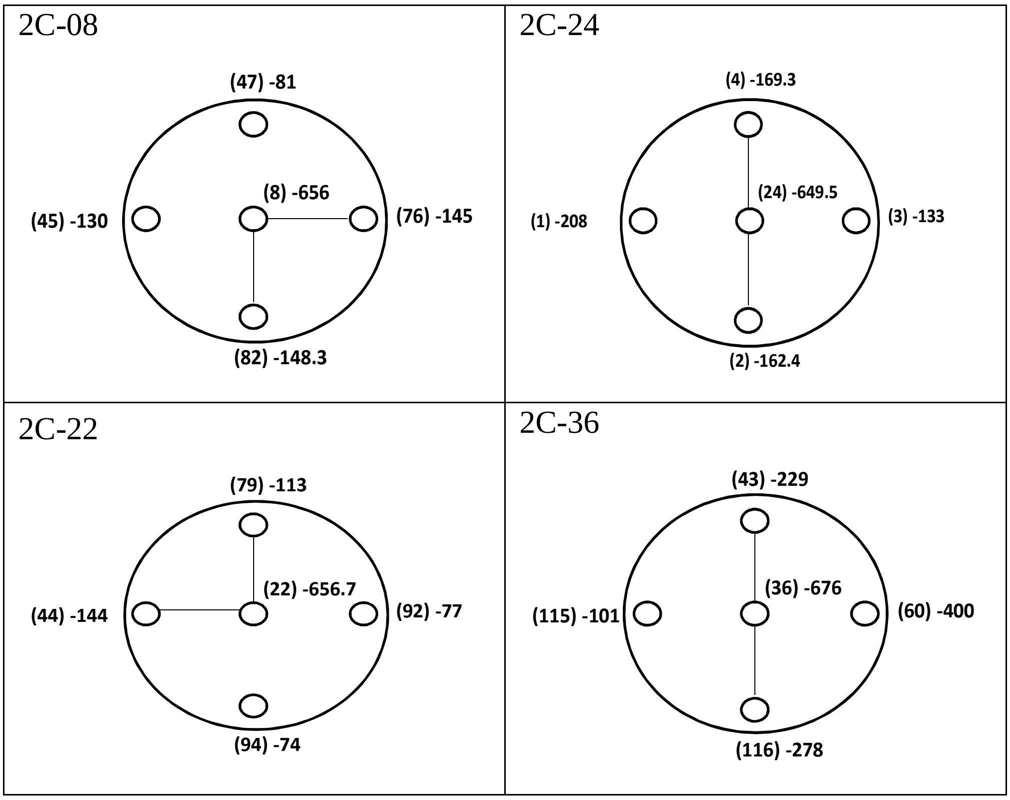

Figure 4-2 Configuration A2: two passive bars connected with central active bar.

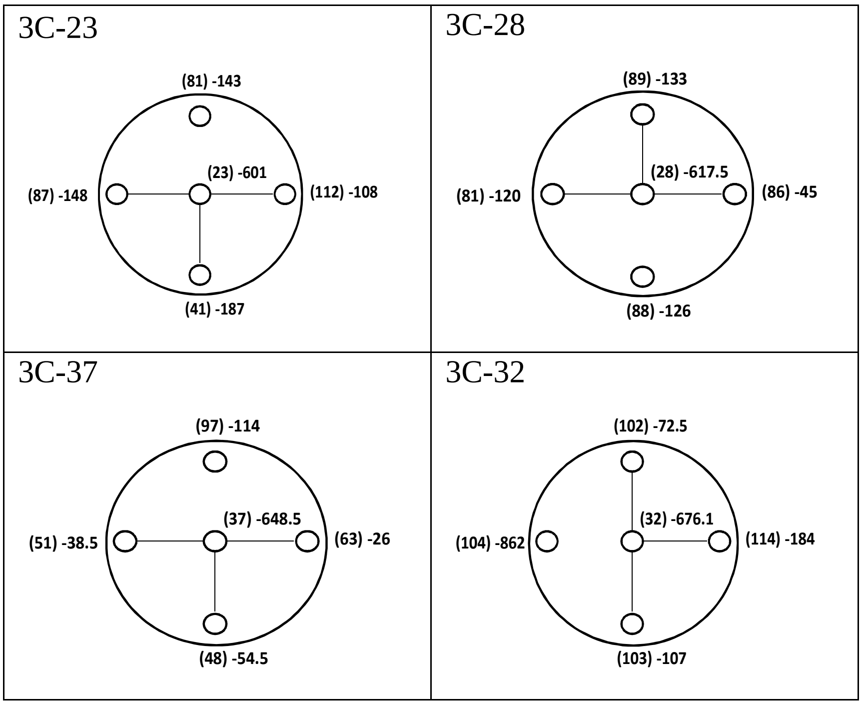

Figure 4-3 Configuration A3: three passive bars connected with central active bar.

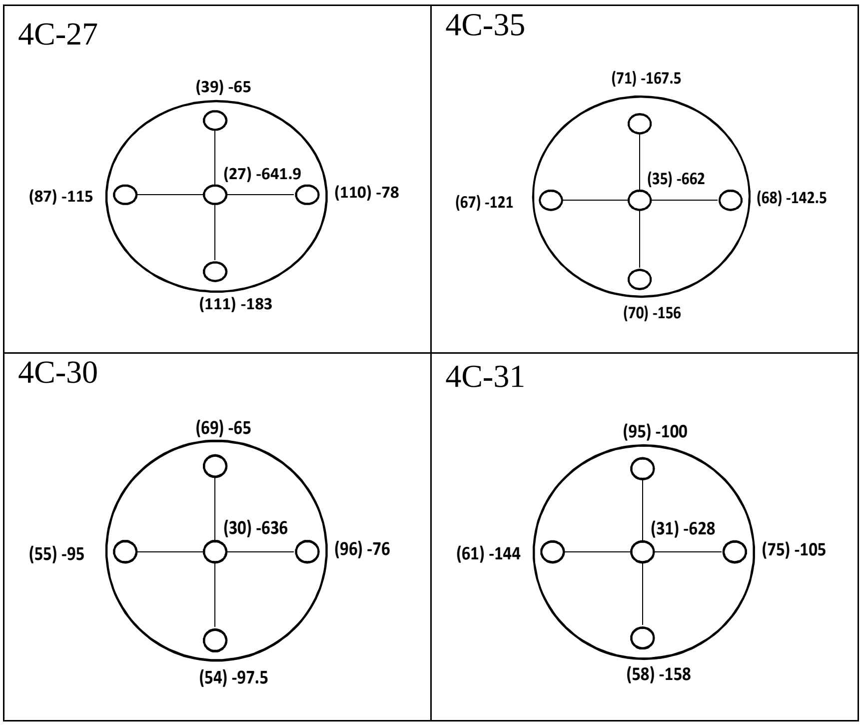

Figure 4-4 Configuration A4: four passive bars connected with central active bar.

Table 4-1 Free potential of both active and passive bars for all the samples (the values in bold case are the potential of bar connected as shown in Figure 4-1 to 4-4).

No. of passive bar connected	Sample designation	Active bar potential	Passive bar potential				Electromotive force
		(mV/SCE)	(mV/SCE)				(mV/SCE)
1	1C-38	-642	**-151**	-164	-550	-140	-491
	1C-29	-660	**-197**	-140	-96	-200	-463
	1C-34	-653	**-162**	-184	-96	-73	-491
2	2C-08	-656	**-148**	**-145**	-81	-130	-509
	2C-24	-649	**-162**	**-169**	-208	-133	-483
	2C-36	-676	**-229**	**-278**	-101	-400	-422
	2C-22	-656	**-113**	**-144**	-74	-77	-528
3	3C-23	-601	**-108**	**-148**	**-187**	-143	-453
	3C-28	-617	**-126**	**-120**	**-133**	-45	-491
	3C-32	-676	**-184**	**-73**	**-107**	-862	-554
	3C-37	-648	**-26**	**-39**	**-54**	**-114**	-608
4	4C-27	-641	**-65**	**-115**	**-183**	**-78**	-531
	4C-30	-636	**-65**	**-95**	**-97**	**-76**	-552
	4C-31	-628	**-100**	**-144**	**-158**	**-105**	-501
	4C-35	-662	**-168**	**-121**	**-156**	**-143**	-515

4.2.2 Configuration B

In this configuration, on a same sample, passive steel bars were progressively increased in the galvanic corrosion system, i.e. at first, only one passive bar was connected with active bar, then after stabilization of current another passive bar was also connected and the process went on until all the four passive bars embedded in the sample were connected to the active one. The samples used for configuration A were used again in configuration B. In total 13 samples were tested with this configuration, which are given in Table 4-1. The samples 4C-30 and 4C-31 could not be tested for this configuration because they were autopsied at the end of configuration A.

4.3 Comparison of numerical and experimental results

4.3.1 Potential range of active and passive bars

Before connecting passive and active bars, the free corrosion potential of all the steel bars embedded in the samples was measured. The Figure 4-5 presents the statistical distributions of potential values measured on passive and active steel bars respectively. The corrosion potential of active steel bars was in the range of $-600\ to\ -675\ mV/SCE$, with an average value over 15 samples of -647 mV/SCE and a median value of 649.5mV/SCE. The standard deviation of active bar potential was only 19 mV/SCE.

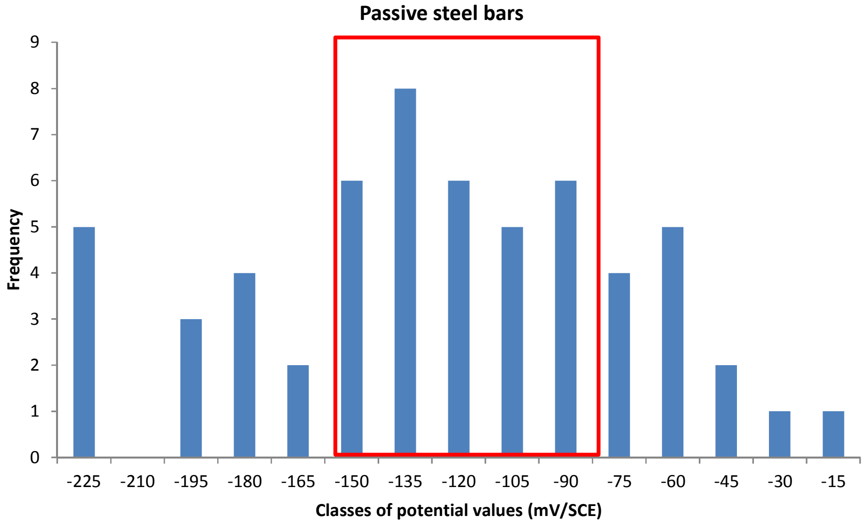

a)

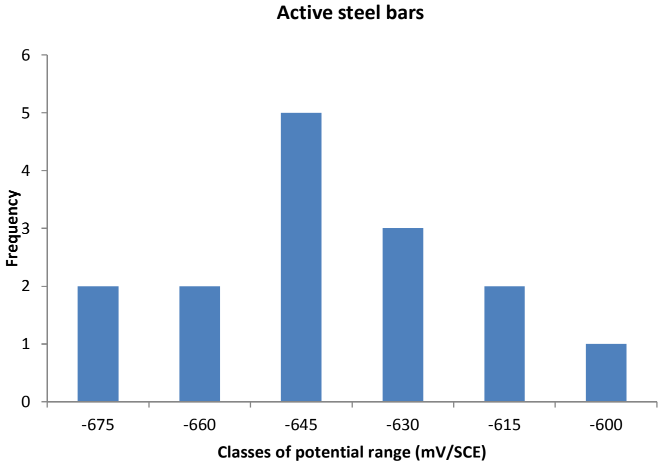

b)

Figure 4-5 Statistical distribution of free potential values achieved, a) on passive steel bars, b) on active steel bars

The free corrosion potential of passive bars was more dispersed, the range found was from $-15\ to - 225\ mV/SCE$, with an average value over 57 steel bars was around $-132.6\ mV/SCE$ while the median value was $-130\ mV/SCE$. There were three passive bars having corrosion potential around $-862, -550\ and\ -400\ mV/SCE$. These values were ignored during calculation of average and median. The standard deviation of passive bar potential was $89\ mV/SCE$. The reason of this large range of values has already been discussed in second chapter, i.e. the range of passivity potential could vary from $+200\ mV/SCE\ to\ -400\ mV/SCE$. The most probable experimental values of corrosion potential observed for passive and active steel bars are $-135\ mV/SCE$ and $-645\ mV/SCE$ respectively. These values are well in accordance with E_{corr} values used in numerical simulations presented in chapter 3, i.e. $-150\ mV/SCE$ and $-650\ mV/SCE$, respectively. In Figure 4-5 the active steel bar histogram shows a lower number of values since, for each specimen, there were only one active bar and four passive bars.

4.3.2 Potential mapping on experimental sample and potential field with numerical simulations

Circumferential potential mapping was performed on experimental specimens according to the protocol presented in the Figure 4-6. The potentials were measured during the galvanic experiment along vertical lines at positions 1, 2, 3 and 4. Along the lines the measurements were done at 3 points $a, b\ and\ c$, which are at $2, 6$ and $10\ cm$ from top surface, respectively. The Figure 4-7 illustrates thanks to a polar plot the circumferential potential field measured on these points at outer boundaries. Two types of samples were selected to show the effect of number of passive bar connected on potential distribution. The first sample (1C-38) involves only one passive steel bar connected to the central active bar (red points on polar plot in Figure 4-7), while the second one (4C-27) consists of four passive bars connected to the active one (blue points). In order to make clearer the fundamental difference between the two specimens, each point corresponds to the average value of the three records (a, b and c) collected along each line (Figure 4-6). The error bar in the case of 1C-38 on polar plot shows the maximum and minimum values of the connected passive bar. In case of sample 4C-27, the error bar is shown for a passive bar which was more polarized than others.

The Figure 4-7 also makes a comparison between the theoretical potential fields achieved by numerical simulations relative to the configuration of the two specimens tested with the experimental values obtained. On the right of the Figure 4-7 the illustration represents the potential field obtained by numerical simulations with one and four passive bars connected with active one respectively.

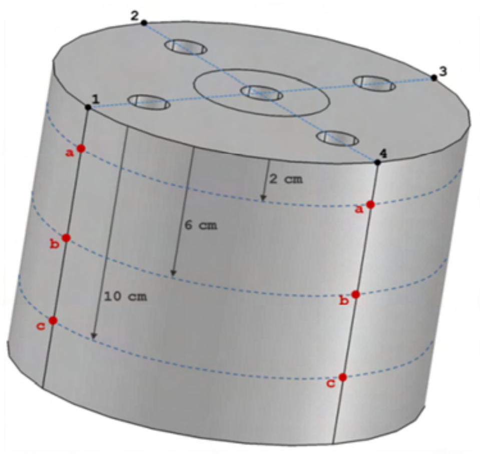

Figure 4-6 Schematic of experimental sample: a, b, c are points where experimental and numerical potential values were compared

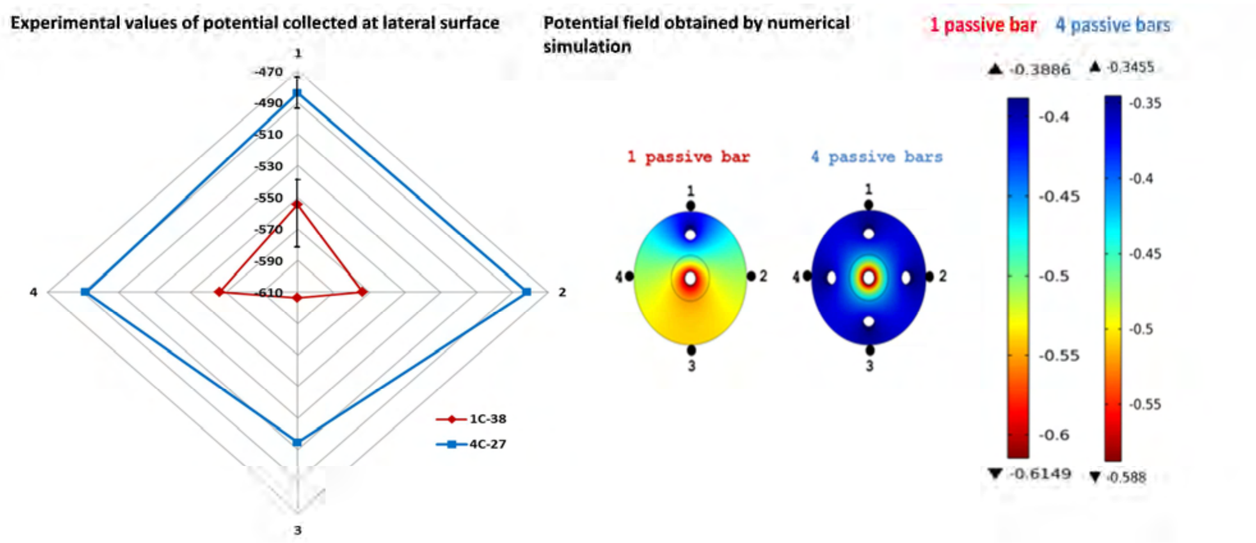

Figure 4-7 Potential field collected on lateral surface of two galvanic corrosion specimens: specimen with one passive bar connected (red) and specimen with 4 passive bars connected (blue)

On the Figure 4-7, two main differences are revealed by the polar plot. As predicted by numerical simulations, it is first observed that the sample 4C-27 shows quite a cylindrical symmetry regarding the circumferential potential field, highlighting the existence of a uniform potential field for the specimen involving 4 connected passive bars.

On the other hand, the specimen 1C-38 with one passive bar connected shows a great difference in potential values between diametrically opposite points 1 ($E = -554\, mV/SCE$) and 3 ($E = -603\, mV/SCE$), close to passive and active bars, respectively, as shown in

Figure 4-7. Moreover, the records collected at points 2 and 4 show that the potential value changes progressively on the circumference from a maximum (at position 1) to minimum (at position 3). The potential gradient appears clearly in this case.

The qualitative behavior of experimental samples and simulations are quite similarly, i.e. the potential near the connected passive bar in the case where only one passive bar is connected (1C-38), is less electronegative, which means it is more polarized, same behavior is shown by simulations when only one passive bar is connected. But the difference in potential values is significant in both cases, in experimental sample the potential is around $-554\, mV/SCE$, while in case of simulations it was around $-450\, mV/SEC$ as can be seen in the scale of simulation results (blue area; 1 passive bar scale). The same remark can be done with sample 4C-27, where all four passive bars were connected. The circumferential potential near the passive steel bars was around -475 mV/SCE, while the values in case of numerical simulation were found to be around $-350\, mV/SCE$ (blue area of scale with 4 passive bars). A difference of about $100\ to\ 125\, mV/SCE$ is found between experimental and numerical values in both case of 1 or 4 passive bars connected to active one. This difference can be explained by the fact that the corrosion conditions supposed in numerical simulations are different from the conditions in real samples. For example, with numerical simulations it has been seen that if the concrete resistivity is higher, the difference between active and passive bar potential is also higher at equilibrium in galvanic system. Moreover the cathodic tafel slope of passive system β_{cp} values in simulation were supposed as $150\, mV/dec$, and with sensitivity analysis it has been observed that if β_{cp} is increased, the potential of passive steel bar reduced to very negative values at galvanic equilibrium, which makes cell potential also more negative. This could clearly explain the more electronegative potential in case of experimental sample, which could have a polarization curve with higher Tafel slope (β_c) and concrete has less resistivity.

Another major difference is highlighted by the global potential levels related to the two experimental specimens. Globally, the specimen with one passive bar connected has potential values lower than those of the specimen with 4 passive bars connected, even close to the connected passive bar (position 1). This observation is in accordance with the theoretical effect of the increase in the cathode-to-anode surface ratio discussed in potential distribution section in the third chapter. Increasing the number of passive bars results in higher anodic polarization of active steel and lower cathodic polarization of passive steel. Regarding outer potential measurement of galvanic systems, a system involving a high cathode-to-anode ratio may globally have higher potential values than a system with low cathode-to-anode ratio. This result confirms that half–cell potential measurements are not sufficient to deduce information on corrosion state in reinforced concrete, since high corrosion rate systems (due to high C/A ratio) may appear with higher potential levels than low corrosion rate systems.

4.3.3 Accelerated Macrocell current in corrosion specimens

In this section, the numerical results of the effects of Cathode/Anode ratio on macrocell current density are firstly presented. Then the results of laboratory experiments are explained. As macrocell corrosion current depends on potential at steel surface, it is essential here to mention that the numerical results of potential distribution during galvanic connection are already been presented in section 3.6.2 and 4.3.2.

4.3.3.1 Numerical calculations of macrocell current

The global macrocell corrosion current J_m may be simply deduced from numerical simulations by the integration of normal current density j_n on the active boundary surface S_a (Eq.4.2).

$$J_m = \iint_{S_a} j_n \, \mathrm{d}S_a \qquad \text{Eq. 4.2}$$

Several simulations were carried out to study the effect of cathode-to-anode ratio (C/A) on the macrocell current J_m. Anode surface area was kept constant while cathodic surface was changed by increasing the number of passive steel bars in the system. These simulations involved 1 to 8 passive bars connected to a central active bar, corresponding here to C/A ratios from $1/1$ up to $8/1$. The results of the numerical experiments are presented in the Figure 4-8. As it may be seen in the Figure 4-8, the macrocell current density is increased with the cathode surface, which means that more corrosion is occurring with large available cathode area in concrete. When C/A ratio is $1/1$, 103 μA current is produced, while it is 154 μA when C/A is $2/1$. It gradually increases with increase in C/A ratio, and reaches to 254 μA when C/A is $8/1$. Nevertheless, the rate of increase in macrocell current is decreased with C/A. For instance, 45 % additional current is produced when changing from one to two cathode bars, but only a 23 % increment is observed when 3 cathode bars are simulated instead of two. At last, the rate of increase is only 3.5 % from 7/1 to 8/1.

Arya and Vassie, (1995) has performed same kind of experiments in laboratory on prismatic concrete samples, with anodic steel in the middle and several coplanar cathodes one beside each other. The author found similar qualitative results and demonstrated that the increase in C/A increases corrosion current density. He also observed that the increase in current rate decreases with cathode-to-anode ratio. He observed an increment of 70 % in current density when C/A is varied from 50/1 to 100/1, and only 35 % increase in current from 100/1 to 150/1. Warkus and Raupach, (2008) have performed numerical simulations to study the effects of C/A ratio and achieved a 19% increment in macrocell current density for C/A ratio varying from 18/1 to 34/1, versus 30 % from 18/1 to 54/1. In our study, C/A ratio has greater influence due to the cylindrical geometry of samples used, all passive bars being at the same distance from the active one and having the same influence on the galvanic system. If passive bars are coplanar with active bar as in the work of Warkus and Raupach, (2008), the macrocell current is lower since the furthest bars have less influence on the galvanic equilibrium than the nearest ones.

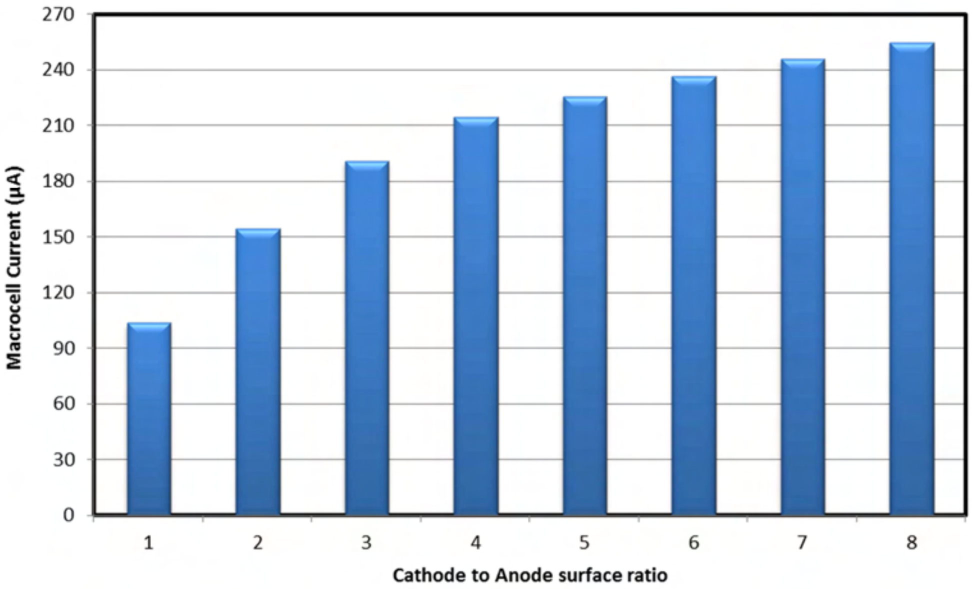

Figure 4-8 Effect of cathode-to-anode ratio on the macrocell current in simulated galvanic systems

4.3.3.2 Experimental measurements of macrocell current

4.3.3.2.1 Results of configuration A

Figure 4-9 shows a sample which was selected to configure a connection between one passive steel bar with the central active steel bar. All the samples were partially submerged in concrete during the galvanic corrosion current measurements. The connection was made by stainless steel clamps rather than soldering the wire to the bar, because with soldering the temperature can change the equilibrium condition of the samples. The selection of passive bar was made depending on their free corrosion potential. Generally the bar which had a corrosion potential around $-150\ mV/SCE$ was selected for connection as shown in Figure 4-1.

Figure 4-9 Experimental sample with one passive bar connected to central active bar via 1Ω resistance of Yokogawa MW 100 ®

For each sample the current values were considered after the stabilization. The results shown in Figure 4-10 present the monitoring of macrocell current during the first 27 days of galvanic connection. The initial part of *macrocell current vs time* plot is magnified to emphasize the time required to reach the stabilization of the current. Two of these three samples had a galvanic corrosion current 38 μA and 46 μA respectively after stabilization, while one sample showed a higher amount of current i.e. 147 μA. The higher values could primarily be due to the higher electromotive force developed between active and passive bars due to a large difference in corrosion potential between active and passive bars connected. However, the electromotive force generated due to the potential difference in all three samples is not dispersed hugely from one sample to another as shown in table 1. So the difference in macrocell current can also be attributed to the corrosion parameters like Tafel slope coefficients and corrosion current density at passive and active steel bars. A more detailed discussion is carried out on this point at the end of this section.

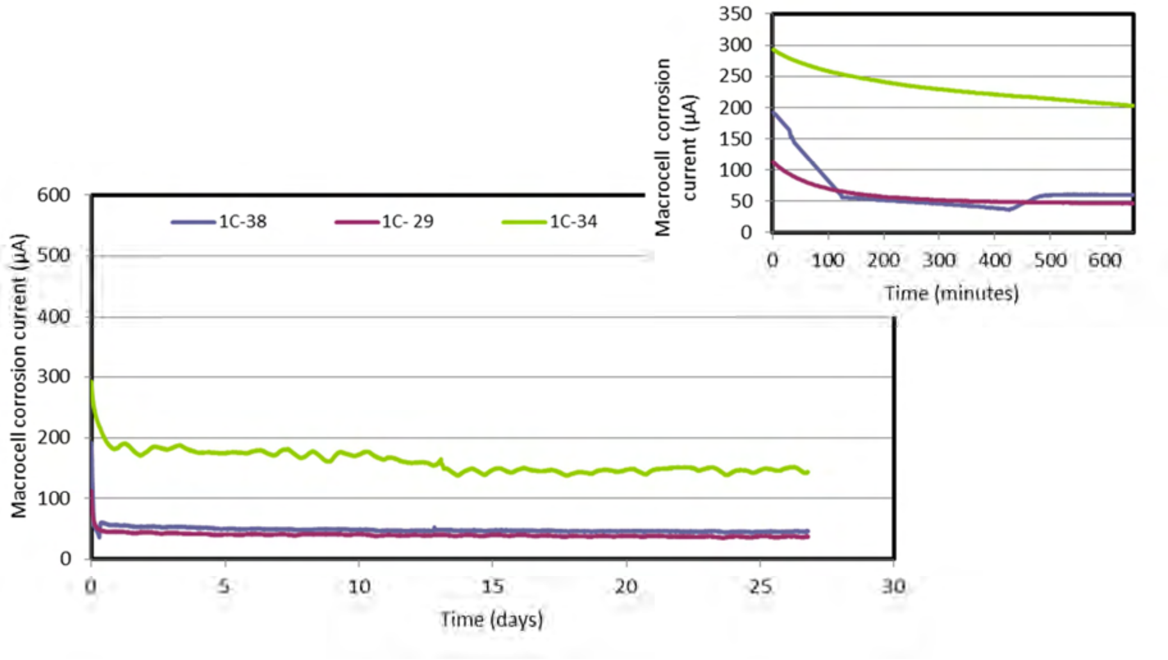

Figure 4-10 Macrocell current on samples with one passive bar connected to active one

Four samples 2C-08, 2C-36, 2C-22 and 2C-24 were selected to configure the connection of two passive steel bars with the active bar. The monitoring of macrocell corrosion current is shown in Figure 4-11. All the four samples show the same range of current after stabilization. The current values were between $88\ to\ 142\ \mu A$. In general, three times higher macrocell corrosion current was observed with two passive bars connected instead of one.

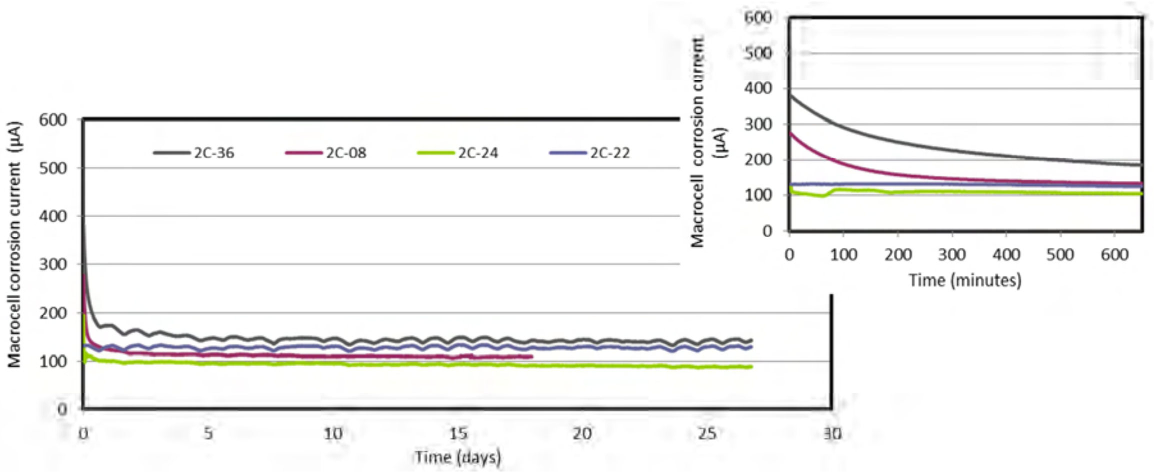

Figure 4-11 Macrocell current on samples with two passive bars connected to active one

Figure 4-12 shows the results of galvanic monitoring of the samples with three passive bars connected with central active bar. The macrocell corrosion current values were found in the range from $175\ to\ 269\ \mu A$. In numerical simulations we observed that the rate of increase in macrocell corrosion current decreases with addition of passive bars, the same tendency is found in laboratory experiments.

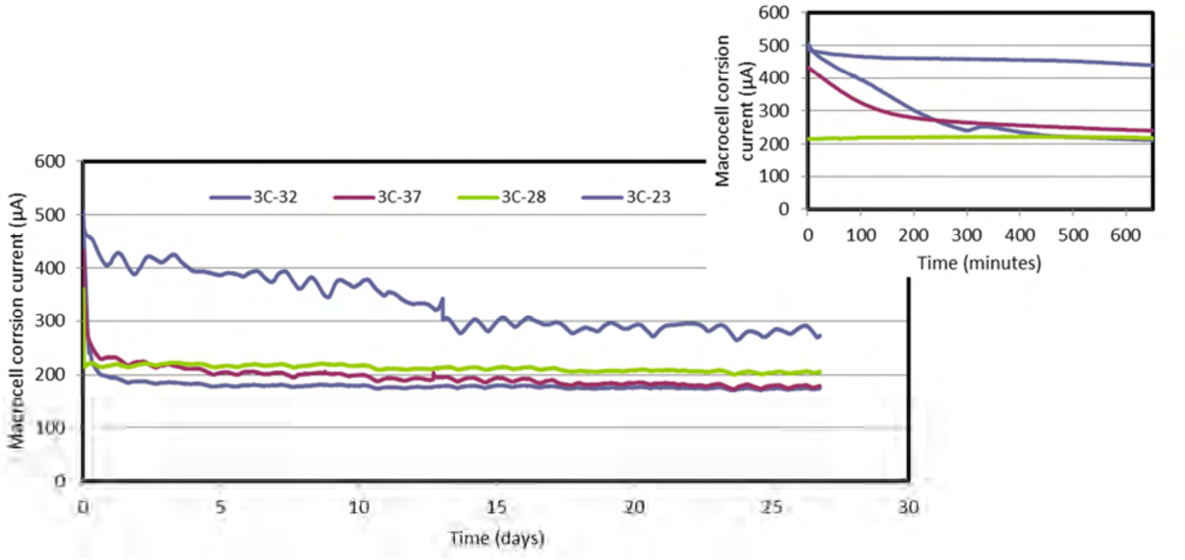

Figure 4-12 Macrocell current on samples with three passive bars connected to active one

The galvanic current produced for the samples in which 4 passive bars were connected was in a range between $175\ to\ 395\ \mu A$ respectively (Figure 4-13).

Figure 4-14 shows the evolution of macrocell corrosion current with the increase in number of passive steel bars. A clear tendency of producing higher macrocell corrosion current can be seen in samples with 4 passive bars connected to the active bar than to that samples with 1 passive bar is connected.

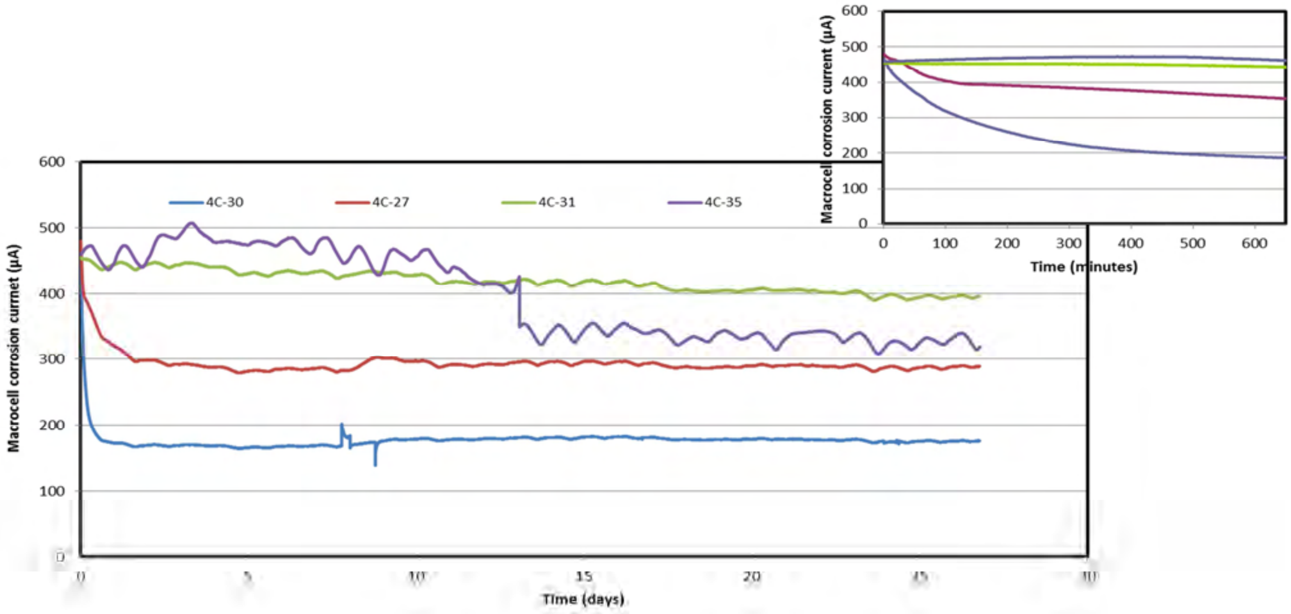

Figure 4-13 Macrocell current on samples with four passive bars connected to active one

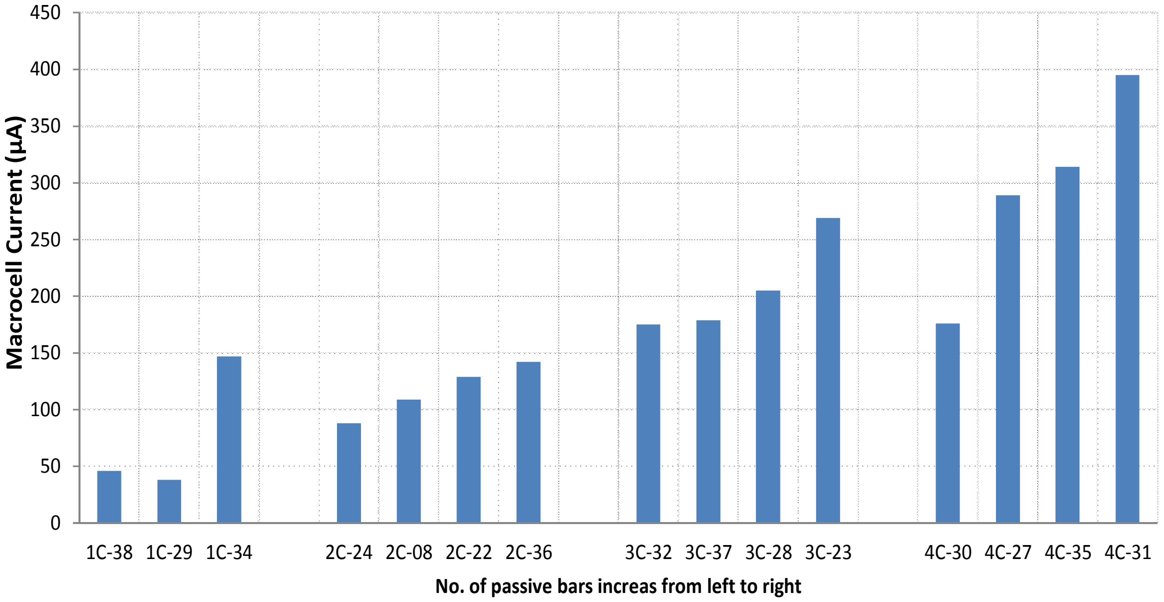

Figure 4-14 Effect of increase in No. of passive bars on macrocell current in configuration A.

With these experimental results the assumption that the increase in Cathode/Anode ratio can produce higher corrosion current during propagation phase is validated. And these results have also very close similitude to results found with numerical simulations.

In Figure 4-13 we observe that the macrocell corrosion current of 4C-31 is 393μA while the one of 4C-30 is only 175μA. Both samples had a connection of 4 passive steel bars with active steel bar. With the calculations of the electromotive force (cell potential) of both samples we find out that the 4C-30 has even slightly higher values (550 mV/SCE) than 4C-31 (-501.5 mV/SEC), but still macrocell current was lower in 4C-30. To understand why less macrocell current is produced in 4C-30 than in 4C-31, both samples were disconnected. Immediately after disconnecting, the potential of all the passive and active bars of both samples was measured. It was observed that the passive bars of 4C-30 were more polarized towards negative potential than the passive bars of 4C-31. The Tables 1 and 2 show the potential of passive steel bars before electrical connection and just after disconnection. After the equilibrium was established in both samples, the cell potential can be now calculated again. The 4C-30 had a cell potential -148mV while 4C-31 had -312mV.

This behavior can be explained by the shape of polarization curves shown in Figure 4-15. Two passive systems with same corrosion potential, corrosion density and anodicTafel slopes values are shown. But the passive system 1 has lower values of cathodic Tafel slope coefficients, while passive system 2 has higher of cathodic Tafel slope coefficients. The shape formed by passive system 2 (Figure 4-15) is such that, to achieve the equilibrium when connected to an active system, it has to be polarized more than passive system 1. Moreover, this behavior can be seen in the parametric study of cathodic Tafel slope coefficient of passive system β_{cp} in a macrocell galvanic system, where active and passive bars are involved. Figure 4-16 shows that as the value of β_{cp} increases the macrocell current decreases immensely. It can also be seen that with the increase in β_{cp} values the passive bar potential is polarized more towards the negative potential. This can explain the higher polarization of passive bar in case of 4C-30. It is also relevant to mention that if β_{cp} is higher the polarization of active steel towards positive potential is reduced. In case of 4C-30 a same behavior was found, i.e. active bar was only 14 mV polarized towards positive while it was polarized 18 mV towards positive potential in 4C-31.

So it can be concluded that the different values of macrocell current in the samples could be due to the different states of passivity of system in the concrete. The bars in different conditions of passivity could have altogether different corrosion parameters and polarization characteristics. The sensitivity analysis presented in section 3.5, allows analyzing how the change in different corrosion parameters influence the corrosion current density and polarization of active and passive system.

Table 4-2 Open circuit potential of passive and active steel bars in 4C-31 before connection and just after disconnecting.

Passive bars	**Corrosion Potential before connection (mV/SCE)**	**Corrosion Potential just after disconnecting (mV/SCE)**
95 4C-31	-100	-306
58 4C-31	-158	-242
75 4C-31	-105	-341
61 4C-31	-145	-301
Active bar 31	-628	-610

Table 4-3 Open circuit potential of passive and active steel bars in 4C-30 before connection and just after disconnecting.

Passive bars	**Corrosion Potential before connection (mV/SCE)**	**Corrosion Potential just after disconnecting (mV/SCE)**
54 4C-30	-97.7	-523
69 4C-30	-65	-504
55 4C-30	-95	-478
96 4C-30	-76	-386
Active bar 30	-635	-621

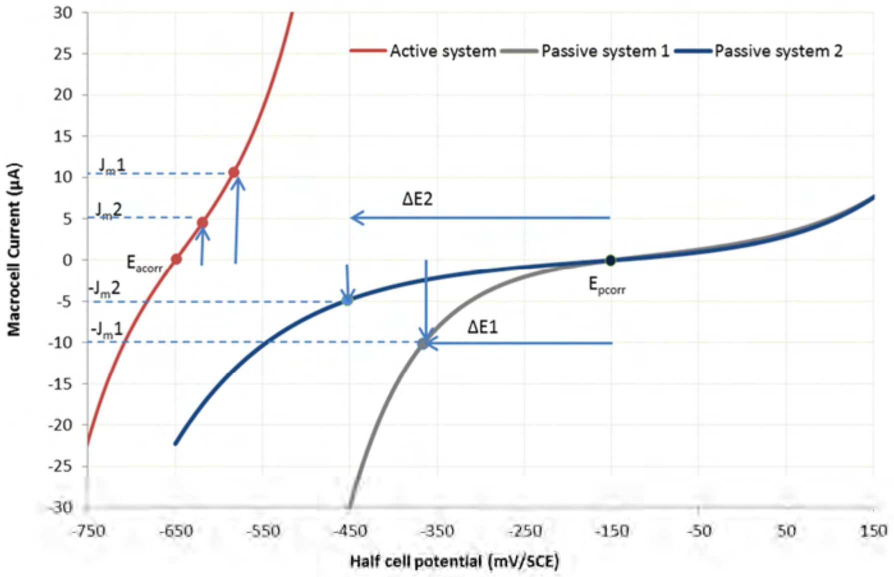

Figure 4-15 Quantitave illustration of two passive systems with different corrosion parameters

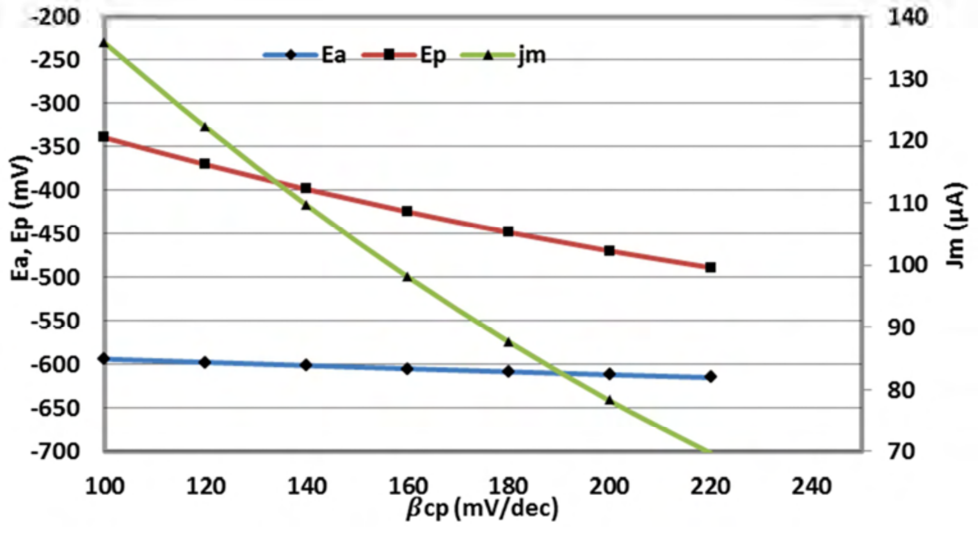

Figure 4-16 Influence of Cathodic Tafel slopes coefficient on macrocell corrosion system

Both samples were then broken to visually observe the corrosion state of active and passive steel bars, and also to observe if there were any differences at steel-concrete interface. The broken samples are shown in Figure 4-17 and Figure 4-18. In both samples the central active steel bar was depassivated and corrosion activities were underway. The rust products were clearly visible at steel surfaces. The passive bars were not corroded and had shining surface.

The pH values in sound concrete were above 12 as the phenolphthalein test gave a pink color. Only difference observed was that the corrosion products in 4C-31 travelled into the concrete volume at some distance from steel-concrete interface. These products were not observed in 4C-30. This proves that the macrocell current activities are not as prominent in sample 4C-30 as in 4C-31.

Figure 4-17 Sample 4C-31 after autopsy, on the active bar corrosion products are clearly visible travelled into concrete volume

Figure 4-18 Sample 4C-30 after autopsy, on the active bar corrosion products are only formed at steel concrete interface

4.3.3.2.2 Weight Loss measurements

To observe the weight loss of the samples, the active steel bars were taken out from concrete. Figure 4-19 shows the steel bars of both samples before cleaning process. The bars were then cleaned according to the ASTM G-I-90, (1999) standards using Clark’s solution. After passing through Clark’s solution the steel bars were cleaned in an ultrasonic bath to remove any corrosion products left on the steel surface. The cleaned bars are shown in Figure 4-20. The Figure 4-21 shows the weight loss in both samples, the samples were remained connected for this galvanic test during sixty days. At 4C-31 sample, the weight loss was $1643\ mg$ while for steel bar in 4C-30 it was $1315\ mg$. As expected the sample 4C-31 which produced the higher macrocell current had a higher weight loss. The difference of weight loss of both sample was not higher than the difference in their respective macrocell current, it is because of longer connection period for 4C30.

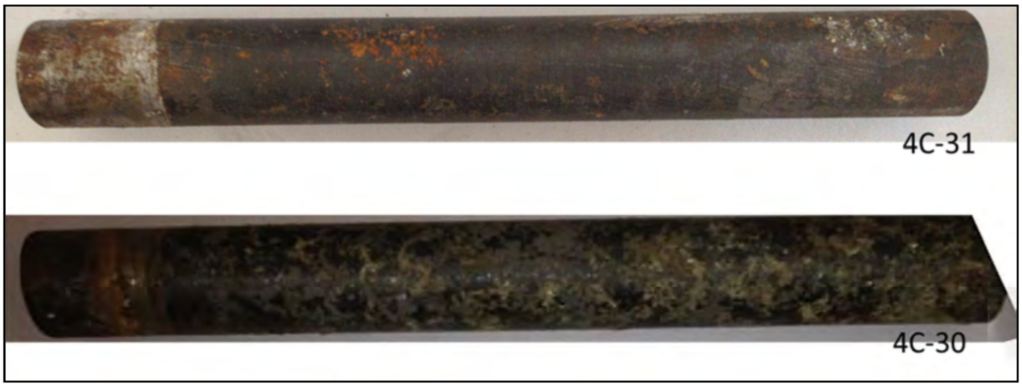

Figure 4-19 Active steel bars of sample 4C-31 and 4C-30, just after taken out from concrete

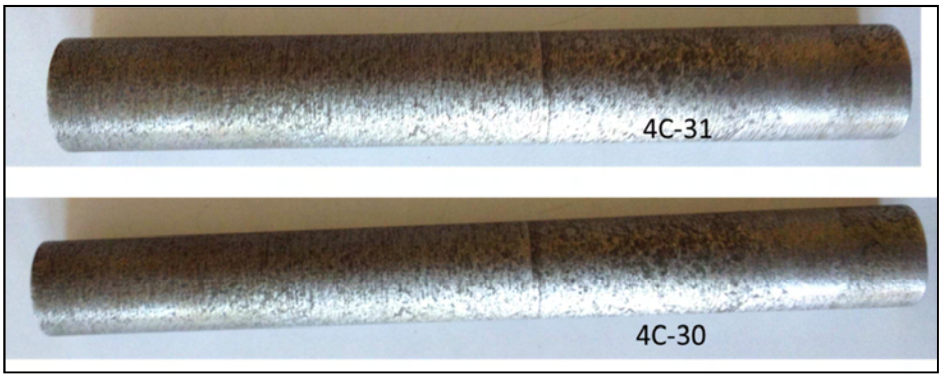

Figure 4-20 Steel bars after passing through Clark’s solution and Ultrasonic bath.

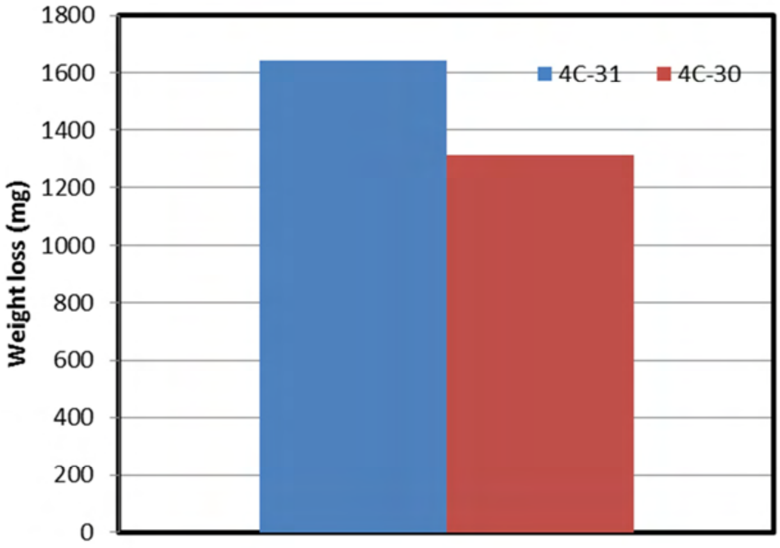

Figure 4-21 Weight loss in two samples with same number of passive bars but different current density

By using Faraday's law, the macrocell current of each steel bar was recalculated. Faraday's equation is given below, the current value was integrated over whole period of connection between active and passive bars.

$$m = \frac{M.Jcorr\ .t}{nF}$$

Where:

- *m* is mass loss of steel bar,
- *M* is molar mass of iron (55.8 g/mole),
- *Jcorr* is macrocell current, *n* are number electrons,
- *F* is faraday's constant (96500 C/mole),
- *t* is the time of electrical connection between active and passive bars.

The weight loss by Faraday's law was calculated by using macrocell corrosion current. The mass loss in case of sample 4C-31 was 1040 mg. While for sample 4C-30 it was 463 mg.

The macrocell/galvanic experiments were performed after 6 month of carbonation of the inner cylinders. Meanwhile the steel bars were in active state, and uniform/microcell corrosion process was undergoing. This could explain the less weight calculated by Faraday's law. The autopsy was performed after 4 months of disconnecting the samples from Yokogawa MW100 ®, during this period the microcell corrosion was ongoing at active steel bars. The weight loss by Faraday's law was calculated by two currents, the macrocell current (lasted for 2 months), and microcell current which lasted for 10 months (before + after the the macrocell connection). From Tafel experiments on carbonated samples, the corrosion current density was estimated around 1 µA/cm^2, the polarized surface area of steel was 75 cm^2. A global current was then calculated, and faraday's law was applied. The comparison between gravimetric weight losses and weight loss by two currents together is presented in Figure 4-22.

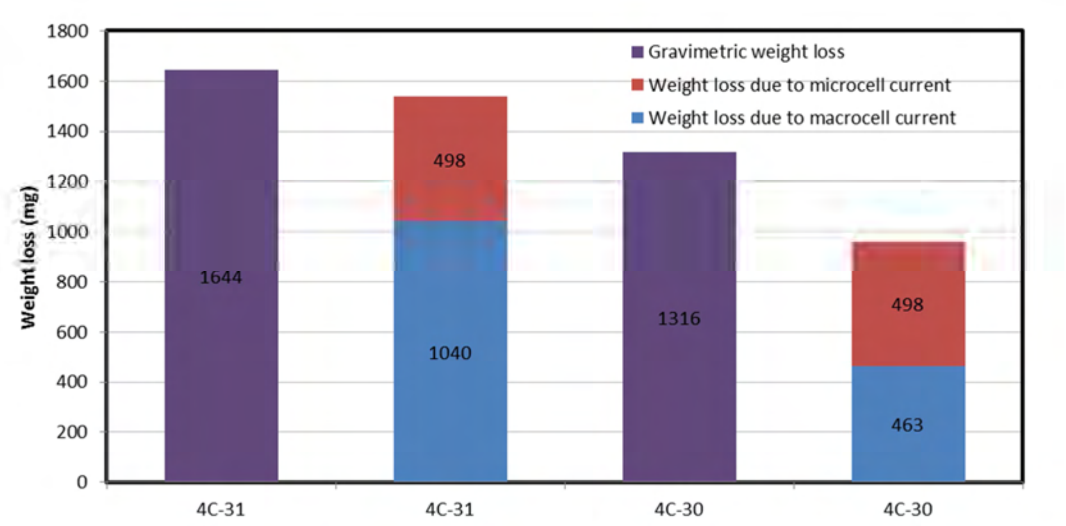

Figure 4-22 Comparison between weight loss measured gravimetrically and the weight loss calculated by Faraday's law.

The weight loss due to the galvanic connection which lasted only for two months has clearly lion shares in weight loss calculation by Faraday's law. The losses are in close range to each other.

Figure 4-23 shows a comparison between numerical values of macrocell current and the experimental values resulted from configuration A after stabilization of macrocell corrosion current. For this comparison, average values of all the configurations (A1, A2, A3 and A4) were taken. The error bars show the standard deviation for 3 samples in case of 1 passive bar connected, and for 4 samples for other configurations. If the exceptional value of macrocell current in sample 1C-34 is ignored, it can be seen that the deviation of extreme values in the first three cases is less than that of when all four passive bars are connected. This may be because when only one, two or three passive bars had to be connected, we could select the bars with a potential near to the most probable passive potential (i.e -135 mV/SCE), and to ignore those which had a potential far from these values. But in case of samples where all 4 passives bar had to be connected, it was not possible to make this selection. This could explain the higher difference in numerical and experimental values in case of 4 passive bars connected.

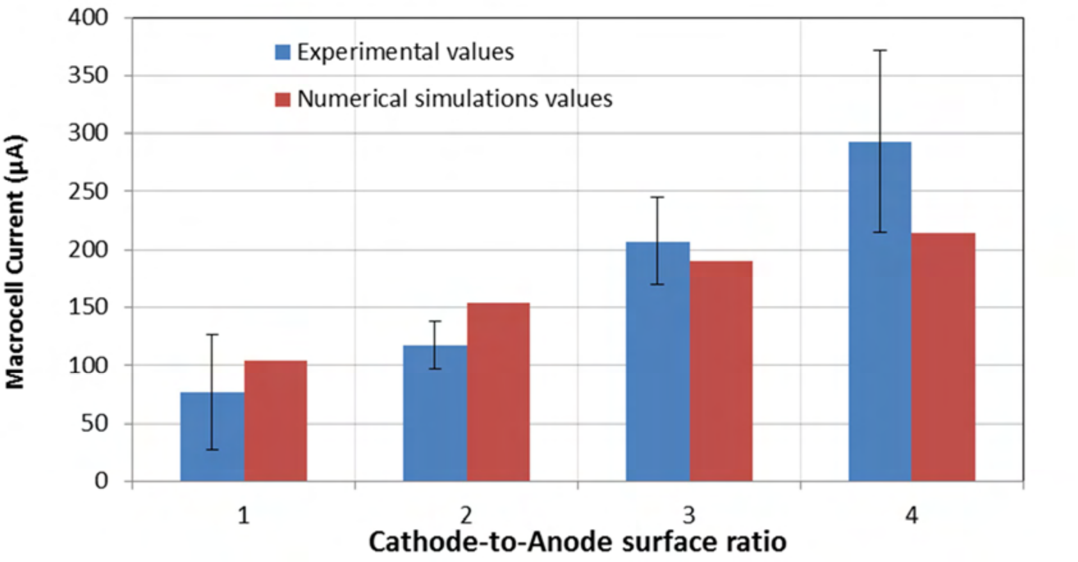

Figure 4-23 Comparison between experimental and numerical results of Cathode/Anode ratio effect, in case of configuration A.

In the Figure 4-23, it can be observed that the numerical results are in the same magnitude as the measured values. Qualitatively, both model and experimental samples exhibit same behavior, i.e with increase in Cathode/Anode ratio the macrocell current increases, and also rate of increase in macrocell current decreases with increase of Cathode/Anode ratio.

4.3.3.2.3 Results of configuration B

These tests were performed on the same samples as previously used. For each specimen, the number of connected passive bars was progressively increased from 1 to 4, and the galvanic current was noted after stabilization. The galvanic connection between active and passive bars was already lasted for six months with previous experiments for configuration A, so it was probable that the active and passive bars were polarized to new corrosion potential values. The Figure 4-25 shows the values of galvanic currents collected on experimental specimens thanks to Yokogawa MW100® device. Despite identical geometries and conditions, some differences are observed in experimental macrocell current levels between the specimens for each C/A ratio, as shown in Figure 4-25. For example 1C-29 produced 88 µA, while 4C-35 produced 267 µA macrocell current even if both samples had 4 passive bars connected to active one. Again these differences arise from the variability observed in free corrosion potential, and also from probable natural variability of the electrochemical parameters.

Nevertheless, for each specimen, the experimental relation between C/A ratio and macrocell current is well in accordance with the theoretical prediction achieved from numerical simulations presented in the Figure 4-8. Regarding the geometry of the specimens studied here, the macrocell current is increased by 2 to 8 times when changing the C/A ratio from 1 to 4. In Figure 4-25, the samples are organized according to the macrocell current values when all 4 passive bars were connected. The first sample 2C-08 gives minimum macrocell current when all four passive bars were connected, so it was presented at extreme left side, while sample 4C-35 gave a maximum value so it was at extreme right. All samples exhibit an increment in macrocell current when Cathode/Anode ratio is increased by adding passive bars.

The values of macrocell corrosion current obtained from configuration B are generally lower than those shown in case of configuration A. The values shown in configuration A are after 27 days, but the macrocell connection lasted for a period of six months, and over this period the macrocell current values were gradually reduced. The sample 4C-35 shows a current of 314 µA after 27 days. However, these values were decreased to 265 µA just before disconnection of configuration A and start of configuration B (Figure 4-24). Similarly sample 4C-27 in Figure 4-24 had a macrocell current value 289 µA after 27 days, and after 6 months the values were reduced to 235µA. The macrocell current values found in sample 4C-27 when 4 passive bars were connected during configuration B were 199 µA. So the lower values in case of configuration B could be explained by the time elapse between two experiments, during which the concrete-steel surface interface condition were significantly changed by the corrosion products.

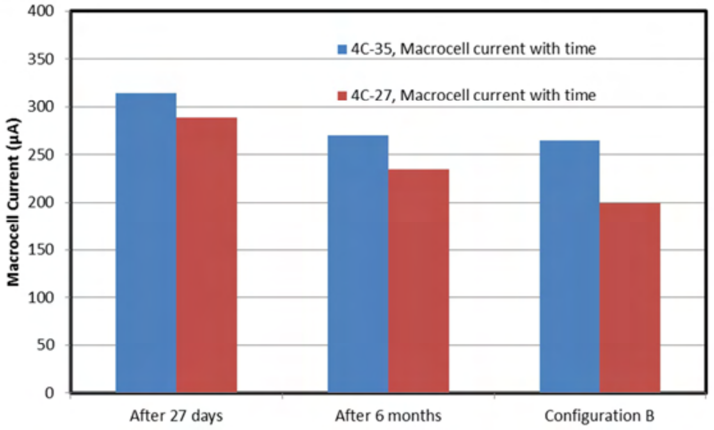

Figure 4-24 Macrocell current reduced gradually with the increase in the time of electrical connection

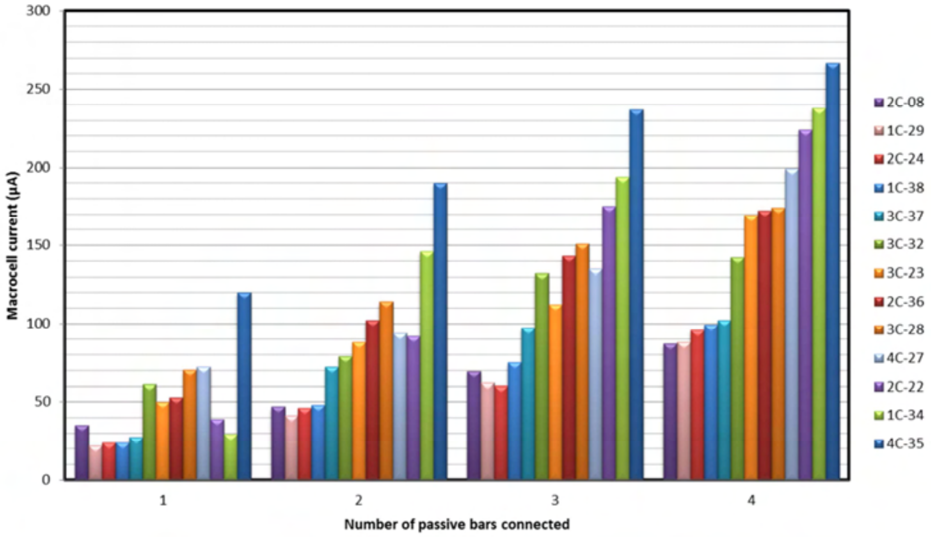

Figure 4-25 Macrocell current on different samples when passive bars were progressively increased from 1 to 4

In the Figure 4-26, the averaged values of galvanic currents of the 15 specimens are plotted versus the cathode-to-anode ratio. Error bars in the bar plot highlight the standard deviation relative to these 15 specimens. The values of galvanic current versus cathode-to-anode surface ratio achieved by numerical simulation are also plotted in the Figure 4-26. Despite, rather high differences in macrocell corrosion current, the rate of current increase with C/A is similar. The difference in macrocell corrosion current could again be explained by a probable coarse approximation of simulation parameters, the plot highlights the coherence between the modeling/simulation approach and the experimental results.

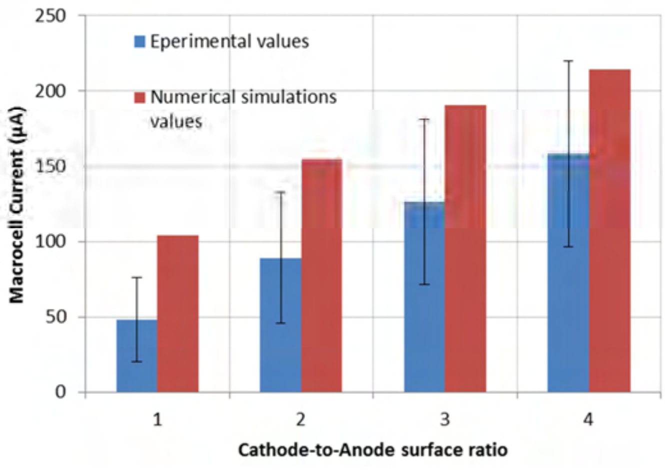

Figure 4-26 Experimental average values of macrocell current in case of configuration B vs cathode-to-anode surface ratio – Comparison with numerical simulations

4.4 Conclusion

The work presented in this chapter was carried out on the assumption that the corrosion can also be accelerated in the propagation phase. This assumption was based on the Cathode/Anode ratio, which was changed by change in passive bars embedded in the cylindrical concrete samples. The results show that with the increase in Cathode/Anode ratio, the macrocell corrosion current can be increased. A 8 times higher macrocell current was obtained from the samples with Cathode/Anode ratio equal to 4, than to those with Cathode/Anode ratio equal to 1. This means that corrosion process can be accelerated not only in initiation phase but also in the propagation phase. These results help to achieve a naturally occurring corrosion in laboratory environment, and in consequence can help to understand better the corrosion phenomena in real structures.

The numerical model based on Butler-Volmer kinetics was also presented in this chapter, the results show that the model has same behaviour as found in laboratory experiments, i.e. with increase in C/A the macrocell current also increases. The polarization behavior in both cases was also found similar. But quantitatively the values were little different, these differences are clearly arisen from the selection of corrosion parameters. If these parameters are recognized accurately for given concrete conditions, the corrosion phenomena can be modeled numerically with more precision.

5 Conclusions and prospects

An accelerated corrosion test could be helpful to better understand the corrosion behavior of steel in RC structures. In the accelerated corrosion test proposed in this work, the galvanic/macrocell corrosion current was induced without any external power supply device in propagation phase. So the corrosion observed was a replica of naturally occurring corrosion in real reinforced concrete structures, with partially carbonated concrete. Once the steel bar is depassivated after initiation phase, the required level of corrosion in RC can be achieved by controlling the cathode surface area.

Two different configurations, depending upon how passive bars are connected to central active bar, were tested. The configuration A consists of connecting a fixed numbers of passive bars, i.e. 1, 2, 3 or 4 passive bars were connected on a given sample. The number of passive bars is not changed during the test. While in Configuration B the passive bars are progressively increased from 1 to 4 during the test. With both configurations A and B, the value of macrocell corrosion current is considerably increased with increase in Cathode/Anode (C/A) ratio. Although the rate at which corrosion current increases is not proportional to C/A ratio, instead it decreases with increase in ratio. Same tendency is found in numerical results. The number of passive bars is increased from 1 to 8 progressively, and with increase in C/A ratio, the macrocell current increases. Qualitatively, both experimental tests and numerical simulations behave in same manner; quantitatively differences could be due to the rough estimation of corrosion parameters used in simulations.

The circumferential potential mapping was performed on experimental samples parallel to steel bars. When only one passive bar is connected, it was found a more electronegative potential than in the case of four passive bars connected. Same behavior is also found with numerical simulations. This shows that when the corrosion is occurring under the effect of galvanic/macrocell system, half-cell potential measurements could lead to erroneous conclusions. A system with small cathode surface will give more electronegative potential values, but the corrosion current will be lesser than in the case of a system where the cathode surface is larger. On the other hand, a galvanic corrosion system connected to larger cathode surface area can give less electronegative values of half-cell potential while the rate of corrosion can be very high.

To simulate corrosion phenomenon numerically, it is essential to estimate the corrosion parameters (corrosion potential, corrosion current density and anodic and cathodic Tafel slope) accurately according to the conditions of concrete and steel in it. A comprehensive experimental study is presented on corrosion parameters in carbonated concrete as well as in non-carbonated concrete. The average value of corrosion potential of active bars in carbonated concrete was found to -645 mV/SCE, and deviation from average values was small. While in case of steel in non-carbonated concrete the range of corrosion potential value was quite large, from -15mV/SCE to -214mV/SEC. This range could be explained by large range of passive zone (potential values) of a steel bar which is under the oxide layer (passive layer). The equilibrium could be formed at different values of potential, depending upon the steel passivity and also to the degree of saturation of concrete. So it is very important to consider the state of concrete to access the corrosion parameters for modeling.

The average corrosion current density of active steel bar was 0.86μA/cm^2. The average of corrosion current density for passive steel bars was 0.05μA/cm^2, these values are well in accordance with the values found in literature. The values of anodic and cathodic Tafel slope for active steel bars were 244mV/dec and 260mv/dec respectively. These values are considerably higher than those used by other researchers who simulated the corrosion in reinforced concrete. The scan rates from 0.1, 0.5 and 0.8 mV/s were used to perform Tafel experiments, the polarization curves obtained under different scan rates had same shape, and hence, the parameters found under different scan rates were in same range. Since there is not a lot of work performed on corrosion parameters in carbonated concrete, these results could provide an initial step towards defining the corrosion parameters values in carbonated concrete.

As the corrosion parameters found in literature and also in this work are somewhat scattered, a sensitivity analysis was carried out to observe the effects on macrocell corrosion system with the change in these corrosion parameters. Some parameters e.g. equilibrium corrosion potential (E_{acorr}, E_{pcorr}) are found to be highly influential on macrocell corrosion. Corrosion parameters of passive system are more influential on macrocell current than the parameters of active system. As illustrated by polarization curves of a macrocell corrosion system, the anodic Tafel slope coefficient of active system and cathodic Tafel slope of passive system were more influential on macrocell corrosion system. Moreover, change in cathodic Tafel slope of passive system had more effect on macrocell system than to anodic slope coefficient of active system.

With numerical simulations, the face to face polarization phenomenon was observed. The face of active steel which faces the passive steel bar was more polarized than to its opposite side. Similarly, the side of passive bar which was facing the active bar was more polarized than the opposite side. Concrete resistivity has a huge role in development of a macrocell/galvanic corrosion system in concrete structures. With higher values of resistivity, ohmic drop is quite significant and macrocell corrosion current is very small and vice-versa.

Main perspectives:

The results have shown the reliability of this accelerated corrosion test clearly. This test could be used to observe the corrosion sensitivity of various systems involving different types of reinforcing steels or concretes at different environmental conditions. For example, different types of cements can be used to cast the concrete, and their effects on corrosion could be studied. The corrosion behavior can be studied when different additions like, fly ash, metakaolin and silica fume are used in concrete. Their effects on polarization curves could be observed. Moreover, the efficiency of corrosion inhibitors could be checked on the development of macrocell corrosion. The test could also be easily performed in different environmental conditions by varying temperature and/or hygrometry.

The numerical model could also be improved. In particular, the numerical simulations were performed on the assumption that the polarization is only due to the activation; charge is transferred only by electron flow. The Butler-Volmer equations can be modified to simulate the effect of oxygen diffusion and limiting current density parameter can also be taken into account. Further research should also be carried out to build a dynamic model in transitory state of corrosion, by taking account of capacitance of concrete-steel interface. In order to achieve a better quantitative correlation between numerical and experimental results, inverse modeling could be carried out to optimize electrochemical parameters involved in the simulations.

The test could also be used for a better quantification of the effects of galvanic corrosion in carbonated concrete. Indeed, usually, concrete carbonation is assumed to induce uniform corrosion of reinforcing steel by uniform depassivation. In electrochemistry, the assumption of uniform corrosion means that anodic and cathodic reactions occur quite at the same locations on the steel-concrete interface. Since most of the time concrete is only partially carbonated, so already active reinforcement bars are connected to the till passive bars in sound concrete through stirrups or by longitudinal bars. That is why, in most of the cases in reinforced concrete, the corrosion phenomena are macrocell rather than microcell. Or at least the macrocell current is much more significant than the microcell current. But in contrast, most of the corrosion measuring instruments are based on the theory of microcell/uniform corrosion. That is why further research must be carried out to develop the corrosion measurement methods in concrete structures where macrocell/galvanic corrosion is underway.

6 References

Ahmad, S., 2009. Techniques for inducing accelerated corrosion of steel in concrete. The Arabian Journal for Science and Engineering 95–104.

Ahn, W., 2001. Galvanostatic testing for the durability of marine concrete under fatigue loading. Cement and Concrete Research 31, 343–349.

Almusallam, A.A., Al-Gahtani, A.S., Aziz, A.R., Rasheeduzzafar, 1996. Effect of reinforcement corrosion on bond strength. Construction and Building Materials 10, 123–129.

Alonso, C., Castellote, M., Andrade, C., 2002. Chloride threshold dependence of pitting potential of reinforcements. Electrochimica Acta 47, 3469–3481.

Andrade, C., Alonso, C., 1996. Corrosion rate monitoring in the laboratory and on-site. Construction and Building Materials 10, 315–328.

Andrade, C., Alonso, C., 2004. Test methods for on-site corrosion rate measurement of steel reinforcement in concrete by means of the polarization resistance method. Mat. Struct. 37, 623–643.

Arya, C., Vassie, P.R.., 1995. Influence of cathode-to-anode area ratio and separation distance on galvanic corrosion currents of steel in concrete containing chlorides. Cement and Concrete Research 25, 989–998.

ASTM C876-09, 2009. Test Method for Corrosion Potentials of Uncoated Reinforcing Steel in Concrete. G01 Committee, ASTM International.

ASTM G-I-90, 1999. Practice for Preparing, Cleaning, and Evaluating Corrosion Test Specimens. G01 Committee ASTM International.

Balayssac, J.P., Détriché, C.H., Grandet, J., 1995. Effects of curing upon carbonation of concrete. Construction and Building Materials 9, 91–95.

Bertolini, L., Elsener, B., Pedeferri, P., Polder, R.B., 2004. Corrosion of Steel in Concrete. John Wiley & Sons.

Brem, 2004. Numerische Modellierung der Korrosion in Stahlbetonbauten. Dissertation. Edgennoissche Technische Hochschule Zurich.

Broomfield, J.P., 2007. Corrosion of Steel in Concrete: Understanding, Investigation and Repair. Taylor & Francis.

Cefracor, n.d. Notions fondamentales, Aspects électrochimiques de la corrosion.

Chang, Z.-T., Cherry, B., Marosszeky, M., 2008. Polarisation behaviour of steel bar samples in concrete in seawater. Part 1: Experimental measurement of polarisation curves of steel in concrete. Corrosion Science 50, 357–364.

Clément, A., Laurens, S., Arliguie, G., Deby, F., 2012. Numerical study of the linear polarisation resistance technique applied to reinforced concrete for corrosion assessment. European Journal of Environmental and Civil Engineering 16, 491–504.

El Maaddawy, T.A., Soudki, K.A., 2003. Effectiveness of Impressed Current Technique to Simulate Corrosion of Steel Reinforcement in Concrete. Journal of Materials in Civil Engineering 15, 41–47.

Elsener, B., 2005. Corrosion rate of steel in concrete—Measurements beyond the Tafel law. Corrosion Science 47, 3019–3033.

Elsener, B., Andrade, C., Gulikers, J., Polder, R., Raupach, M., 2003. Hall-cell potential measurements—Potential mapping on reinforced concrete structures. Mat. Struct. 36, 461–471.

Feliú, S., González, J., Andrade, C., 1996. Electrochemical Methods for On-Site Determinations of Corrosion Rates of Rebars, in: Berke, N., Escalante, E., Nmai, C., Whiting, D. (Eds.), Techniques to Assess the Corrosion Activity of Steel Reinforced Concrete Structures. ASTM International, 100 Barr Harbor Drive, PO Box C700, West Conshohocken, PA 19428-2959, pp. 107–107–12.

Feliu, V., González, J.A., Adrade, C., Feliú, S., 1998. Equivalent circuit for modelling the steel-concrete interface. II. Complications in applying the stern-geary equation to corrosion rate determinations. Corrosion Science 40, 995–1006.

Fortuné, I.V., 2009. Sensibilité de la technique d'émission acoustique à la corrosion des armatures dans le béton [WWW Document]. URL http://thesesups.ups-tlse.fr/666/ (accessed 2.20.13).

Garcés, P., Andrade, M.C., Saez, A., Alonso, M.C., 2005. Corrosion of reinforcing steel in neutral and acid solutions simulating the electrolytic environments in the micropores of concrete in the propagation period. Corrosion Science 47, 289–306.

Ge, J., Isgor, O. b., 2007. Effects of Tafel slope, exchange current density and electrode potential on the corrosion of steel in concrete. Materials and Corrosion 58, 573–582.

Gjorv, O., Vennesland, Ø., El-Busaidy, A., 1977. Electrical Resistivity Of Concrete In The Oceans. The Offshore Technology Conference.

Gu P., 1998. Obtaining Effective Half-Cell Potential Measurements in Reinforced Concrete Structures. National Research Council of Canada.

Gulikers, J., Raupach, M., 2006. Modelling of reinforcement corrosion in concrete. Materials and Corrosion 57, 603–604.

Hansson, Jaffer, S. J.,, Poursea, A, 2007. Corrosion of Reinforcing Bars in Concrete. Portland Cement Association, Skokie, Illinois, USA:

Haselbach, L., 2009. Potential for Carbon Dioxide Absorption in Concrete. Journal of Environmental Engineering 135, 465–472.

Ha-Won Song, 2007. Corrosion Monitoring of Reinforced Concrete Structures – A Review. International Journal of Electrochem Science 2, 1– 28.

Isgor, O.B., Razaqpur, A.G., 2006. Modelling steel corrosion in concrete structures. Mater Struct 39, 291–302.

Ismail, M., Ohtsu, M., 2006. Corrosion rate of ordinary and high-performance concrete subjected to chloride attack by AC impedance spectroscopy. Construction and Building Materials 20, 458–469.

Kear, G., Walsh, F.C., 2005. The characteristics of a true Tafel slope [WWW Document]. Corrosion and Materials. URL http://eprints.soton.ac.uk/49025/ (accessed 2.20.13).

Kim, C.-Y., Kim, J.-K., 2008. Numerical analysis of localized steel corrosion in concrete. Construction and Building Materials 22, 1129–1136.

Lee, C., Bonacci, J.F., Thomas, M.D., Maalej, M., Khajehpour, S., Hearn, N., Pantazopoulou, S., Sheikh, S., 2000. Accelerated corrosion and repair of reinforced concrete columns using carbon fibre reinforced polymer sheets. Canadian Journal of Civil Engineering 27, 941–948.

Marques, P.F., Costa, A., 2010. Service life of RC structures: Carbonation induced corrosion. Prescriptive vs. performance-based methodologies. Construction and Building Materials 24, 258–265.

McCafferty, E., 2005. Validation of corrosion rates measured by the Tafel extrapolation method. Corrosion Science 47, 3202–3215.

Miyazato, S., 2010. Steel Corrosion Induced by Chloride or Carbonation in Mortar with Bending Cracks or Joints. Journal of Advanced Concrete Technology 8, 135–144.

Nasser, A., 2010. La corrosion des aciers dans le béton à l'état passif et par carbonatation : prise en compte des courants galvaniques et des défauts d'interface acier-béton [WWW Document]. URL http://thesesups.ups-tlse.fr/1091/ (accessed 2.20.13).

Nasser, A., Clément, A., Laurens, S., Castel, A., 2010. Influence of steel–concrete interface condition on galvanic corrosion currents in carbonated concrete. Corrosion Science 52, 2878–2890.

Nygaard, P.V., 2009. Non-destructive electrochemical monitoring of reinforcement corrosion. DTU Civil Engineering-Report R-202 (UK).

Perez, N., 2004. Electrochemistry and Corrosion Science.

Polder, R., Andrade, C., Elsener, B., Vennesland, Ø., Gulikers, J., Weidert, R., Raupach, M., 2000. Test methods for on site measurement of resistivity of concrete. Mat. Struct. 33, 603–611.

Poupard, O., Aït-Mokhtar, A., Dumargue, P., 2004. Corrosion by chlorides in reinforced concrete: Determination of chloride concentration threshold by impedance spectroscopy. Cement and Concrete Research 34, 991–1000.

Pourbaix, M., 1974. Applications of electrochemistry in corrosion science and in practice. Corrosion Science 14, 25–82.

Poursaee, A.E., 2007. An Analysis of the Factors Influencing Electrochemical Measurements of the Condition of Reinforcing Steel in Concrete Structures. University of Waterloo, Waterloo Ontario, Canada.

Ramachandran, S. Campbell,, M. W Ward, 2001. The Interactions and Properties of Corrosion Inhibitors with Byproduct Layers. CORROSION 57.

Raupach, M., 2006. Models for the propagation phase of reinforcement corrosion – an overview. Materials and Corrosion 57, 605–613.

Redaelli, E., Bertolini, L., Peelen, W., Polder, R., 2006. FEM-models for the propagation period of chloride induced reinforcement corrosion. Materials and Corrosion 57, 628–635.

Revie, R.W., Uhlig, H.H., 2008. Corrosion and Corrosion Control: An Introduction to Corrosion Science and Engineering, Fourth Edition.

Roberge, P.R., 2000. Handbook of Corrosion Engineering. MCGraw Hill., New York.

Smith, R., 2007. The effects of corrosion on the performance of reinforced concrete beams. Theses and dissertations.

Soleymani, H.R., Ismail, M.E., 2004. Comparing corrosion measurement methods to assess the corrosion activity of laboratory OPC and HPC concrete specimens. Cement and Concrete Research 34, 2037–2044.

Song, G., 2000a. Equivalent circuit model for AC electrochemical impedance spectroscopy of concrete. Cement and Concrete Research 30, 1723–1730.

Song, G., 2000b. Theoretical analysis of the measurement of polarisation resistance in reinforced concrete. Cement and Concrete Composites 22, 407–415.

Stern, M., Geary, A.L., 1957. Electrochemical Polarization I . A Theoretical Analysis of the Shape of Polarization Curves. J. Electrochem. Soc. 104, 56–63.

Stratfull, R. F, 1957. The corrosion of steel in a reinforced concrete bridge. Corrosion 13, 173–178.

Tanner's Chemistry, n.d. Tanner's General Chemistry - Molar Conductivity [WWW Document]. URL http://www.tannerm.com/molar_cond.htm (accessed 2.20.13).

Tuutti, K, 1982. Corrosion of steel in concrete (Research Report FO 4). Swedish Cement and Concrete Research Institute,, Stockholm.

Verbeck, G.J., 1958. Carbonation of hydrated Portland cement. Portland Cement Association, Chicago.

Warkus, J., Brem, M., Raupach, M., 2006. BEM-models for the propagation period of chloride induced reinforcement corrosion. Materials and Corrosion 57, 636–641.

Warkus, J., Raupach, M., 2006. Modelling of reinforcement corrosion – Corrosion with extensive cathodes. Materials and Corrosion 57, 920–925.

Warkus, J., Raupach, M., 2008. Numerical modelling of macrocells occurring during corrosion of steel in concrete. Materials and Corrosion 59, 122–130.

Yingshu, Y., Yongsheng Ji, Surendra P. Shah, 2007. Comparison of Two Accelerated Corrosion Techniques for Concrete Structures. ACI Structural Journal 104, 344–347.